

Copyright  
by  
Tianyi Wang  
2012

The Dissertation Committee for Tianyi Wang certifies that this is the approved version of the following dissertation:

**DEVELOPMENT AND APPLICATION OF OPTICAL IMAGING  
TECHNIQUES IN DIAGNOSING CARDIOVASCULAR DISEASE**

**Committee:**

---

Thomas E. Milner, Supervisor

---

Marc D. Feldman

---

Keith P. Johnston

---

Andrew K. Dunn

---

James W. Tunnell

**DEVELOPMENT AND APPLICATION OF OPTICAL IMAGING  
TECHNIQUES IN DIAGNOSING CARDIOVASCULAR DISEASE**

by

**TIANYI WANG, B.E., M.E.**

**Dissertation**

Presented to the Faculty of the Graduate School of

The University of Texas at Austin

in Partial Fulfillment

of the Requirements

for the Degree of

**DOCTOR OF PHILOSOPHY**

**The University of Texas at Austin**

**May 2012**

## Dedication

To my dear parents Mr. Jiaochun Wang and Mrs. Cuiqiong Xu,  
and my wonderful wife Jingjing Sun.

## Acknowledgements

I am most heartily thankful to my supervisor, Professor Thomas E. Milner, for his continuous support and encouragement throughout my whole PhD study. It is him who brought me into this research area, offered me the freedom to express my ideas and explore my interest without a restricted path, and provided me with insightful advices and suggestions that guide me to my goals. Professor Milner is a very kind and patient person, with whom I feel very lucky to be working. Undoubtedly, his intuition, critical suggestions and precise logic inspired me in every step of my research. I will never forget his words "Let's walk through this problem", which always makes me feel warm and confident because I am not facing the difficulties on my own. Professor Milner is not only a scientist, an engineer, but also a manager. His view of a project is way beyond the laboratory scope and is always connected with potential clinical applications.

However, this dissertation would not have been accomplished without support and advice from numerous other people. Professor Marc D. Feldman is one such person to whom I owe my heartfelt gratitude. Professor Feldman is a respected cardiologist who introduced me into the field of cardiovascular imaging and provides a tight link between my research and clinical importance. He has given me invaluable advice and suggestions that keep me from detours and is also appreciated for reviewing many of my manuscripts for publication and providing very detailed and thoughtful comments.

My gratitude goes to Professor Keith P. Johnston for his valuable advice and collaboration on manufacturing and supplying imaging contrast agents for my research. His novel nanoparticles provide me such a powerful tool to detect macrophages and make my research much easier, faster and more efficient.

I also would like to thank Professors James W. Tunnell and Andrew K. Dunn for serving on my dissertation committee, allowing me to use equipment and imaging setups in their labs for my experiments and their support in my research especially with regard to questions related to optical properties measurements. My appreciation also goes to Dr. Greg Allen for taking care of my health and encouraging me when under pressure.

Additionally, I would like to extend my appreciations to my labmates and fellow researchers. Especially, Dr. Jinze Qiu, Dr. Amit Paranjape, Dr. Jordan Dwelle, Austin McElroy, Biwei Yin, Sahar Elahi (from Milner's lab at UT Austin), S. M. Shams Kazmi, Dr. Arnold Estrada (from Dunn's lab at UT Austin), Varun Pattani (from Tunnell's lab at UT Austin), Dr. Li Ma, Brian Willsey, Ameya Borwankar (from Johnston's lab at UT Austin), Dr. Jake Mancuso, Dr. Veronika Sapozhnikova, J. Travis Jenkins and David Halaney (from Feldman's lab at UTHSCSA). The days and nights I spent with them in the past four and one-half years have been a joyful and wonderful memory for me.

I would like to express my deepest love and appreciation to my dear parents for their years of sacrifice and unconditional love. To my wonderful and lovely wife, Jingjing Sun, I thank you very much for loving, caring, supporting and encouraging me in every aspect throughout the years. I can barely achieve anything without your support and company.

Last but not least, with all my heart, I appreciate Mr. and Mrs. Boudreaux and all the "Life Group" members. They are my family in the U.S. and introduced me to God, to Whom I will always open my heart, pray and listen.

# DEVELOPMENT AND APPLICATION OF OPTICAL IMAGING TECHNIQUES IN DIAGNOSING CARDIOVASCULAR DISEASE

Tianyi Wang, Ph.D.

The University of Texas at Austin, 2012

Supervisor: Thomas E. Milner

Atherosclerosis and specifically rupture of vulnerable plaques account for 23% of all deaths worldwide, far surpassing both infectious diseases and cancer. Plaque-based macrophages, often associated with lipid deposits, contribute to atherogenesis from initiation through progression, plaque rupture and ultimately, thrombosis. Therefore, the macrophage is an important early cellular marker related to vulnerability of atherosclerotic plaques. The objective of my research is to assess the ability of multiple optical imaging modalities to detect, and further characterize the distribution of macrophages (having taken up plasmonic gold nanoparticles as a contrast agent) and lipid deposits in atherosclerotic plaques.

Tissue phantoms and macrophage cell cultures were used to investigate the capability of nanorose as an imaging contrast agent to target macrophages. *Ex vivo* aorta segments from a rabbit model of atherosclerosis after intravenous nanorose injection were imaged by optical coherence tomography (OCT), photothermal imaging (PTW) and two-photon luminescence microscopy (TPLM), respectively. OCT images depicted

detailed surface structure of atherosclerotic plaques. PTW images identified nanorose-loaded macrophages (confirmed by co-registration of a TPLM image and corresponding RAM-11 stain on a histological section) associated with lipid deposits at multiple depths. TPLM images showed three-dimensional distribution of nanorose-loaded macrophages with a high spatial resolution. Imaging results suggest that superficial nanorose-loaded macrophages are distributed at shoulders on the upstream side of atherosclerotic plaques at the edges of lipid deposits. Combination of OCT with PTW or TPLM can simultaneously reveal plaque structure and composition, permitting assessment of plaque vulnerability during cardiovascular interventions.



## Table of Contents

List of Tables .....	xiv
List of Figures .....	xv
Chapter 1 Introduction .....	1
1.1 Motivation.....	1
1.2 Research Objectives.....	3
1.3 Dissertation Overview .....	4
1.4 References.....	7
Chapter 2 Background .....	11
2.1 Cardiovascular Disease.....	11
2.1.1 Current Status of Cardiovascular Disease.....	11
2.1.2 Pathophysiology of Atherosclerosis .....	13
2.2 Diagnosis and Treatment of Atherosclerosis .....	15
2.2.1 Current Imaging Modalities for Atherosclerosis Detection.....	15
2.2.2 Medical Treatment of Atherosclerosis.....	19
2.3 Imaging Contrast Agents for Atherosclerosis Targeting .....	20
2.3.1 A Review of Currently Used Contrast Agents.....	20
2.3.2 A Novel Contrast Agent: Nanorose .....	22
2.4 References.....	22
Chapter 3 Optical Properties of Nanorose .....	39
3.1 Abstract .....	39
3.2 Introduction.....	39
3.3 Materials and Methods.....	40
3.3.1 Direct Measurement.....	40
3.3.2 Discrete Dipole Approximation.....	41
3.4 Results and Discussion .....	42
3.5 Conclusion .....	42
3.6 References.....	43

Chapter 4 Photothermal Wave (PTW) Imaging of Nanorose and Lipid .....	44
4.1 Fixed-frequency PTW Imaging of Macrophages and Lipid Deposits in Ex Vivo Tissues .....	44
4.1.1 Abstract .....	44
4.1.2 Introduction .....	45
4.1.3 Materials and Methods .....	46
4.1.3.1 Preparation of Tissues .....	46
4.1.3.2 PTW Theory and System .....	47
4.1.4 Results .....	49
4.1.5 Discussion .....	51
4.1.6 Conclusion .....	52
4.1.7 Acknowledgements .....	53
4.1.8 References .....	53
4.2 Multi-frequency PTW Imaging of Lipid Deposits in Ex Vivo Tissues .....	55
4.2.1 Summary .....	55
4.2.2 Description of Design Objective .....	55
4.2.3 Analysis and Performance Evaluation .....	56
4.2.4 Discussion .....	58
4.2.5 Conclusion .....	59
4.2.6 References .....	59
4.3 Swept-frequency PTW Imaging of Nanorose in Tissue Phantoms .....	60
4.3.1 Abstract .....	60
4.3.2 Introduction .....	60
4.3.3 Materials and Methods .....	61
4.3.4 Results .....	62
4.3.5 Discussion .....	65
4.3.6 Conclusion .....	66
4.3.7 References .....	66

Chapter 5 Fluorescence Imaging of Macrophages in Atherosclerotic Plaques Using Gold Nanoparticles.....	67
5.1 Abstract.....	67
5.2 Introduction.....	67
5.3 Materials and Methods.....	70
5.3.1 Preparation of Macrophage Cell Culture and Ex Vivo Arterial Tissues.....	70
5.3.2 Imaging Systems.....	70
5.4 Results.....	72
5.4.1 Fluorescence of NRs in Macrophage Cell Culture.....	72
5.4.2 Fluorescence of NRs in Arterial Tissues.....	73
5.5 Discussion and Conclusion.....	76
5.6 Acknowledgements.....	77
5.7 References.....	77
Chapter 6 PTW Imaging Combined with OCT for Macrophage and Lipid Detection in Atherosclerotic Plaques Using Gold Nanoparticles.....	80
6.1 Abstract.....	80
6.2 Introduction.....	81
6.3 Materials and Methods.....	84
6.3.1 Macrophage Cell Culture.....	84
6.3.2 Preparation of Rabbit Arterial Tissues.....	84
6.3.3 Imaging Systems.....	85
6.3.3.1 PTW Imaging.....	85
6.3.3.2 OCT.....	86
6.3.3.3 TPL Microscopy.....	86
6.3.4 Histology Analysis.....	87
6.3.5 Statistical Analysis.....	88
6.3.6 Analysis of Area Percentage of Nanorose in Plaques.....	88
6.4 Results.....	88
6.4.1 Nanorose Uptake by Macrophages.....	88
6.4.2 Nanorose Identification by TPL Microscopy in Histological	

Sections .....	89
6.4.3 PTW Imaging of Superficial Nanoroses and Lipid Deposits in Atherosclerotic Plaques .....	90
6.4.4 Multi-Frequency PTW Imaging in Combination with OCT.....	95
6.5 Discussion .....	97
6.6 Conclusion .....	101
6.7 Acknowledgements.....	102
6.8 References.....	102
 Chapter 7 Two-photon Luminescence (TPL) Microscopy Combined with OCT for Macrophage Detection in the Hypercholesterolemic Rabbit Aorta Using Gold Nanoparticles .....	111
7.1 Abstract .....	111
7.2 Introduction.....	112
7.3 Materials and Methods.....	115
7.3.1 Synthesis of Imaging Contrast Agent (Nanorose) .....	115
7.3.2 Preparation of Macrophage Cell Culture and Rabbit Arterial Tissues.....	116
7.3.3 Experimental Setup.....	118
7.3.4 Histology Analysis.....	120
7.4 Results.....	120
7.4.1 TPL Microscopy of Nanorose-loaded Macrophages in Cell Culture.....	120
7.4.2 Imaging Ex Vivo Rabbit Tissues .....	121
7.5 Discussion.....	126
7.6 Conclusion .....	129
7.7 Acknowledgements.....	129
7.8 References.....	130
 Chapter 8 Conclusions and Future Studies .....	138
8.1 Conclusions.....	138
8.1.1 Measurement of Optical Properties of Nanorose.....	138
8.1.2 Dual-wavelength Multi-frequency PTW Imaging Combined	

with OCT for Macrophage and Lipid Detection in Atherosclerotic Plaques Using Gold Nanoparticles .....	138
8.1.3 Combined TPLM and OCT for Macrophage Detection in the Hypercholesterolemic Rabbit Aorta Using Plasmonic Gold Nanorose .....	139
8.2 Future studies .....	140
8.2.1 3-D Reconstruction Algorithm for Swept-frequency PTW Imaging .....	140
8.2.2 Optimization of Imaging Contrast Agent .....	140
8.2.3 Realization of Intravascular Imaging of Atherosclerotic Plaques .....	141
Bibliography .....	143
Vita.....	169

## List of Tables

Table 2.1.	Comparison of cardiovascular imaging techniques in terms of penetration depth, spatial resolution and temporal resolution. ....	18
Table 2.2.	Cellular/molecular targets and contrast agents for atherosclerosis imaging. ....	21

## List of Figures

- Figure 2.1. (a) World map showing the global distribution of CVD mortality rates in males (age standardized, per 100,000). (b) World map showing the global distribution of CVD mortality rates in females (age standardized, per 100,000). Figure adapted from [3]. .....12
- Figure 2.2. Death rate in males (left) and females (right) for total CVD and total deaths in selected countries. Figure adapted from [4]. .....13
- Figure 2.3. The development of an atherosclerotic plaque. The progression of an atherosclerotic lesion is shown in a simplified form, developing from a normal blood vessel (far left) to a vessel with an atherosclerotic plaque and superimposed thrombus (far right). Potential targets for molecular imaging at each stage are also listed. AHA, American Heart Association; ICAM1, intercellular adhesion molecule 1; LDL, low-density lipoprotein; MMP, matrix metalloproteinase; VCAM1, vascular cell-adhesion molecule 1. Figure adapted from [12]. .....14
- Figure 4.1. (a) Digital image of a piece of abdominal artery. (b) Top view infrared image of a segment on an abdominal artery before laser irradiation (surface in the image is intimal layer of the artery). .....46
- Figure 4.2. Schematic diagram of PTW imaging instrumentation to measure the IR signal of the aortic tissue in response to periodic laser irradiation (800 nm and 1210 nm respectively). .....49
- Figure 4.3. (a) Amplitude image at 800 nm laser irradiation (arrows point to the positions of nanoroses). (b) Amplitude image at 1210 nm laser irradiation (arrows point to the positions of lipid deposits). .....50

Figure 4.4. (a) Overlay of 800 nm and 1210 nm amplitude images (red color indicates nanorose, yellow line indicates the edges of lipid deposits). (b) Histology image of RAM-11 stain along the blue line at the region of 3C in (a). Brown color indicates macrophages (arrows point to accumulation positions of macrophages).....51

Figure 4.5. (a) Sample of atherosclerotic aorta of a Zealand white rabbit. (b) Reconstructed OCT image of the same atherosclerotic tissue in Figure 2. Arrow points to the plaque. (c) Schematic diagram of PTW imaging instrumentation to measure the IR signal of the aortic tissue in response to frequency modulated laser irradiation. ....57

Figure 4.6. (a), (b), (c) FFT amplitude images of a segment of atherosclerotic tissue at modulation frequencies of 0.1, 1 and 5 Hz respectively. (d), (e), (f) FFT phase images of the same tissue at modulation frequencies of 0.1, 1 and 5 Hz respectively. Scale bar is 5 mm. ....58

Figure 4.7. Side view (a) and cross-section view (b) of PDMS tissue phantoms. The two-layered geometry consists of top-layer (①), nanoroses (②) and substrate (③).....61

Figure 4.8. Pixel temperature response at nanorose location in response to swept-frequency laser modulation irradiation (800 nm). ....63

Figure 4.9. Reconstructed three-dimensional amplitude PTW images of nanoroses located at a 130  $\mu\text{m}$  depth in PDMS tissue phantom before (a) and after (c) background subtraction; Reconstructed three-dimensional phase PTW images of nanoroses located at 130  $\mu\text{m}$  depth before (b) and after (d) background subtraction. ....63



Figure 4.10. Reconstructed three-dimensional amplitude PTW images with nanoroses embedded in PDMS tissue phantoms at depths of (a) 130 $\mu\text{m}$ , (b) 450 $\mu\text{m}$ and (c) 930 $\mu\text{m}$ . .....	64
Figure 5.1. (a) Absorbance spectrum of NR colloidal suspension. Inset shows a SEM image of one NR cluster with scale bar. (b) Normalized emission spectrum with scale bar of NR-loaded macrophages at 633 nm excitation.....	69
Figure 5.2. Schematic diagrams of (a) SCM (adapted from [12]) and (b) PTW imaging (adapted from [13])......	72
Figure 5.3. (a, d) DIC images, (b, e) fluorescence images (650-760 nm) and (c, f) overlay images of macrophage cell culture with and without NRs. Scale bar is 10 $\mu\text{m}$ . .....	73
Figure 5.4. (a, d) Digital images, (b, e) transmission images and (c, f) fluorescence images (650-760 nm) of rabbit arterial tissue samples with and without NRs. (g) Reconstructed 3-D fluorescence image of red square region in (a). .....	74
Figure 5.5. (a) Amplitude PTW image of the tissue sample as shown in Figure 5.4(a) at a laser modulation frequency of 4 Hz. (b) Amplitude PTW image of the tissue sample as shown in Figure 5.4(d) at a laser modulation frequency of 4 Hz. Scale bar is 2 mm. (c) Average radiometric temperature increases of red square regions in (a, b) in response to laser irradiation within first ten seconds. ....	76

Figure 6.1.	(a) Absorbance spectrum of nanorose colloidal suspension. Inset shows a scanning electron microscopy (SEM) image of a single nanorose cluster. (b) Absorption coefficient spectra of arterial tissues, lipid, water and nanorose. Nanorose concentration was typical of that found inside macrophages on plaque surface, based on surface radiometric temperature measurement in response to a pulsed laser irradiation at 800 nm [23].	83
Figure 6.2.	Schematic diagrams of (a) PTW imaging instrumentation to measure the IR signal from plaques in response to periodic laser irradiation (800 and 1210 nm) and (b) intensity OCT system to measure plaque surface structure. SS: swept source.	86
Figure 6.3.	TEM images of (a) peritoneal macrophages loaded with nanorose and (b) peritoneal macrophages without nanorose. Red arrow points to a lysosome which is magnified in a red square at the upper right corner in (a) where single nanorose and nanorose clusters are observed. Scale bar is 2 $\mu\text{m}$ .	89
Figure 6.4.	Co-registered TPL images of an unstained histological section of plaque from the Positive group. (a) TPL images of plaque measured at emission wavelengths shorter than 570 nm (green). (b) TPL images of nanoroses measured via a 700 nm band-pass filter (red). (c) Merged image of (a) and (b). Yellow arrows in (c) point to nanorose locations. SP: short-pass (<570 nm); BP: band-pass (700/75 nm).	90

Figure 6.5. Amplitude (a,b,c,d) and phase (e,f,g,h) PTW images of atherosclerotic plaques from Positive and Control groups respectively at 800 and 1210 nm laser irradiation. Laser modulation frequency is 4 Hz. Red arrows point to the position of nanoroses in (a) and lipid deposits in (b, d). Red squares indicate regions with and without nanorose in (a) and (c), respectively. Scale bar is the same in (a,b,e,f) and (c,d,g,h), respectively. ....91

Figure 6.6. (a) Average radiometric temperature increase in response to 800 nm laser irradiation at a modulation frequency of 4 Hz measured from plaque area containing nanorose (bright regions in the red square in Figure 6.5(a)) in the Positive group and area with no nanorose (red square in Figure 6.5(c)) in the Control group. (b) Radiometric temperature increase per pulse at a laser modulation frequency of 4 Hz from all plaque segments in Positive and Control groups, respectively. Data are given as mean±SD.....92

Figure 6.7. (a) Overlay of amplitude PTW images from Figure 6.5(a) and 5(b). Red color indicates nanorose. (b,c) Histological sections of plaque from the Positive group with RAM-11 stain along blue and yellow dashed lines in regions 2A and 4B respectively in (a). (d) Histological section of plaque from the Control group with RAM-11 stain. Brown color in (b) and (d) indicates macrophages. (e,f,g), (h,i,j), (k,l,m) Merged TPL images of unstained histological section adjacent to the section in (b), (c) and (d), respectively. Red square region in (b), (c) and (d) corresponds to (e), (h) and (k), respectively. Yellow square region in (e), (h) and (k) corresponds to (f), (i) and (l), respectively. Blue square region in (f), (i) and (l) corresponds to (g), (j) and (m), respectively. Inset in (g) shows co-localized RAM-11 stain of (g) magnified from (b). Yellow arrows in (g) point to nanorose locations. Yellow arrow heads in (m) point to lipid droplets. Yellow circle in (m) indicates clusters of macrophages. ...94

Figure 6.8. (a,b,c,d,e,f) Amplitude PTW images of a plaque segment from the Positive group at 800 and 1210 nm laser irradiation, respectively. Laser modulation frequencies are respectively 0.1, 1 and 4 Hz with corresponding thermal diffusion lengths of 600, 200 and 100  $\mu\text{m}$ . Black arrows point to lipid deposits in (d), (e) and (f). (g) Co-registered and merged PTW-OCT image (Video 1, MPEG, 2.5 MB). Red, yellow, and green colors in (g) represent respectively nanorose-loaded macrophages, lipid deposits and both. White arrows point to peak (P) and valley (V) regions of the plaque in (g). Red arrows above (g) indicate direction of blood flow. (h) Histological section with RAM-11 stain along blue dashed line in (g). (i,j,k) Merged TPL images of unstained histological section adjacent to the section in (h). (i), (j) and (k) respectively represents red, yellow and blue square region in (h), (i) and (j). (l) Area percentage of nanorose at shoulders on the upstream versus downstream side of the plaques (N=44) from the Positive group. Larger area percentage of nanorose are observed at plaque shoulders on the upstream side ( $P < 0.01$ ). Yellow arrows in (k) point to nanorose locations. ....97

Figure 6.9. Co-registered TPL images of a nanorose-loaded monocyte-like cell entering the plaque surface from an unstained histological slice of plaque from the Positive group. (a) TPL images of plaque measured at emission wavelengths shorter than 570 nm (green). (b) TPL images of nanoroses measured via a 700 nm band-pass filter (red). (c) Merged image of (a) and (b). Yellow arrow in (c) points to nanorose location. SP: short-pass (<570 nm); BP: band-pass (700/75 nm).....100

Figure 7.1. A: Absorbance spectrum of nanorose colloidal suspension. Inset shows a schematic cartoon (left) and scanning electron microscopy image (right) of a single nanorose cluster. B: TPL emission spectra of nanorose in gelatin (red) and gelatin alone (blue) at an excitation wavelength of 800 nm. Nanorose suspension ( $3.3 \times 10^{11}$  nanoroses/ml) was mixed with 8% (wt/wt) gelatin to make a nanorose-gelatin tissue phantom ( $1.99 \times 10^{11}$  nanoroses/ml). A shortpass filter ( $<750$  nm) was placed in front of the spectrometer detector in order to block the laser line. ....114

Figure 7.2. A: Rabbit model of aorta inflammation with intimal hyperplasia. B: RAM-11 staining of a cross-section of abdominal aorta. C: Amplified view of the black box in (B). Brown color indicates macrophages. D: RAM-11 staining of a cross-section of thoracic aorta. E: A piece of abdominal aorta with intimal hyperplasia. F: An aorta segment ( $8 \times 8 \times 2$  mm<sup>3</sup>) cut from the black box in (E). ....118

Figure 7.3. Schematic diagrams of (A) TPL microscopy and (B) intensity OCT system. ....119

Figure 7.4. Co-registered TPL images of (A,B) nanorose-loaded macrophages and (D,E) control macrophages without nanorose in two channels (red and green). C,F: Merged two-channel images of (A,B) and (D,E) respectively. G: Quadratic dependence of luminescence intensity (red channel) of nanoroses in macrophage cell culture on excitation laser power of 13-30 mW at 800 nm. A slope of 2.07 confirms the TPL process. Yellow circles in (A) indicate macrophage cells. BP: band-pass (700/75 nm); SP: short-pass ( $<570$  nm). ....121

Figure 7.5. A,B,C,D: Digital image, 3-D OCT, PTW imaging and 3-D two-channel TPL microscopy (red box in (A,C)) of an abdominal aorta segment from the Positive rabbit. E,F,G,H: Digital image, 3-D OCT, PTW imaging and 3-D two-channel TPL microscopy (red box in (E,G)) of an abdominal aorta segment from the Control rabbit. I,J: PTW imaging and 3-D two-channel TPL microscopy (red box in (I)) of a liver segment from the Positive rabbit. K,L: PTW imaging and 3-D two-channel TPL microscopy (red box in (K)) of a liver segment from the Control rabbit. Inset in (D,H,J,L) shows a two-channel TPL image at a single depth at an amplified view within the corresponding 3-D TPL image. Right side of (D,H) shows a side view of the corresponding 3-D TPL image. Laser power delivered to the sample is 20 mW in all TPL measurements except insets of (H) 59 mW and (L) 45 mW. ....123

Figure 7.6. A: RAM-11 stain with positive macrophage staining of the black dashed line in Figure 5A. B,C,D: Two-channel TPL images of the red, yellow and blue boxes in (A), (B) and (C) respectively. Red color indicates TPL signals from nanorose. Green color indicates endogenous fluorescence from aorta. Inset in (D) is a co-localized RAM-11 stain image of (D) amplified from (A). E: RAM-11 stain with positive macrophage staining of the black dashed line in Figure 5E. H: TPL image of the red box in (E). F,I: TPL images of the yellow and blue boxes in (H) and (F) respectively. G,J: TPL images of the white and purple boxes in (H) and (G) respectively. Yellow arrows in (D) point to nanoroses. Yellow arrow heads in (D,J) point to lipid droplets. White arrows in (B,H) point to elastin fibers. Yellow circles in (I,J) indicate clusters of macrophage cells defined by dark nuclei. Laser power delivered to the sample is 20 mW. High intensity TPL signals from nanorose in intimal layer (B,C,D) co-localize with corresponding RAM-11 staining of superficial macrophages in the histological section from the Positive rabbit (A), while no TPL signal from nanorose (red color) is observed in the histological section from the Control rabbit (F,G,H,I,J). .....126

Figure 8.1. Nanorose geometries (imaged by TEM) for optimizing two-photon absorption and luminescence. Scale Bar: 50 nm. ....141

Figure 8.2. IVOCT images of a cross-section of a human coronary artery. (A) Thin-cap fibroatheroma overlying a large lipid core is observed at the 1:00-3:00 O’Clock position. (B) A healthy coronary artery. Reconstructed side view of the artery along the white line during a pullback is shown at the bottom of (A) and (B). .....142



## Chapter 1 Introduction

### 1.1 MOTIVATION

Cardiovascular disease (CVD) remains the leading cause of deaths worldwide [1]. Mortality data show that CVD as the underlying cause of death (including congenital cardiovascular defects) accounted for 33.6% (813,804) of all 2,423,712 deaths in 2007 or 1 of every 3 deaths in the United States [2]. The American Heart Association estimated the total direct and indirect cost of CVD in the United States for 2010 was \$503.2 billion [3] or about 3.5% of the GDP. Atherosclerosis, one of the most common CVD, can lead to myocardial infarction, stroke and progression of peripheral artery disease. The American Heart Association recognizes six stages of an atherosclerotic lesion [4]: Type I lesions are present even in children, and are composed of isolated foam cells in the arterial wall. Type II lesions are also known as fatty streak lesions and feature more foam cells. Type III lesions feature pools of fatty material located outside the cells, and can be present in young adults. Type IV lesions are called atheromas (atherosclerotic plaques) and have a core of cell-free lipid (fat). Type V lesions are known as fibroatheromas and are surrounded by fibrous tissue and may also contain calcifications, which make the arteries remarkably hard and inflexible. Type V lesions are present in older adults. Type VI lesions are complicated and include surface defects, blood clotting activity, and may result in formation of blood clots that can break off and be transported to other parts of the body by the blood stream. Although the disease process tends to be slow and progress over decades, conditions usually remain asymptomatic until an atheroma ruptures, which leads to immediate blood clotting at the site of atheroma rupture. Plaque rupture triggers a cascade of events that leads to clot enlargement, which may quickly obstruct the flow of blood. A complete blockage leads to ischemia of the myocardial (heart) muscle and damage. This process is termed a myocardial infarction or "heart attack". In 2004,

approximately 157,000 heart attacks were fatal in the United States [5]. One study indicated that approximately half of cardiac deaths occur within one hour of symptom onset, before patients reach a hospital [6].

Many of the cellular and molecular events that lead to rupture of atherosclerotic plaques, thrombus formation and consequent acute myocardial infarction are now understood and being utilized to develop novel imaging approaches. Several features of the inflammatory process have been identified that contribute to mechanical instability and increased risk of plaque remodeling and subsequent rupture. For instance, accumulations of macrophages in atherosclerotic plaques over-express matrix metalloproteinases (MMPs), such as MMP-1 (collagenase-1), MMP-3 (stromelysin-1), and MMP-9 (gelatinase-B) [7-10]. Over-expression of such matrix-degrading enzymes is believed to contribute to instability of atherosclerotic plaques and thrombogenicity [11-13]. Therefore, the macrophage is an important early cellular marker that indicates and contributes to increased risk of plaque remodeling and subsequent rupture in the coronary, cerebral, and peripheral circulations.

Inasmuch as atherosclerosis is an inflammatory disease of the arterial wall, ability to identify macrophages in vulnerable atherosclerotic plaques before rupture is a cornerstone of early diagnosis. Currently, many imaging modalities have been investigated to detect vulnerable plaques. Non-invasive imaging modalities include magnetic resonance imaging (MRI), computed tomography (CT) and positron-emission tomography (PET). Catheter-based minimally-invasive imaging modalities include near-infrared fluorescence (NIRF) imaging, intravascular ultrasound (IVUS), intravascular photoacoustic imaging (IVPA) and intravascular optical coherence tomography (IVOCT) [14-19]. However, none of these approaches has been used to image macrophages in vulnerable plaques with high resolution, high sensitivity and high specificity. Therefore,

development of a diagnostic imaging technique that can simultaneously reveal both plaque cellular composition (e.g., macrophages) and anatomical structure is critical to identify vulnerable plaques and would allow the determination of macrophage density in longitudinal studies in response to therapies without cutting tissue. Moreover, clinical validation of such an imaging technique would enable detection and treatment of atherosclerotic plaques at an early stage and, thus, reduce the risk of future myocardial infarction.

## 1.2 RESEARCH OBJECTIVES

The principal goal of my research is to develop hybrid optical imaging modalities (i.e., photothermal wave (PTW) imaging combined with optical coherence tomography (OCT), two-photon luminescence microscopy (TPLM) combined with OCT), and assess the ability of such hybrid imaging modalities to reveal both cellular composition (e.g., macrophages (having taken up plasmonic gold nanoparticles as a contrast agent) and lipid deposits) and anatomical structure of atherosclerotic plaques.

Objectives of my research are achieved through the following specific aims:

- (1) Measure the optical properties of nanorose as an imaging contrast agent for PTW imaging to target macrophages.
- (2) Investigate dual-wavelength multi-frequency/swept-frequency PTW imaging in detecting macrophages and lipid deposits in tissue phantoms and *ex vivo* tissues.
- (3) Investigate the capability of PTW imaging combined with OCT to detect nanorose-loaded macrophages associated with lipid deposits at multiple depths in atherosclerotic plaques with respect to plaque surface structure.

- (4) Investigate the capability of TPLM combined with OCT to detect and characterize the three-dimensional distribution of nanorose-loaded macrophages in atherosclerotic plaques with respect to plaque surface structure with a higher spatial resolution compared to PTW imaging.

### 1.3 DISSERTATION OVERVIEW

The dissertation is structurally divided into four parts. The first part reviews current imaging modalities and imaging contrast agent for atherosclerosis detection and targeting (Chapter 2). The second part characterizes the optical properties of nanorose as a contrast agent for PTW imaging to target macrophages (Chapter 3). The third part of the dissertation describes macrophage detection using PTW imaging and fluorescence imaging (Chapters 4 and 5). The fourth part investigates the combination of PTW imaging/TPLM with OCT to reveal both cellular composition (e.g., macrophages and lipid deposits) and anatomical structure of atherosclerotic plaques (Chapters 6 and 7).

In detail, Chapter 2 describes the current status of CVD and pathophysiology of atherosclerosis. Moreover, current imaging techniques for diagnosing atherosclerosis and clinical/pre-clinical imaging contrast agents for atherosclerosis targeting are reviewed.

Chapter 3 describes experimental and simulation procedures of nanorose absorption ( $\sigma_a$ ) and scattering ( $\sigma_s$ ) cross-section measurements. From experimental measurements,  $\sigma_a$  was computed (mean =  $3.1 \times 10^{-14} \text{ m}^2$ , standard deviation =  $0.5 \times 10^{-14} \text{ m}^2$ ). Data suggested that  $\sigma_s$  is much smaller than  $\sigma_a$  and beyond the sensitivity of our measurements. Discrete dipole approximation (DDA) simulation results showed that  $\sigma_a/\sigma_s = 10.5$  for a randomly generated nanorose cluster geometry (30 nm in diameter, 60 gold-coated iron oxide nanoparticles). The ratio of absorption to scattering cross-sections

( $\sigma_a / \sigma_s$ ) from DDA simulation is consistent with our experimental results ( published in *ACS Nano* (Ma LL, Wang T, et al, 2009), *OSA Technical Digest* (Wang T, et al, 2010)).

Chapter 4 introduces three different applications of PTW imaging: (1) fixed-frequency PTW imaging of macrophages and lipid deposits in *ex vivo* tissues. PTW amplitude images were obtained corresponding to 800 nm and 1210 nm laser irradiation. Computed images suggest that the distributions of both nanorose and lipid can be identified in amplitude images at a frequency of 4 Hz. Nanoroses taken up by macrophages are distributed at the edges of lipid deposits. Observation of high concentration of nanoroses in atherosclerotic plaque confirms that nanoroses are present at locations associated with lipid deposits (published in *Proc SPIE* (Wang T, et al, 2010)). (2) multi-frequency PTW imaging of lipid deposits in *ex vivo* tissues. The 1210 nm excitation wavelength was selected to target lipids. The atherosclerotic plaque sample was irradiated at modulation frequencies ranging from 0.1 to 5 Hz to generate PTWs. Amplitude and phase images obtained at each modulation frequency were related to lateral and depth distribution of lipid in the atherosclerotic tissue samples. PTW images recorded from the atherosclerotic plaque suggest that lateral and depth distribution of lipid can be identified by analysis of amplitude and phase images at selected modulation frequencies. The geometric shape of atherosclerotic plaque is associated with distribution of the lipid deposits (published in *Proc BMES* (Wang T, et al, 2010)). (3) swept-frequency PTW imaging of nanorose in tissue phantoms. The excitation wavelength of 800 nm was selected to target nanorose. Tissue phantoms were irradiated at modulation frequencies ranging from 0.04 to 5 Hz to generate PTWs. PTW images recorded from tissue phantoms suggest that three-dimensional distribution of nanorose can be identified by analysis of amplitude and phase images at selected modulation frequencies. Swept-

frequency PTW imaging is able to detect nanoroses as deep as 930  $\mu\text{m}$  (abstract published in *Lasers Surg Med* (Wang T, et al, 2010)).

Chapter 5 explores fluorescence imaging of macrophages in atherosclerotic plaques using plasmonic gold nanorose. A HeNe laser at 633 nm was used as an excitation light source and an acousto-optic beam splitter was utilized to collect fluorescence emission in the 650-760 nm spectral range. Results of scanning confocal microscopy of macrophage cell cultures and *ex vivo* arterial tissue showed that nanoroses produce a strong fluorescence signal. The presence of nanorose in *ex vivo* arterial tissue was further confirmed by PTW imaging. These results suggest that scanning confocal microscopy can identify the presence and location of nanorose-loaded macrophages in atherosclerotic plaques (published in *Proc SPIE* (Wang T, et al, 2011)).

Chapter 6 assesses the ability of combined dual-wavelength multi-frequency PTW imaging and OCT to detect, and further characterize the distribution of macrophages (having taken up plasmonic gold nanorose) and lipid deposits in atherosclerotic plaques. Amplitude PTW images (4 Hz) were merged into a co-registered OCT image, suggesting that superficial nanorose-loaded macrophages are distributed at shoulders on the upstream side of atherosclerotic plaques ( $P < 0.01$ ) at edges of lipid deposits. Results suggest that combined PTW-OCT imaging can simultaneously reveal plaque structure and composition, permitting characterization of nanorose-loaded macrophages and lipid deposits in atherosclerotic plaques (published in *J Biomed Opt* (Wang T, et al, 2012)).

Chapter 7 investigates the ability of combined TPLM and OCT for macrophage detection in the hypercholesterolemic rabbit aorta using plasmonic gold nanorose. Merged two-channel TPL images suggest that nanorose-loaded macrophages are diffusively distributed and mostly detected superficially within 20  $\mu\text{m}$  from the luminal surface of the aorta. OCT images depict detailed surface structure of the diseased aorta.

Results suggest that TPLM combined with OCT can simultaneously reveal macrophage distribution with respect to aorta surface structure, which has the potential to detect vulnerable plaques and monitor plaque-based macrophages overtime during cardiovascular interventions (published in *Lasers Surg Med* (Wang T, et al, 2012)).

Chapter 8 presents conclusions and directions for future studies related to my dissertation research. Several potential research directions are proposed and outlined.

#### 1.4 REFERENCES

- [1] Yusuf S, Reddy S, Ounpuu S, Anand S, "Global burden of cardiovascular diseases: part I: general considerations, the epidemiologic transition, risk factors, and impact of urbanization," *Circulation* 104, 2746-2753 (2001)
- [2] Roger VL, Go AS, Lloyd-Jones DM, Adams RJ, Berry JD, Brown TM, Carnethon MR, Dai S, de Simone G, Ford ES, Fox CS, Fullerton HJ, Gillespie C, Greenlund KJ, Hailpern SM, Heit JA, Ho PM, Howard VJ, Kissela BM, Kittner SJ, Lackland DT, Lichtman JH, Lisabeth LD, Makuc DM, Marcus GM, Marelli A, Matchar DB, McDermott MM, Meigs JB, Moy CS, Mozaffarian D, Mussolino ME, Nichol G, Paynter NP, Rosamond WD, Sorlie PD, Stafford RS, Turan TN, Turner MB, Wong ND, Wylie-Rosett J, "Heart disease and stroke statistics--2011 update : a report from the American Heart Association," *Circulation* 123, e18-e209 (2011)
- [3] Lloyd-Jones D, Adams RJ, Brown TM, Carnethon M, Dai S, De Simone G, Ferguson TB, Ford E, Furie K, Gillespie C, Go A, Greenlund K, Haase N, Hailpern S, Ho PM, Howard V, Kissela B, Kittner S, Lackland D, Lisabeth L, Marelli A, McDermott MM, Meigs J, Mozaffarian D, Mussolino M, Nichol G, Roger VL, Rosamond W, Sacco R, Sorlie P, Stafford R, Thom T, Wasserthiel-Smoller S, Wong

- ND, Wylie-Rosett J, "Heart disease and stroke statistics--2010 update : a report from the American Heart Association," *Circulation* 121, e46-e215 (2010)
- [4] Stary HC, Chandler AB, Dinsmore RE, Fuster V, Glagov S, Insull W Jr, Rosenfeld ME, Schwartz CJ, Wagner WD, Wissler RW, "A definition of advanced types of atherosclerotic lesions and a histological classification of atherosclerosis. A report from the Committee on Vascular Lesions of the Council on Arteriosclerosis, American Heart Association," *Circulation*, 92(5), 1355-74 (1995)
- [5] Heart disease and stroke statistics - 2008 update, American Heart Association, Available at [http://www.americanheart.org/downloadable/heart/1200078608862HS\\_Stats%202008.final.pdf](http://www.americanheart.org/downloadable/heart/1200078608862HS_Stats%202008.final.pdf)
- [6] Zheng ZJ, Croft JB, Giles WH, Mensah GA, "Sudden cardiac death in the United States, 1989 to 1998," *Circulation* 104, 2158-2163 (2001)
- [7] Johnson JL, George SJ, Newby AC, Jackson CL, "Divergent effects of matrix metalloproteinases 3, 7, 9, and 12 on atherosclerotic plaque stability in mouse brachiocephalic arteries," *Proc Natl Acad Sci* 102, 15575-15580 (2005)
- [8] Henney AM, Wakeley PR, Davies MJ, Foster K, Hembry R, Murphy G, Humphries S, "Localization of stromelysin gene expression in atherosclerotic plaques by in situ hybridization," *Proc Natl Acad Sci* 88, 8154-8158 (1991)
- [9] Galis ZS, Sukhova GK, Lark MW, Libby P, "Increased expression of matrix metalloproteinases and matrix degrading activity in vulnerable regions of human atherosclerotic plaques," *J Clin Invest* 94, 2493-2503 (1994)
- [10] Nikkari ST, O'Brien KD, Ferguson M, Hatsukami T, Welgus HG, Alpers CE, Clowes AW, "Interstitial collagenase (MMP-1) expression in human carotid atherosclerosis," *Circulation* 92,1393-1398 (1995)



- [11] Libby P, Geng YJ, Aikawa M, Schoenbeck U, Mach F, Clinton SK, Sukhova GK, Lee, RT, "Macrophages and atherosclerotic plaque stability," *Curr Opin Lipidol* 7, 330-335 (1996)
- [12] Taubman MB, Fallon JT, Schechter AD, Giesen P, Mendlowitz M, Fyfe BS, Marmur JD, Nemerson Y, "Tissue factor in the pathogenesis of atherosclerosis," *Thromb Haemost* 78, 200-204 (1997)
- [13] Kolodgie FD, Virmani R, Burke AP, Farb A, Weber DK, Kutys R, Finn AV, Gold HK, "Pathologic assessment of the vulnerable human coronary plaque," *Heart* 90, 1385-1391 (2004)
- [14] Trivedi RA, Mallawarachi C, U-King-Im JM, Graves MJ, Horsley J, Goddard MJ, Brown A, Wang L, Kirkpatrick PJ, Brown J, Gillard JH, "Identifying inflamed carotid plaques using in vivo USPIO-enhanced MR imaging to label plaque macrophages," *Arterioscler Thromb Vasc Biol* 26, 1601-1606 (2006)
- [15] Hyafil F, Cornily J, Feig JE, Gordon R, Vucic E, Amirbekian V, Fisher EA, Fuster V, Feldman LJ, Fayad ZA, "Noninvasive detection of macrophages using a nanoparticulate contrast agent for computed tomography," *Nat Med* 13(5), 636-641 (2007)
- [16] Tawakol A, Migrino RQ, Bashian GG, Bedri S, Vermylen D, Cury RC, Yates D, LaMuraglia GM, Furie K, Houser S, Gewirtz H, Muller JE, Brady TJ, Fischman AJ, "In vivo 18F-fluorodeoxyglucose positron emission tomography imaging provides a noninvasive measure of carotid plaque inflammation in patients," *J Am Coll Cardiol* 48, 1818-1824 (2006)
- [17] Jaffer FA, Kim DE, Quinti L, Tung CH, Aikawa E, Pande AN, Kohler RH, Shi GP, Libby P, Weissleder R, "Optical visualization of cathepsin K activity in

atherosclerosis with a novel, protease-activatable fluorescence sensor," *Circulation* 115, 2292-2298 (2007)

[18] Sethuraman S, Aglyamov SR, Amirian JH, Smalling RW, Emelianov SY, "Intravascular photoacoustic imaging using an IVUS imaging catheter," *IEEE Trans Ultrason Ferroelectr Freq Control* 54, 978-986 (2007)

[19] Tearney GJ, Yabushita H, Houser SL, Aretz HT, Jang I, Schlendorf KH, Kauffman CR, Shishkov M, Halpern EF, Bouma BE, "Quantification of macrophage content in atherosclerotic plaques by optical coherence tomography," *Circulation* 107, 113-119 (2003)

## **Chapter 2 Background**

This chapter provides a brief overview of the current status of cardiovascular disease and pathophysiology of atherosclerosis. Subsequently, current imaging techniques for diagnosing atherosclerosis and clinical/pre-clinical imaging contrast agents for atherosclerosis targeting are reviewed.

### **2.1 CARDIOVASCULAR DISEASE**

#### **2.1.1 Current Status of Cardiovascular Disease**

Cardiovascular disease (CVD) or heart disease is a class of diseases that involve the heart or blood vessels (arteries and veins) [1]. While the term technically refers to any disease that affects the cardiovascular system, the term is usually used to refer to those conditions related to atherosclerosis.

CVD remains the leading cause of deaths worldwide [2]. Figure 2.1 shows the global distribution of CVD mortality rates in males and females reported by the World Health Organization (WHO) [3]. According to WHO estimates, in 2002, 16.7 million people around the globe died of CVD [4]. In the United States, CVD accounted for 33.6% (813,804) of all 2,423,712 deaths or 1 of every 3 deaths in 2007 [5]. Figure 2.2 shows the death rate in males and females for total CVD and total deaths in selected countries reported by WHO [4]. By 2020, CVD and stroke is expected to become the leading cause of both death and disability worldwide, with the number of fatalities projected to increase to over 20 million a year and by 2030 to over 24 million a year [6].

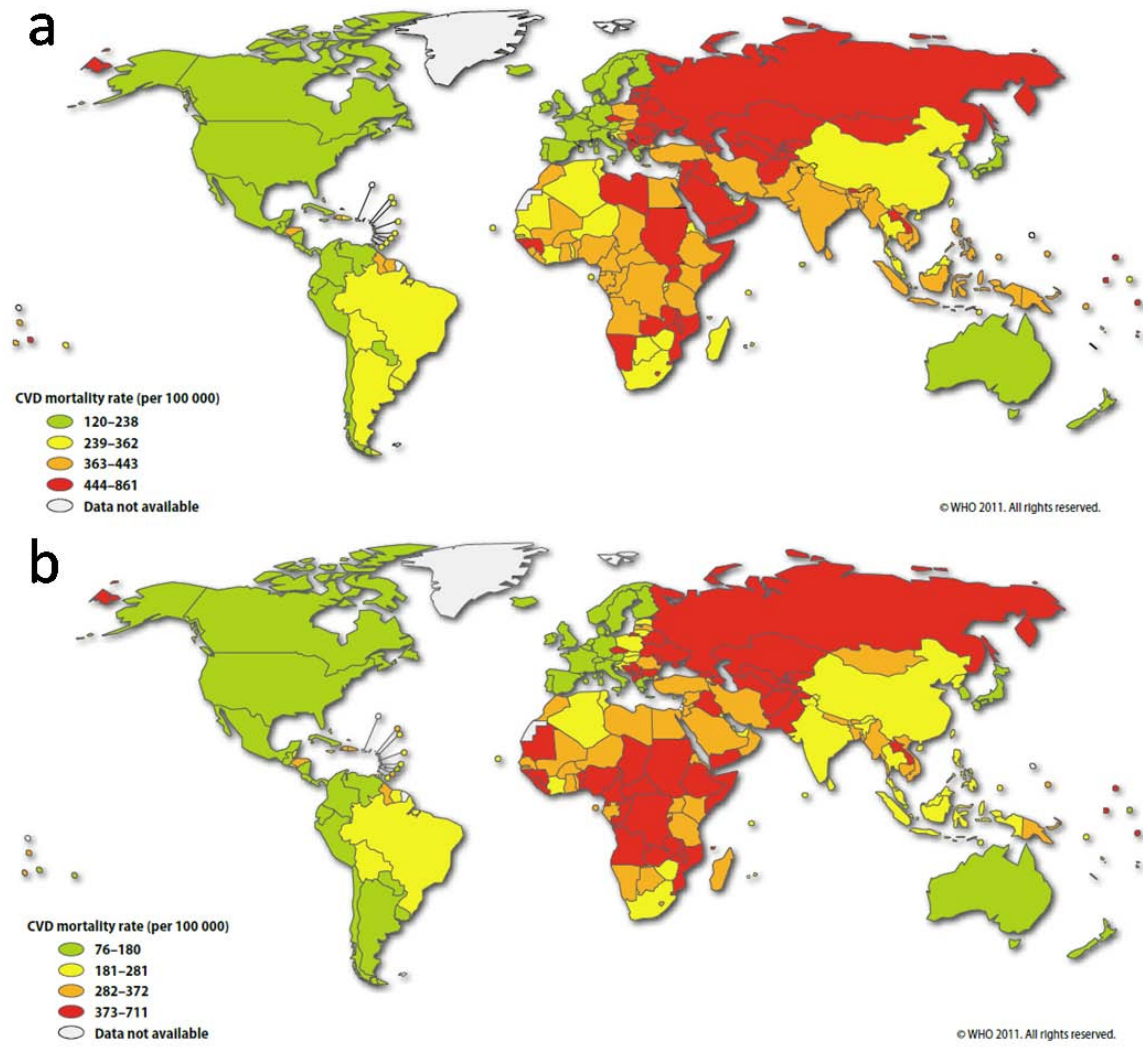


Figure 2.1. (a) World map showing the global distribution of CVD mortality rates in males (age standardized, per 100,000). (b) World map showing the global distribution of CVD mortality rates in females (age standardized, per 100,000). Figure adapted from [3].

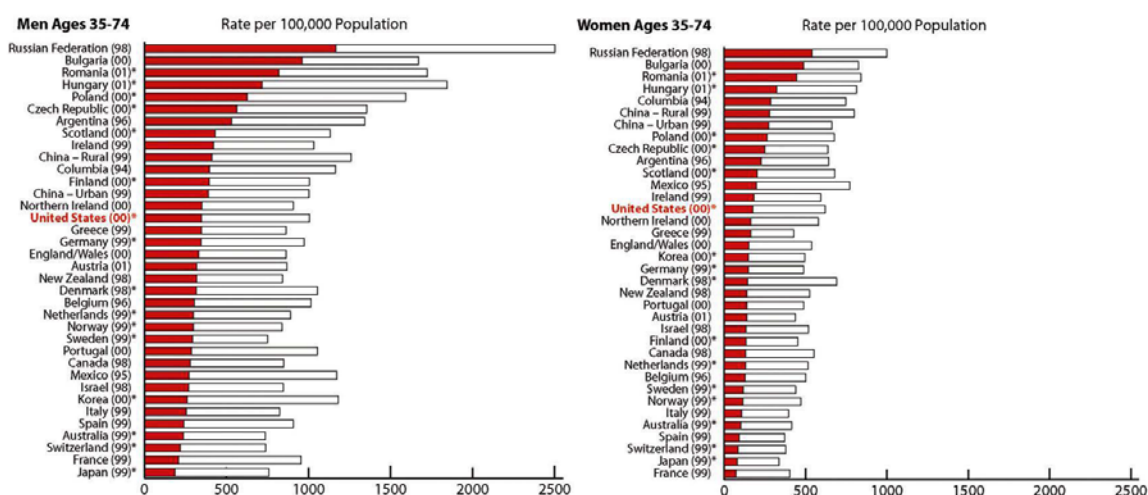


Figure 2.2. Death rate in males (left) and females (right) for total CVD and total deaths in selected countries. Figure adapted from [4].

### 2.1.2 Pathophysiology of Atherosclerosis

Atherosclerosis and plaque rupture leads to myocardial infarction, stroke and progression of peripheral artery disease. Atherosclerotic lesions (plaques) are asymmetric focal thickenings of the innermost layer of the artery - the intima. Plaques consist of cells, connective-tissue elements, lipids and debris. An atherosclerotic plaque is preceded by a fatty streak, an accumulation of lipid-laden cells beneath the endothelium. Most of these cells in the fatty streak are macrophages, together with some T cells [7]. Many investigators once believed that progressive luminal narrowing or stenosis beginning from increased lipid storage and continued growth of smooth-muscle cells in the plaque was the main cause of myocardial infarction [8]. Recent advances in basic and experimental science have established a fundamental role that inflammation and underlying cellular and molecular mechanisms [9-11] contribute to atherogenesis from initiation through progression, plaque rupture and ultimately, thrombosis. The principal pathologic features and progression stages (see Section 1.1) of atherosclerotic plaques that are prone to rupture are now well described (Figure 2.3) [12].



Many of the cellular and molecular events that lead to rupture of thin-cap fibroatheromas, thrombus formation and consequent acute myocardial infarction are understood and being utilized to develop novel imaging approaches. Several features of the inflammatory process have been identified that contribute to mechanical instability and increased risk of plaque remodeling and subsequent rupture, including: infiltration and retention of low-density lipoprotein (LDL) [18-19], activation of endothelial cells [20], over-expression of adhesion molecules such as vascular cell adhesion molecule 1 (VCAM-1) and chemokines [21-22], activation and recruitment of macrophages [23-25], a decrease in smooth muscle cells (SMCs) and collagen synthesis [26-27], and thinning of the fibrous cap overlying a large lipid core [28]. Accumulations of macrophages in atherosclerotic plaques over-express matrix metalloproteinases (MMPs), such as MMP-1 (collagenase-1), MMP-3 (stromelysin-1), and MMP-9 (gelatinase-B) [29-32]. Over-expression of such matrix-degrading enzymes is believed to contribute to instability of thin-cap fibroatheromas and increase thrombogenicity [33-35]. Therefore, the macrophage is an important early cellular marker that indicates and contributes to increased risk of plaque remodeling and subsequent rupture in the coronary, cerebral, and peripheral circulations.

## **2.2 DIAGNOSIS AND TREATMENT OF ATHEROSCLEROSIS**

### **2.2.1 Current Imaging Modalities for Atherosclerosis Detection**

Traditionally, diagnosis of atherosclerosis was possible only at advanced stages of lesions by directly revealing the morphological changes of blood vessels (e.g., narrowing of the vessel lumen). However, new imaging approaches allow the assessment not only of the morphology of blood vessels but also of the composition of the vessel walls, enabling observation of atherosclerosis-associated pathological alterations in the arteries, down to

the cellular and molecular level in some cases. Some of these approaches are now in clinical use or are being tested in clinical trials, whereas others are better suited to basic and translational research. In this section, recent advances in imaging modalities for atherosclerosis detection are discussed. First, non-invasive imaging techniques (i.e., computed tomography (CT), magnetic resonance imaging (MRI), positron emission tomography (PET) and single-photon-emission CT (SPECT)) are described. Then the growing field of minimally-invasive imaging techniques (i.e., intravascular ultrasound (IVUS), intravascular photoacoustic imaging (IVPA), fluorescence lifetime imaging (FLIM), intravascular optical coherence tomography (IVOCT)) and invasive microscopic techniques (i.e., non-linear optical microscopy (NLOM)) are investigated.

As lipids presents lower X-ray absorption, atherosclerotic plaques can be characterized by CT as hypo-dense, dense or calcified [36]. Recently, CT has been demonstrated to detect macrophages in the blood vessel wall using an iodinated nanoparticulate contrast agent [37]. Similarly, MRI is also able to depict plaque presence, size and morphology but without exposing the patient to ionizing radiation like CT [38]. Although MRI can achieve macrophage imaging [39-40], relatively large amounts of contrast agents (2 to 20 mg Fe/kg) are required. PET, however, provides detection sensitivities an order of magnitude higher than MRI, enabling the use of radioactive contrast agent at lower concentrations. The combination of PET and CT has the potential to map macrophage infiltration onto anatomic vascular structures [41-42]. SPECT presents comparable sensitivity to PET, but also requires the use of radioactive contrast agent to track macrophage recruitment to atherosclerotic plaques [43].

Intravascular imaging techniques are minimally-invasive. IVUS can perform virtual histology by using spectral analysis to identify plaque components [44-45]. By detecting laser-induced thermal expansion ultrasonically, IVPA is able to map



macrophages onto an IVUS image using contrast agent [46]. FLIM is used to measure the autofluorescence and can assess the biochemical composition (e.g., MMPs) of atherosclerotic plaques [47]. IVOCT has been demonstrated to visualize microstructural features atherosclerotic plaques with high resolution [48-51] and is currently the sole approach that provides sufficient spatial resolution to image thin-cap fibroatheromas *in vivo*.

NLOM including two-photon luminescence microscopy (TPLM), second harmonic generation (SHG) and coherent antistokes Raman scattering (CARS) microscopy uses nonlinear optical properties of tissue and has been recently utilized to image plaque components such as endothelial cells, smooth muscle cells [52], elastin fibers [53-54], oxidized LDL [55] and lipid droplets [56] based on their endogenous autofluorescence. Up to now, NLOM provides the highest spatial resolution than other cardiovascular imaging techniques despite its invasive nature.

A comparison of penetration depth, spatial resolution and temporal resolution of the imaging techniques discussed above are summarized in Table 2.1 below [57-64].

<b>Imaging Techniques</b>	<b>Penetration Depth</b>	<b>Spatial Resolution (Lateral/Axial)</b>	<b>Temporal Resolution</b>
<b>CT</b>	several cm	0.1-0.29 mm/0.1-1 mm	~10 fps
<b>MRI</b>	several cm	0.04-0.5 mm/0.3-0.5 mm	~30 fps
<b>PET</b>	several cm	1-4 mm/1-4 mm	<5 fps
<b>SPECT</b>	several cm	3 mm/3 mm	<1 fps
<b>IVUS</b>	4-7.6 mm	100 $\mu$ m/20-50 $\mu$ m	30 fps
<b>IVPA</b>	3 mm	100 $\mu$ m/25 $\mu$ m	1 fps
<b>FLIM</b>	superficial	100 $\mu$ m/NA	10 fps
<b>IVOCT</b>	1-2 mm	10 $\mu$ m/10-20 $\mu$ m	60 fps
<b>TPLM</b>	200 $\mu$ m	0.3 $\mu$ m/1 $\mu$ m	< 50 fps
<b>SHG</b>	550 $\mu$ m	0.5 $\mu$ m/1-1.9 $\mu$ m	< 50 fps
<b>CARS</b>	500 $\mu$ m	0.5 $\mu$ m/1 $\mu$ m	< 50 fps

Table 2.1. Comparison of cardiovascular imaging techniques in terms of penetration depth, spatial resolution and temporal resolution.

Although CT/MRI/PET/SPECT can assess atherosclerosis non-invasively, IVUS/IVOCT have higher spatial and temporal resolution, IVPA/FLIM can obtain plaque biochemical information, none of these techniques is able to provide cellular or subcellular resolution. TPLM/SHG/CARS are superior in terms of spatial resolution, however, endogenous fluorescence contrast does not provide sufficient specificity to target macrophages in atherosclerotic plaques. Therefore, an imaging technique that can reveal both plaque cellular composition (e.g., macrophages and lipid deposits) and anatomical structure with high resolution, sensitivity and specificity is of great interest for clinical applications.

### 2.2.2 Medical Treatment of Atherosclerosis

Atherosclerosis treatment usually begins with lifestyle changes, such as a healthy diet, exercising regularly, cessation of smoking, and maintaining a healthy body weight [65-72]. In addition, medications or surgical procedures may be undertaken. Various pharmacological interventions can slow, or even reverse the effects of atherosclerosis, including: cholesterol reduction, anti-platelet, beta-blockers, angiotensin-converting enzyme inhibitors, calcium channel blockers and diuretics [73]. Specifically, clinical trials have shown that lipid lowering by 3-hydroxy-3-methylglutaryl coenzyme A (HMG-CoA) reductase inhibitors or statins can reduce acute coronary events and mortality rates in many individuals [74-77]. More aggressive interventions including surgery may be needed if severe symptoms are observed, these include: angioplasty, stenting, endarterectomy, thrombolytic therapy and bypass surgery [78]. Although coronary angioplasty can immediately reduce anginal symptoms in almost all patients undergoing therapy, use is associated with nonfatal myocardial infarction or death in about 5% of patients [79-82]. Moreover, restenosis requiring repeated angioplasty or bypass surgery occurs in about 30% [83] of these patients. Several clinical trials have shown that the deployment of coronary stents reduces the occurrence of acute complications and restenosis in patients undergoing coronary angioplasty [84-85]. However, the use of stents as a “plaque sealing” approach was recently criticized by Nissen, arguing that atherosclerosis is fundamentally a systemic inflammatory disease [86]. Nissen suggests that stenting a few vulnerable plaques is not a viable long-term therapeutic approach for cardiovascular disease.

## **2.3 IMAGING CONTRAST AGENTS FOR ATHEROSCLEROSIS TARGETING**

### **2.3.1 A Review of Currently Used Contrast Agents**

In the past decade, cardiovascular imaging has advanced from merely imaging vascular anatomy and physiology to detecting biological processes at the cellular or even molecular level, which relies on the development in three scientific fields: 1) imaging platforms, 2) molecular epitope and ligand identification, and 3) design and use of high-quality contrast agents. As far as the latter is concerned, significant progress is being made for tracking potentially important components of atherosclerotic disease [87-92]. Nano-sized contrast agents provide many advantages over conventional approaches [91]: 1) significant signal amplification due to a number of imaging labels or a combination of labels attached to a single nanoparticle, 2) enhanced binding affinity and specificity by conjugating multiple targeting ligands onto the nanoparticle, and 3) better targeting efficacy by bypassing biological barriers. Currently, most of the available contrast agents are in laboratory testing (especially for optical imaging), although some have already advanced to clinical evaluation and routine use (e.g., for MRI, CT, PET, SPECT). Table 2.2 summarizes currently developed contrast agents, their cellular or molecular targets and applications in various imaging modalities.

Target	Biological Roles	Contrast Agent	Imaging Modality
<b>Macrophages/ Inflammatory cells/MMPs</b>	Crucial in early plaque development, extracellular-matrix formation, angiogenesis, plaque rupture and thrombosis	USPIO	MRI [93]
		N1177	CT [94]
		[ <sup>18</sup> F]Fluoro-deoxyglucose	PET [95]
		<sup>99m</sup> Tc-labelled interleukin-2	SPECT [96]
		Near infrared probe	NIRF [97]
<b>Apoptotic cells</b>	Release pro-coagulant and pro-oxidative stimuli that contribute to plaque destabilization and myocardial injury	Gold NPs	IVPA [98]
		Ironoxide-Cy5.5	MRI/NIRF [99]
<b>Activated endothelium/ Vascular cell-adhesion molecules</b>	Mediate the adhesion of inflammatory cells to the endothelium and the recruitment of these cells into atherosclerotic lesions and injured myocardium	<sup>99m</sup> Tc	SPECT [100]
		USPIO	MRI [101]
		<sup>123</sup> I	PET [102]
<b>Extracellular matrix</b>	An important component of plaques, particularly abundant in advanced lesions	VINP-28	MRI/NIRF [103]
		Microbubbles	Ultrasound [104]
<b>Lipoproteins</b>	Involved in the trafficking of cholesterol between the blood and atherosclerotic plaques	Gadofluorine	MRI [105]
		Fluorescent probe	TPLM [106]
<b>New blood vessels/ Angiogenesis</b>	Contribute to intraplaque haemorrhage, plaque growth and destabilization, and myocardial healing and remodelling	HDL-like NPs	MRI [107]
		<sup>99m</sup> Tc-labelled MDA2	SPECT [108]
<b>Thrombus</b>	A hallmark of acute vascular syndromes, and promote plaque growth	Paramagnetic NPs	MRI [109]
		<sup>99m</sup> Tc-labelled NC100692	SPECT [110]
<b>Thrombus</b>	A hallmark of acute vascular syndromes, and promote plaque growth	EP-1873	MRI [111]
		<sup>99m</sup> Tc-labelled apcitide	SPECT [112]
		IR-786-labelled platelets	NIRF [113]
		Microbubbles	Ultrasound [114]

Table 2.2. Cellular/molecular targets and contrast agents for atherosclerosis imaging.

### 2.3.2 A Novel Contrast Agent: Nanorose

As no endogenous optical absorption or scattering contrast exists between macrophages and other plaque components, in this research, a novel gold nanoparticle called nanorose was utilized to serve as a macrophage targeting chromophore [115]. The nanoclusters were formed by kinetic assembly of gold/iron oxide nanocomposite building blocks with only a small amount of polymeric stabilizers. The closely spaced and asymmetric thin gold coatings on the primary particles and porosity of the nanoclusters favor high NIR absorbance as a result of collective responses of the electrons and reduced symmetry of the interactions between plasmon modes. The details of nanorose optical properties and synthesis procedure are discussed in Chapters 3, 5, 6 and 7.

## 2.4 REFERENCES

- [1] Maton A, (1993), Human Biology and Health, Cliffs E (Ed.), New Jersey: Prentice Hall, ISBN 0-13-981176-1
- [2] Yusuf S, Reddy S, Ounpuu S, Anand S, "Global burden of cardiovascular diseases: part I: general considerations, the epidemiologic transition, risk factors, and impact of urbanization," *Circulation* 104, 2746-2753 (2001)
- [3] Global Atlas on cardiovascular disease prevention and control, World Health Organization, Available at [http://whqlibdoc.who.int/publications/2011/9789241564373\\_eng.pdf](http://whqlibdoc.who.int/publications/2011/9789241564373_eng.pdf)
- [4] Statistical fact sheet - populations, American Heart Association, Available at <http://www.americanheart.org>
- [5] Roger VL, Go AS, Lloyd-Jones DM, Adams RJ, Berry JD, Brown TM, Carnethon MR, Dai S, de Simone G, Ford ES, Fox CS, Fullerton HJ, Gillespie C, Greenlund KJ, Hailpern SM, Heit JA, Ho PM, Howard VJ, Kissela BM, Kittner SJ, Lackland DT, Lichtman JH, Lisabeth LD, Makuc DM, Marcus GM, Marelli A, Matchar DB,

- McDermott MM, Meigs JB, Moy CS, Mozaffarian D, Mussolino ME, Nichol G, Paynter NP, Rosamond WD, Sorlie PD, Stafford RS, Turan TN, Turner MB, Wong ND, Wylie-Rosett J, "Heart disease and stroke statistics - 2011 update: a report from the American Heart Association," *Circulation* 123, e18-e209 (2011)
- [6] Atlas of heart disease and stroke, World Health Organization (2004)
- [7] Stary HC, Chandler AB, Glagov S, Guyton JR, Insull W Jr, Rosenfeld ME, Schaffer SA, Schwartz CJ, Wagner WD, Wissler RW, "A definition of initial, fatty streak, and intermediate lesions of atherosclerosis: a report from the Committee on Vascular Lesions of the Council on Arteriosclerosis," *Circulation* 89, 2462-2478 (1994)
- [8] Libby P, Aikawa M, "Stabilization of atherosclerotic plaques: new mechanisms and clinical targets," *Nat Med* 8, 1257-1262 (2002)
- [9] Libby P, Ridker PM, Maseri A, "Inflammation and Atherosclerosis," *Circulation* 105,1135-1143 (2002)
- [10] Libby P, Theroux P, "Pathophysiology of coronary artery disease," *Circulation* 111, 3481-8 (2005)
- [11] Lucas AR, Korol R, Pepine CJ, "Inflammation in atherosclerosis: some thoughts about acute coronary syndromes," *Circulation* 113, e728-732 (2006)
- [12] Javier Sanz, Zahi A. Fayad, "Imaging of atherosclerotic cardiovascular disease," *Nature* 451, 953-957 (2008)
- [13] Davies MJ, Thomas A, "Thrombosis and acute coronary-artery lesions in sudden cardiac ischemic death," *N Engl J Med* 310, 1137-1140 (1984)
- [14] Virmani R, Burke AP, Kolodgie FD, Farb A, "Pathology of the thin-cap fibroatheroma: a type of vulnerable plaque," *J Interv Cardiol* 16(3), 267-272 (2003)

- [15] Davies MJ, Richardson PD, Woolf N, Katz DR, Mann J, "Risk of thrombosis in human atherosclerotic plaques: role of extracellular lipid, macrophage, and smooth muscle cell content," *Br Heart J* 69, 377-381 (1993)
- [16] Stary HC, Chandler AB, Dinsmore RE, "A definition of advanced types of atherosclerotic lesions and a histological classification of atherosclerosis: a report from the Committee on Vascular Lesions of the Council on Arteriosclerosis," *Circulation* 92, 1355-1374 (1995)
- [17] Jonasson L, Holm J, Skalli O, Bondjers G, Hansson GK, "Regional accumulations of T cells, macrophages, and smooth muscle cells in the human atherosclerotic plaque," *Arteriosclerosis* 6, 131-138 (1986)
- [18] Skalen K, Gustafsson M, Rydberg EK, Hultén LM, Wiklunda O, Innerarity TL, Borén J, "Subendothelial retention of atherogenic lipoproteins in early atherosclerosis," *Nature* 417, 750-754 (2002)
- [19] Leitinger N, "Oxidized phospholipids as modulators of inflammation in atherosclerosis," *Curr Opin Lipidol* 14, 421-430 (2003)
- [20] Eriksson EE, Xie X, Werr J, Thoren P, Lindbom L, "Importance of primary capture and L-selectin-dependent secondary capture in leukocyte accumulation in inflammation and atherosclerosis in vivo," *J Exp Med* 194, 205-218 (2001)
- [21] Kinlay S, Libby P, Ganz P, "Endothelial function and coronary artery disease," *Curr Opin Lipidol* 12, 383-389 (2001)
- [22] Cybulsky MI, Iiyama K, Li H, Zhu S, Chen M, Liyama M, Davis V, Gutierrez-Ramos JC, Connelly PW, Milstone DS, "A major role for VCAM-1, but not ICAM-1, in early atherosclerosis," *J Clin Invest* 107, 1255-1262 (2001)



- [23] Smith JD, Trogan E, Ginsberg M, Grigaux C, Tian J, Miyata M, "Decreased atherosclerosis in mice deficient in both macrophage colony-stimulating factor (op) and apolipoprotein E," *Proc Natl Acad Sci* 92, 8264-8268 (1995)
- [24] Boring L, Gosling J, Cleary M, Charo IF, "Decreased lesion formation in CCR2-/- mice reveals a role for chemokines in the initiation of atherosclerosis," *Nature* 394, 894-897 (1998)
- [25] Gu L, Okada Y, Clinton SK, Gerard C, Sukhova GK, Libby P, Rollins BJ, "Absence of monocyte chemoattractant protein-1 reduces atherosclerosis in low density lipoprotein receptor-deficient mice," *Mol Cell* 2, 275-281 (1998)
- [26] Fukumoto Y, Libby P, Rabkin E, Hill CC, Enomoto M, Hirouchi Y, Shiomi M, Aikawa M, "Statins alter smooth muscle cell accumulation and collagen content in established atheroma of watanabe heritable hyperlipidemic rabbits," *Circulation* 103, 993-999 (2001)
- [27] Davies MJ, Richardson PD, Woolf N, Katz DR, Mann J, "Risk of thrombosis in human atherosclerotic plaques: role of extracellular lipid, macrophage, and smooth muscle cell content," *Br Heart J* 69, 377-381 (1993)
- [28] van der Wal AC, Becker AE, van der Loos CM, Das PK, "Site of intimal rupture or erosion of thrombosed coronary atherosclerotic plaques is characterized by an inflammatory process irrespective of the dominant plaque morphology," *Circulation* 89, 36-44 (1994)
- [29] Johnson JL, George SJ, Newby AC, Jackson CL, "Divergent effects of matrix metalloproteinases 3, 7, 9, and 12 on atherosclerotic plaque stability in mouse brachiocephalic arteries," *Proc Natl Acad Sci* 102, 15575-15580 (2005)

- [30] Henney AM, Wakeley PR, Davies MJ, Foster K, Hembry R, Murphy G, Humphries S, "Localization of stromelysin gene expression in atherosclerotic plaques by in situ hybridization," *Proc Natl Acad Sci* 88, 8154-8158 (1991)
- [31] Galis ZS, Sukhova GK, Lark MW, Libby P, "Increased expression of matrix metalloproteinases and matrix degrading activity in vulnerable regions of human atherosclerotic plaques," *J Clin Invest* 94, 2493-2503 (1994)
- [32] Nikkari ST, O'Brien KD, Ferguson M, Hatsukami T, Welgus HG, Alpers CE, Clowes AW, "Interstitial collagenase (MMP-1) expression in human carotid atherosclerosis," *Circulation* 92,1393-1398 (1995)
- [33] Libby P, Geng YJ, Aikawa M, Schoenbeck U, Mach F, Clinton SK, Sukhova GK, Lee, RT, "Macrophages and atherosclerotic plaque stability," *Curr Opin Lipidol* 7, 330-335 (1996)
- [34] Taubman MB, Fallon JT, Schechter AD, Giesen P, Mendlowitz M, Fyfe BS, Marmur JD, Nemerson Y, "Tissue factor in the pathogenesis of atherosclerosis," *Thromb Haemost* 78, 200-204 (1997)
- [35] Kolodgie FD, Virmani R, Burke AP, Farb A, Weber DK, Kutys R, Finn AV, Gold HK, "Pathologic assessment of the vulnerable human coronary plaque," *Heart* 90, 1385-1391 (2004)
- [36] Viles-Gonzalez JF, Poon M, Sanz J, Rius T, Nikolaou K, Fayad ZA, Fuster V, Badimon JJ, "In vivo 16-slice, multidetector-row computed tomography for the assessment of experimental atherosclerosis: comparison with magnetic resonance imaging and histopathology," *Circulation* 110, 1467-1472 (2004)
- [37] Hyafil F, Cornily JC, Feig JE, Gordon R, Vucic E, Amirbekian V, Fisher EA, Fuster V, Feldman LJ, Fayad ZA, "Noninvasive detection of macrophages using a

- nanoparticulate contrast agent for computed tomography," *Nature Med* 13(5), 636-41 (2007)
- [38] Khera A, de Lemos JA, Peshock RM, Lo HS, Stanek HG, Murphy SA, Wians FH Jr, Grundy SM, McGuire DK, "Relationship between C-reactive protein and subclinical atherosclerosis: the Dallas Heart Study," *Circulation* 113, 38-43 (2006)
- [39] Nahrendorf M, Jaffer FA, Kelly KA, Sosnovik DE, Aikawa E, Libby P, Weissleder R, "Noninvasive vascular cell adhesion molecule-1 imaging identifies inflammatory activation of cells in atherosclerosis," *Circulation* 114, 1504-1511 (2006)
- [40] Amirbekian V, Lipinski MJ, Briley-Saebo KC, Amirbekian S, Aguinaldo JGS, Weinreb DB, Vucic E, Frias JC, Hyafil F, Mani V, Fisher EA, Fayad ZA, "Detecting and assessing macrophages in vivo to evaluate atherosclerosis noninvasively using molecular MRI," *Proc Natl Acad Sci* 104, 961-966 (2007)
- [41] Okane K, Ibaraki M, Toyoshima H, Sugawara S, Takahashi K, Miura S, Shimosegawa E, Satomi J, Kitamura K, Satoh T, "<sup>18</sup>F-FDG accumulation in atherosclerosis: use of CT and MR co-registration of thoracic and carotid arteries," *Eur J Nucl Med Mol Imaging* 33, 589-594 (2006)
- [42] Nahrendorf M, Zhang H, Hembrador S, Panizzi P, Sosnovik DE, Aikawa E, Libby P, Swirski FK, Weissleder R, "Nanoparticle PET-CT imaging of macrophages in inflammatory atherosclerosis," *Circulation* 117, 379-387 (2008)
- [43] Kircher MF, Grimm J, Swirski FK, Libby P, Gerszten RE, Allport JR, Weissleder R, "Noninvasive in vivo imaging of monocyte trafficking to atherosclerotic lesions," *Circulation* 117, 388-395 (2008)
- [44] Nair A, Kuban BD, Obuchowski N, Vince DG, "Assessing spectral algorithms to predict atherosclerotic plaque composition with normalized and raw intravascular ultrasound data," *Ultrasound Med Biol* 27, 1319-1331 (2001)

- [45] Kenya N, Etsuo T, Osamu K, Vince DG, Renu V, Jean-Francois S, Akira M, Yoshihiro T, Tatsuya I, Mariko E, Tetsuo M, Mitsuyasu T, Takahiko S, "Accuracy of in vivo coronary plaque morphology assessment: a validation study of in vivo virtual histology compared with in vitro histopathology," *J Am Coll Cardiol* 47, 2405-2412 (2006)
- [46] Wang B, Yantsen E, Larson T, Karpouk AB, Sethuraman S, Su JL, Sokolov K, Emelianov SY, "Plasmonic intravascular photoacoustic imaging for detection of macrophages in atherosclerotic plaques," *Nano Lett* 9(6), 2212-7 (2009)
- [47] Phipps JE, Hatami N, Galis ZS, Baker JD, Fishbein MC, Marcu L, "A fluorescence lifetime spectroscopy study of matrix metalloproteinases-2 and -9 in human atherosclerotic plaque," *J Biophotonics* 4, 650-658 (2011)
- [48] Brezinski ME, Tearney GJ, Bouma BE, Boppart SA, Hee MR, Swanson EA, Southern JF, Fujimoto JG, "Imaging of coronary artery microstructure (in vitro) with optical coherence tomography," *Am J Cardiol* 77, 92-93 (1996)
- [49] Raffel OC, Tearney GJ, Gauthier DD, Halpern EF, Bouma BE, Jang IK, "Relationship between a systemic inflammatory markers, plaque inflammation, and plaque characteristics determined by intravascular optical coherence tomography," *Arterioscler Thromb Vasc Biol* 27, 1820-1827 (2007)
- [50] Tanaka A, Imanishi T, Kitabata H, Kubo T, Takarada S, Tanimoto T, Kuroi A, Tsujioka H, Ikejima H, Ueno S, Kataiwa H, Okouchi K, Kashiwagi M, Matsumoto H, Takemoto K, Nakamura N, Hirata K, Mizukoshi M, Akasaka T, "Morphology of exertion-triggered plaque rupture in patients with acute coronary syndrome: an optical coherence tomography study," *Circulation* 118, 2368-2373 (2008)
- [51] Vancraeynest D, Pasquet A, Roelants V, Gerber BL, Vanoverschelde JJ, "Imaging the vulnerable plaque," *J Am Coll Cardiol* 57, 1961-1979 (2011)

- [52] van Zandvoort M, Engels W, Douma K, Beckers L, oude Egbrink M, Daemen M, Slaaf DW, "Two-photon microscopy for imaging of the (atherosclerotic) vascular wall: a proof of concept study," *J Vasc Res* 41, 54-63 (2004)
- [53] Zoumi A, Lu XA, Kassab GS, Tromberg BJ, "Imaging coronary artery microstructure using secondharmonic and two-photon fluorescence microscopy," *Biophys J* 87, 2778-2786 (2004)
- [54] Boulesteix T, Pena AM, Pages N, Godeau G, Sauviat MP, Beaurepaire E, Schanne-Klein MC, "Micrometer scale ex vivo multiphoton imaging of unstained arterial wall structure," *Cytometry Part A* 69A, 20-26 (2006)
- [55] Le TT, Langohr IM, Locker MJ, Sturek M, Cheng JX, "Label-free molecular imaging of atherosclerotic lesions using multimodal nonlinear optical microscopy," *J Biomed Opt* 12(5), 0540071-05400710 (2007)
- [56] Lilledahl MB, Haugen OA, de Lange Davies C, Svaasand LO, "Characterization of vulnerable plaques by multiphoton microscopy," *J Biomed Opt* 12(4), 0440051-04400512 (2007)
- [57] Badea C, Hedlund LW, Johnson GA, "Micro-CT with respiratory and cardiac gating," *Med Phys* 31(12), 3324-3329 (2004)
- [58] Wasserman BA, Astor BC, Sharrett AR, Swingen C, Catellier D, "MRI measurements of carotid plaque in the atherosclerosis risk in communities (ARIC) study: Methods, reliability and descriptive statistics," *J Magn Reson Imaging* 31, 406-415 (2010)
- [59] Nahrendorf M, Zhang H, Hembrador S, Panizzi P, Sosnovik DE, Aikawa E, Libby P, Swirski FK, Weissleder R, "Nanoparticle PET-CT imaging of macrophages in inflammatory atherosclerosis," *Circulation* 117, 379-387 (2008)

- [60] Baird AE, Donnan GA, Austin MC, Fitt GJ, Davis SM, McKay WJ, "Reperfusion after thrombolytic therapy in ischemic stroke measured by single-photon emission computed tomography," *Stroke* 25, 79-85 (1994)
- [61] Karpouk AB, Wang B, Emelianov SY, "Development of a catheter for combined intravascular ultrasound and photoacoustic imaging," *Rev Sci Instrum* 81(1), 014901-014907 (2010)
- [62] Park J, Jo JA, Shrestha S, Pande P, Wan Q, Applegate BE, "A dual-modality optical coherence tomography and fluorescence lifetime imaging microscopy system for simultaneous morphological and biochemical tissue characterization," *Biomed Opt Express* 2 (1), 186-200 (2010)
- [63] Wang T , Mancuso JJ, Sapozhnikova V, Dwelle J, Ma LL, Willsey B, Kazmi SM, Qiu J, Li X, Asmis R, Johnston KP, Feldman MD, Milner TE, "Dual-wavelength multi-frequency PTW imaging combined with OCT for macrophage and lipid detection in atherosclerotic plaques", *J Biomed Opt* (IN PRESS)
- [64] Wang HW, Langohr IM, Sturek M, Cheng JX, "Imaging and quantitative analysis of atherosclerotic lesions by CARS-based multimodal nonlinear optical microscopy," *Arterioscler Thromb Vasc Biol* 29, 1342-1348 (2009)
- [65] The Trials of Hypertension Prevention Collaborative Research Group, "Effects of weight loss and sodium reduction intervention on blood pressure and hypertension incidence in overweight people with high-normal blood pressure, The Trials of Hypertension Prevention, phase II," *Arch Intern Med* 157, 657-67 (1997)
- [66] He J, Whelton PK, Appel LJ, Charleston J, Klag MJ, "Long-term effects of weight loss and dietary sodium reduction on incidence of hypertension," *Hypertension* 35, 544-549 (2000)

- [67] Sacks FM, Svetkey LP, Vollmer WM, Appel LJ, Bray GA, Harsha D, Obarzanek E, Conlin PR, Miller ER III, Simons-Morton DG, Karanja N, Lin PH, DASH-Sodium Collaborative Research Group, "Effects on blood pressure of reduced dietary sodium and the Dietary Approaches to Stop Hypertension (DASH) diet," *N Engl J Med* 344, 3-10 (2001)
- [68] Vollmer WM, Sacks FM, Ard J, Appel LJ, Bray GA, Simons-Morton DG, Conlin PR, Svetkey LP, Erlinger TP, Moore TJ, Karanja N, "Effects of diet and sodium intake on blood pressure: subgroup analysis of the DASH-sodium trial," *Ann Intern Med* 135, 1019-1028 (2001)
- [69] Chobanian AV, Hill M, National Heart, Lung, and Blood Institute, "Workshop on sodium and blood pressure: a critical review of current scientific evidence," *Hypertension* 35, 858-863 (2000)
- [70] Kelley GA, Kelley KS, "Progressive resistance exercise and resting blood pressure: a meta-analysis of randomized controlled trials," *Hypertension* 35, 838-843 (2000)
- [71] Whelton SP, Chin A, Xin X, He J, "Effect of aerobic exercise on blood pressure: a meta-analysis of randomized, controlled trials," *Ann Intern Med* 136, 493-503 (2002)
- [72] Xin X, He J, Frontini MG, Ogden LG, Motsamai OI, Whelton PK, "Effects of alcohol reduction on blood pressure: a meta-analysis of randomized controlled trials," *Hypertension* 38, 1112-1117 (2001)
- [73] Executive summary of the Third Report of the National Cholesterol Education Program (NCEP) Expert Panel on Detection, Evaluation, and Treatment of High Blood Cholesterol in Adults (Adult Treatment Panel III), National Heart, Lung, and Blood Institute, Available at <http://www.nhlbi.nih.gov/guidelines/cholesterol/atp3xsum.pdf> (Accessed Jan 10, 2011)

- [74] 4S Group, "Randomised trial of cholesterol lowering in 4444 patients with coronary heart disease: the Scandinavian Simvastatin Survival Study (4S)," *Lancet* 344, 1383-1389 (1994)
- [75] Shepherd J, Cobbe SM, Ford I, Isles CG, Lorimer AR, MacFarlane PW, McKillop JH, Packard CJ, "Prevention of coronary heart disease with pravastatin in men with hypercholesterolemia. West of Scotland Coronary Prevention Study Group," *N Engl J Med* 333, 1301-1307 (1995)
- [76] Sacks FM, Pfeffer MA, Moye LA, Rouleau JL, Rutherford JD, Cole TG, Brown L, Warnica JW, Arnold JM, Wun CC, Davis BR, Braunwald E, "The effect of pravastatin on coronary events after myocardial infarction in patients with average cholesterol levels. Cholesterol and Recurrent Events Trial Investigators," *N Engl J Med* 335, 1001-1009 (1996)
- [77] Downs JR, Clearfield M, Weis S, Whitney E, Shapiro DR, Beere PA, Langendorfer A, Stein EA, Kruyer W, Gotto AM Jr, "Primary prevention of acute coronary events with lovastatin in men and women with average cholesterol levels: results of AFCAPS/TexCAPS: Air Force/Texas Coronary Atherosclerosis Prevention Study," *JAMA* 279, 1615-1622 (1998)
- [78] Atherosclerosis, National Heart, Lung, and Blood Institute, Available at [http://www.nhlbi.nih.gov/health/dci/Diseases/Atherosclerosis/Atherosclerosis\\_All.html](http://www.nhlbi.nih.gov/health/dci/Diseases/Atherosclerosis/Atherosclerosis_All.html) (Accessed Jan 10, 2011)
- [79] Ellis SG, Omoigui N, Bittl JA, Lincoff M, Wolfe MW, Howell G, Topol EJ, "Analysis and comparison of operator-specific outcomes in interventional cardiology: from a multicenter database of 4860 quality-controlled procedures," *Circulation* 93, 431-439 (1996)



- [80] Wolfe MW, Roubin GS, Schweiger M, Isner JM, Ferguson JJ, Cannon AD, Cleman M, Cabin H, Leya F, Bonan R, "Length of hospital stay and complications after percutaneous transluminal coronary angioplasty: clinical and procedural predictors," *Circulation* 92, 311-319 (1995)
- [81] Topol EJ, Leya F, Pinkerton CA, Whitlow PL, Hofling B, Simonton CA, Masden RR, Serruys PW, Leon MB, Williams DO, "A comparison of directional atherectomy with coronary angioplasty in patients with coronary artery disease," *N Engl J Med* 329, 221-227 (1993)
- [82] Adelman AG, Cohen EA, Kimball BP, Bonan R, Ricci DR, Webb JG, Laramie L, Barbeau G, Traboulsi M, Corbett BN, "A comparison of directional atherectomy with balloon angioplasty for lesions of the left anterior descending coronary artery," *N Engl J Med* 329, 228-233 (1993)
- [83] Nobuyoshi M, Kimura T, Nosaka H, Mioka S, Ueno K, Yokoi H, Hamasaki N, Horiuchi H, Ohishi H, "Restenosis after successful percutaneous transluminal coronary angioplasty: serial angiographic follow-up of 229 patients," *J Am Coll Cardiol* 12, 616-623 (1988)
- [84] Serruys PW, de Jaegere P, Kiemeneij F, Macaya C, Rutsch W, Heyndrickx G, Emanuelsson H, Marco J, Legrand V, Materne P, "A comparison of balloon-expandable-stent implantation with balloon angioplasty in patients with coronary artery disease," *N Engl J Med* 331, 489-495 (1994)
- [85] Fischman DL, Leon MB, Baim DS, Schatz RA, Savage MP, Penn I, Detre K, Veltri L, Ricci D, Nobuyoshi M, "A randomized comparison of coronary-stent placement and balloon angioplasty in the treatment of coronary artery disease," *N Engl J Med* 331, 496-501 (1994)

- [86] Nissen SE, "The vulnerable plaque "hypothesis"- promise, but little progress," *JACC: Cardiovascular Imaging* 2(4), 483-485 (2009)
- [87] Briley-Saebo KC, Mulder WJ, Mani V, Hyafil F, Amirbekian V, Aguinaldo JG, Fisher EA, Fayad ZA, "Magnetic resonance imaging of vulnerable atherosclerotic plaques: current imaging strategies and molecular imaging probes," *J Magn Reson Imaging* 26, 460–479 (2007)
- [88] Wu JC, Bengel FM, Gambhir SS, "Cardiovascular molecular imaging," *Radiology* 244, 337-355 (2007)
- [89] Jaffer FA, Libby P, Weissleder R, "Molecular imaging of cardiovascular disease," *Circulation* 116, 1052-1061 (2007)
- [90] Sosnovik DE, Nahrendorf M, Weissleder R, "Molecular magnetic resonance imaging in cardiovascular medicine," *Circulation* 115, 2076-2086 (2007)
- [91] Cai W, Chen X, "Nanoplatfoms for targeted molecular imaging in living subjects," *Small* 3, 1840-1854 (2007)
- [92] Caruthers SD, Wickline SA, Lanza GM, "Nanotechnological applications in medicine," *Curr Opin Biotechnol* 18(1), 26-30 (2007)
- [93] Trivedi RA, Mallawarachi C, U-King-Im JM, Graves MJ, Horsley J, Goddard MJ, Brown A, Wang L, Kirkpatrick PJ, Brown J, Gillard JH, "Identifying inflamed carotid plaques using in vivo USPIO-enhanced MR imaging to label plaque macrophages," *Arterioscler Thromb Vasc Biol* 26, 1601-1606 (2006)
- [94] Hyafil F, Cornily JC, Feig JE, Gordon R, Vucic E, Amirbekian V, Fisher EA, Fuster V, Feldman LJ, Fayad ZA, "Noninvasive detection of macrophages using a nanoparticulate contrast agent for computed tomography," *Nature Med* 13, 636-641 (2007)

- [95] Tawakol A, Migrino RQ, Bashian GG, Bedri S, Vermylen D, Cury RC, Yates D, LaMuraglia GM, Furie K, Houser S, Gewirtz H, Muller JE, Brady TJ, Fischman AJ, "In vivo  $^{18}\text{F}$ -fluorodeoxyglucose positron emission tomography imaging provides a noninvasive measure of carotid plaque inflammation in patients," *J Am Coll Cardiol* 48, 1818-1824 (2006)
- [96] Annovazzi A, Bonanno E, Arca M, D'Alessandria C, Marcoccia A, Spagnoli LG, Violi F, Scopinaro F, De Toma G, Signore A, " $^{99\text{m}}\text{Tc}$ -interleukin-2 scintigraphy for the in vivo imaging of vulnerable atherosclerotic plaques," *Eur J Nucl Med Mol Imaging* 33(2), 117-126 (2006)
- [97] Jaffer FA, Vinegoni C, John MC, Aikawa E, Gold HK, Finn AV, Ntziachristos V, Libby P, Weissleder R, "Real-time catheter molecular sensing of inflammation in proteolytically active atherosclerosis," *Circulation* 118(18), 1802-1809 (2008)
- [98] Wang B, Yantsen E, Larson T, Karpouk AB, Sethuraman S, Su JL, Sokolov K, Emelianov SY, "Plasmonic intravascular photoacoustic imaging for detection of macrophages in atherosclerotic plaques," *Nano Lett* 9(6), 2212-7 (2009)
- [99] Smith BR, Heverhagen J, Knopp M, Schmalbrock P, Shapiro J, Shiomi M, Moldovan NI, Ferrari M, Lee SC, "Localization to atherosclerotic plaque and biodistribution of biochemically derivatized superparamagnetic iron oxide nanoparticles (SPIONs) contrast particles for magnetic resonance imaging (MRI)," *Biomed Microdevices* 9(5), 719-727 (2007)
- [100] Kolodgie FD, Petrov A, Virmani R, Narula N, Verjans JW, Weber DK, Hartung D, Steinmetz N, Vanderheyden JL, Vannan MA, Gold HK, Reutelingsperger CP, Hofstra L, Narula J, "Targeting of apoptotic macrophages and experimental atheroma with radiolabeled annexin V: a technique with potential for noninvasive imaging of vulnerable plaque," *Circulation* 108(25), 3134-3139 (2003)

- [101] McAteer MA, Sibson NR, von Zur Muhlen C, Schneider JE, Lowe AS, Warrick N, Channon KM, Anthony DC, Choudhury RP, "In vivo magnetic resonance imaging of acute brain inflammation using microparticles of iron oxide," *Nat Med* 13(10), 1253-1258 (2007)
- [102] Broisat A, Riou LM, Ardisson V, Boturyn D, Dumy P, Fagret D, Ghezzi C, "Molecular imaging of vascular cell adhesion molecule-1 expression in experimental atherosclerotic plaques with radiolabelled B2702-p," *Eur J Nucl Med Mol Imaging* 34(6), 830-840 (2007)
- [103] Nahrendorf M, Jaffer FA, Kelly KA, Sosnovik DE, Aikawa E, Libby P, Weissleder R, "Noninvasive vascular cell adhesion molecule-1 imaging identifies inflammatory activation of cells in atherosclerosis," *Circulation* 114, 1504-1511 (2006)
- [104] Villanueva FS, Lu E, Bowry S, Kilic S, Tom E, Wang J, Gretton J, Pacella JJ, Wagner WR, "Myocardial ischemic memory imaging with molecular echocardiography," *Circulation* 115, 345-352 (2007)
- [105] Meding J, Urich M, Licha K, Reinhardt M, Misselwitz B, Fayad ZA, Weinmann HJ, "Magnetic resonance imaging of atherosclerosis by targeting extracellular matrix deposition with Gadofluorine M," *Contrast Media Mol Imaging* 2(3), 120-129 (2007)
- [106] Megens RT, Oude Egbrink MG, Cleutjens JP, Kuijpers MJ, Schiffrers PH, Merckx M, Slaaf DW, van Zandvoort MA, "Imaging collagen in intact viable healthy and atherosclerotic arteries using fluorescently labeled CNA35 and two-photon laser scanning microscopy," *Mol Imaging* 6(4), 247-260 (2007)
- [107] Frias JC, Williams KJ, Fisher EA, Fayad ZA, "Recombinant HDL-like nanoparticles: a specific contrast agent for MRI of atherosclerotic plaques," *J Am Chem Soc* 126(50), 16316-16317 (2004)

- [108] Riou LM, Broisat A, Dimastromatteo J, Pons G, Fagret D, Ghezzi, "Pre-clinical and clinical evaluation of nuclear tracers for the molecular imaging of vulnerable atherosclerosis: an overview," *Curr Med Chem* 16(12), 1499-1511 (2009)
- [109] Winter PM, Neubauer AM, Caruthers SD, Harris TD, Robertson JD, Williams TA, Schmieder AH, Hu G, Allen JS, Lacy EK, Zhang H, Wickline SA, Lanza GM, "Endothelial  $\alpha\beta_3$  integrin-targeted fumagillin nanoparticles inhibit angiogenesis in atherosclerosis," *Arterioscler Thromb Vasc Biol* 26, 2103-2109 (2006)
- [110] Backer MV, Levashova Z, Patel V, Jehning BT, Claffey K, Blankenberg FG, Backer JM, "Molecular imaging of VEGF receptors in angiogenic vasculature with single-chain VEGF-based probes," *Nat Med* 13(4), 504-509 (2007)
- [111] Botnar RM, Perez AS, Witte S, Wiethoff AJ, Laredo J, Hamilton J, Quist W, Parsons EC Jr, Vaidya A, Kolodziej A, Barrett JA, Graham PB, Weisskoff RM, Manning WJ, Johnstone MT, "In vivo molecular imaging of acute and subacute thrombosis using a fibrin-binding magnetic resonance imaging contrast agent," *Circulation* 109(16), 2023-2029 (2004)
- [112] Taillefer R, Edell S, Innes G, Lister-James J, " Acute thromboscintigraphy with  $(^{99m}\text{Tc})$ -apcitide: results of the phase 3 multicenter clinical trial comparing  $^{99m}\text{Tc}$ -apcitide scintigraphy with contrast venography for imaging acute DVT. Multicenter Trial Investigators," *J Nucl Med* 41, 1214-1223 (2000)
- [113] Flaumenhaft R, Tanaka E, Graham GJ, De Grand AM, Laurence RG, Hoshino K, Hajjar RJ, Frangioni JV, "Localization and quantification of platelet-rich thrombi in large blood vessels with near-infrared fluorescence imaging," *Circulation* 115, 84-93 (2007)

- [114]Alonso A, Della Martina A, Stroick M, Fatar M, Griebe M, Pochon S, Schneider M, Hennerici M, Allémann E, Meairs S, "Molecular imaging of human thrombus with novel abciximab immunobubbles and ultrasound," *Stroke* 38(5), 1508-1514 (2007)
- [115]Ma LL, Feldman MD, Tam JM, Paranjape AS, Cheruku KK, Larson TA, Tam JO, Ingram DR, Paramita V, Villard JW, Jenkins JT, Wang T, Clarke GD, Asmis R, Sokolov K, Chandrasekar B, Milner TE, Johnston KP, "Small multifunctional nanoclusters (nanoroses) for targeted cellular imaging and therapy," *ACS Nano* 3(9), 2686-2696 (2009)

## Chapter 3 Optical Properties of Nanorose<sup>1</sup>

### 3.1 ABSTRACT

Nanorose is used to target macrophages in atherosclerotic plaques. Experimental measurement and simulation of nanorose absorption ( $\sigma_a$ ) and scattering ( $\sigma_s$ ) cross-sections give, respectively,  $\sigma_a = (3.1 \pm 0.5) \times 10^{-14} \text{ m}^2$  and  $\sigma_a/\sigma_s = 10.5$ .

### 3.2 INTRODUCTION

Atherosclerosis and specifically rupture of vulnerable plaques leading to myocardial infarction and stroke remain the leading cause of death worldwide [1]. In atherosclerosis, macrophages can infiltrate plaques which are often associated with lipid deposits. Nanorose (taken up by macrophages via endocytosis) is a spectrally-tunable optical nanoaggregate, which has an average diameter of 30 nm and consists of thin gold shell coated iron oxide nanoparticles [2]. Intense NIR (700-850 nm) absorbance makes nanorose a candidate marker for targeting macrophages in atherosclerotic plaques using imaging techniques based on photo-absorption [3]. A direct optical properties measurement technique can be used to measure  $\sigma_a$  and  $\sigma_s$  of nanorose solution [4]. In comparison, the discrete-dipole-approximation (DDA) [5] can be utilized to simulate light interaction with a single nanorose cluster and calculate  $\sigma_a$  and  $\sigma_s$  of a nanorose. The purpose of this study is to experimentally measure  $\sigma_a$  and  $\sigma_s$  of nanorose and compare with results from DDA simulation.

---

<sup>1</sup> Significant portions of this chapter has been previously published in *ACS Nano* 3(9), 2686–2696 (2009) and *OSA Technical Digest*, JWA12 (2010).

### 3.3 MATERIALS AND METHODS

#### 3.3.1 Direct Measurement

A lens coupled fiber optic laser (Opto Power, Inc.; Model FCTS/B) was used to irradiate a nanorose sample solution positioned inside an integrating sphere (Figure 3.1). The nanorose sample solution was positioned in a glass sample holder and consisted to two microscope slides displaced by 80  $\mu\text{m}$ . The sample holder was positioned in the center of the integrating sphere and oriented perpendicular to the incident laser beam (3W, 800nm, CW mode). A power meter (Newport, Inc.; Model 1935-C) was placed at a port of the integrating sphere oriented perpendicular to the laser beam. For absorption coefficient ( $\mu_a$ ) measurement, radiant power was measured with the sample holder containing deionized water and nanorose solution. The directly transmitted beam through the sample holder was contained within the integrating sphere and contributed to the measurement. For scattering coefficient ( $\mu_s$ ) measurement, the same procedure was followed except that the non-scattered directly transmitted beam was allowed to exit the integrating sphere and did not contribute to the measurement. Samples were prepared at six nanorose concentrations (385, 193, 96, 77, 39 and 26  $\mu\text{g Au/ml}$ ) with corresponding nanorose number densities  $N = 1.2 \times 10^{11}$ ,  $0.6 \times 10^{11}$ ,  $0.4 \times 10^{11}$ ,  $0.24 \times 10^{11}$ ,  $0.12 \times 10^{11}$  and  $0.08 \times 10^{11}$  nanoroses/ml, respectively. Absorption coefficient and scattering coefficient were computed using equations  $\mu_a = (1/l) \cdot (I_{a0} - I_a) / I_{a0}$  and  $\mu_s = (1/l) \cdot (I_s / I_{s0})$ . Where  $l = 80 \mu\text{m}$  is nanorose solution sample thickness;  $I_0$  (W) and  $I$  (W) represent, respectively, the measured radiant power with deionized water and nanorose solution. Subscripts  $a$  and  $s$  represent absorption and scattering coefficient measurements. Absorption and scattering cross-sections were then computed by equations  $\sigma_a = \mu_a / N$  and  $\sigma_s = \mu_s / N$ .



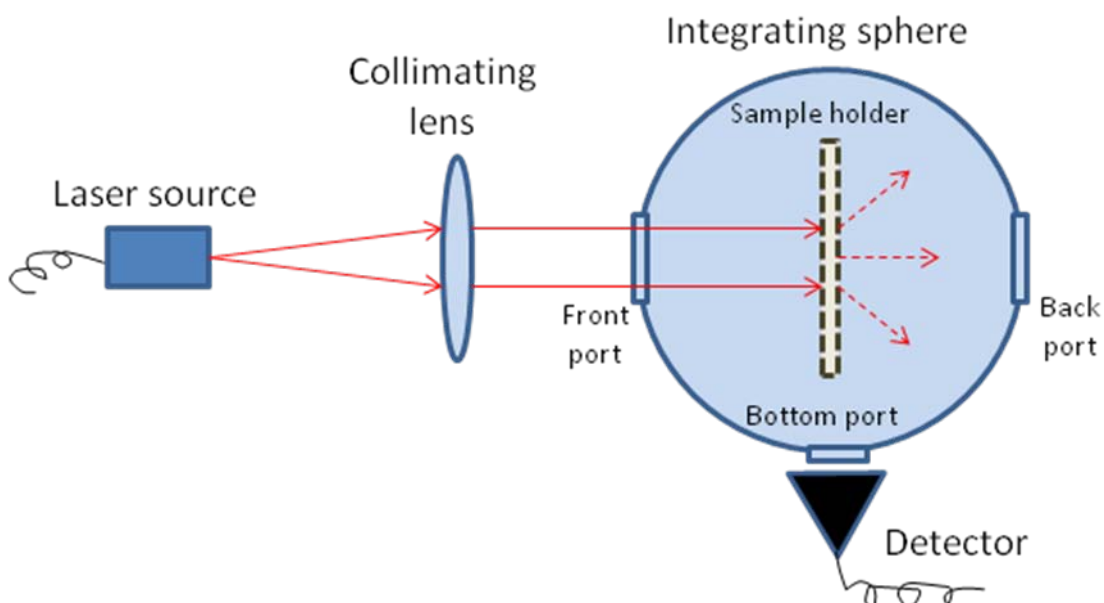


Figure 3.1. Experimental setup for absorption and scattering cross-sections measurement.

### 3.3.2 Discrete Dipole Approximation

Dipole array representation for a nanorose cluster geometry (30 nm in diameter, 60 gold-coated iron oxide nanoparticles) was created (Figure 3.2) and loaded into a DDA program (DDSCAT 7.0) and absorption and scattering cross-sections were calculated.

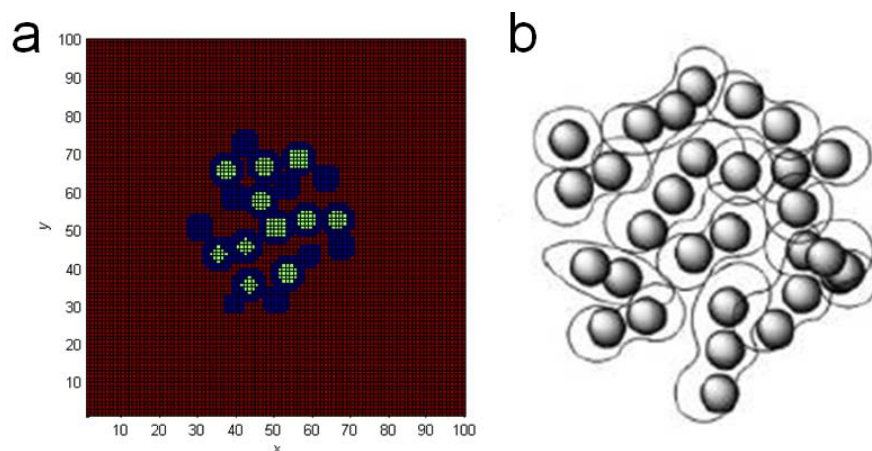


Figure 3.2. (a) A cross-section image of nanorose geometry used in DDA. (b) Cartoon of hypothetical nanorose geometry depicted from nanorose TEM image.

### 3.4 RESULTS AND DISCUSSION

From experimental measurements, the absorption coefficient  $\mu_a = 29.3, 19.2, 10.3, 7.6, 4.2$  and  $2.9 \text{ cm}^{-1}$ , the corresponding absorption cross-section  $\sigma_a = 2.4 \times 10^{-14}, 3.2 \times 10^{-14}, 2.6 \times 10^{-14}, 3.2 \times 10^{-14}, 3.5 \times 10^{-14}$  and  $3.6 \times 10^{-14} \text{ m}^2$  (mean =  $3.1 \times 10^{-14} \text{ m}^2$ , standard deviation =  $0.5 \times 10^{-14} \text{ m}^2$ ) were computed from the six nanorose concentrations. Because the values of  $(I_s / I_{s0}) / e^{-\mu_a x}$  for the six nanorose concentrations are close to 1 (mean = 0.98, standard deviation = 0.03), data suggest that  $\sigma_s$  is much smaller than  $\sigma_a$  and beyond the sensitivity of our measurements. DDA simulation results show that  $\sigma_a / \sigma_s = 10.5$  for a randomly generated nanorose cluster geometry (30 nm in diameter, 60 gold-coated iron oxide nanoparticles). The ratio of absorption to scattering cross-sections ( $\sigma_a / \sigma_s$ ) from DDA simulation is consistent with our experimental results.

DDA simulation gives smaller absorption cross-section than that determined from experiment, which suggests that actual nanorose structure may be different from the randomly generated nanorose cluster geometry in DDA. In fact, nanorose has a much more complicated shape and composition (Figure 3.2b). This complexity needs to be taken into account in further DDA simulations. For instance, some of the gold shell coated nanoparticles in nanorose are so closely arranged that those nanoparticles can take on a “nanorod-like” shape and be oriented side-by-side to neighboring nanoparticles. As a result, actual absorption and scattering cross-sections may be larger than computed values due to the plasmon coupling effect [6].

### 3.5 CONCLUSION

The absorption and scattering cross-sections of nanorose are determined from a direct optical properties measurement and a DDA simulation. Experiment indicates that absorption cross-section is  $\sigma_a = (3.1 \pm 0.5) \times 10^{-14} \text{ m}^2$ . DDA results indicate that nanorose absorption cross-section is an order of magnitude larger than the scattering cross-section.

### 3.6 REFERENCES

- [1] Yusuf S, Reddy S, Ounpuu S, Anand S, “Global burden of cardiovascular diseases: part I: general considerations, the epidemiologic transition, risk factors, and impact of urbanization,” *Circulation* 104, 2746-2753 (2001)
- [2] Ma LL, Feldman MD, Tam JM, Paranjape AS, Cheruku KK, Larson TA, Tam JO, Ingram DR, Paramita V, Villard JW, Jenkins JT, Wang T, Clarke GD, Asmis R, Sokolov K, Chandrasekar B, Milner TE, Johnston KP, “Small multifunctional nanoclusters (nanoroses) for targeted cellular imaging and therapy,” *ACS Nano* 3(9), 2686-2696 (2009)
- [3] Wang T, Qiu J, Ma LL, Li X, Sun J, Ryoo S, Johnston KP, Feldman MD, Milner TE, “Nanorose and lipid detection in atherosclerotic plaque using dual-wavelength PTW imaging,” *Proc. SPIE*, Vol. 7562, 75620S (2010)
- [4] Patterson MS, Wilson BC, Wyman DR, “The propagation of optical radiation in tissue. II: optical properties of tissues and resulting fluence distributions,” *Lasers Med Sci* 6(4), 379-390(1991)
- [5] Draine BT, Flatau PJ, “User guide for the discrete dipole approximation code DDSCAT 7.0 (2008),” Available at <http://arxiv.org/abs/0809.0337>
- [6] Jain PK, Eustis S, El-Sayed MA, “Plasmon coupling in nanorod assemblies: optical absorption, discrete dipole approximation simulation, and exciton-coupling model,” *J Phys Chem B* 110, 18243-18253 (2006)

## Chapter 4 Photothermal Wave (PTW) Imaging of Nanorose and Lipid<sup>2</sup>

### 4.1 FIXED-FREQUENCY PTW IMAGING OF MACROPHAGES AND LIPID DEPOSITS IN EX VIVO TISSUES

#### 4.1.1 Abstract

Atherosclerosis and specifically rupture of vulnerable plaques account for 23% of all deaths worldwide, far surpassing both infectious diseases and cancer. In atherosclerosis, macrophages can infiltrate plaques which are often associated with lipid deposits. PTW imaging is based on the periodic thermal modulation of a sample using intensity modulated light. Intensity modulated light enters the sample and is absorbed by targeted chromophores and generates a periodic thermal modulation. We report use of PTW imaging to visualize nanoroses (taken up by macrophages via endocytosis) and lipids in atherosclerotic plaques. Two excitation wavelengths were selected to image nanoroses (800 nm) and lipids (1210 nm). Atherosclerotic plaque in a rabbit abdominal artery was irradiated (800 nm and 1210 nm separately) at a frequency of 4 Hz to generate PTWs. The radiometric temperature at the tissue surface was recorded by an infrared (IR) camera over a 10 second time period at the frame rate of 25.6 Hz. Extraction of images ( $256 \times 256$  pixels) at various frequencies was performed by Fourier transform at each pixel. Frequency amplitude images were obtained corresponding to 800 nm and 1210 nm laser irradiation. Computed images suggest that the distributions of both nanorose and lipid can be identified in amplitude images at a frequency of 4 Hz. Nanoroses taken up by macrophages are distributed at the edges of lipid deposits. Observation of high concentration of nanoroses in atherosclerotic plaque confirms that nanoroses are present at locations associated with lipid deposits.

---

<sup>2</sup> Significant portions of this chapter has been previously published in *Proc SPIE* 7562, 75620S1-75620S7 (2010), *Proc BMES*, OP-7-3-3A (2010), and *Lasers Surg Med* 42 (S22), 13 (2010).

#### 4.1.2 Introduction

Atherosclerosis and specifically rupture of vulnerable plaques leading to myocardial infarction, stroke and progression of peripheral artery disease remain the leading cause of death worldwide [1]. Vulnerable plaques are characterized as having a thin fibrous cap of less than 65  $\mu\text{m}$ , increased infiltration of macrophages with decreased smooth muscle cells, and an increased lipid core size when compared to stable plaques [2]. Davies and coworkers noted that with the reconstruction of serial histological sections in patients with acute myocardial infarctions associated with death, a rupture or fissuring of vulnerable plaque was evident [3]. Further, greater macrophage density is associated with increased plaque vulnerability to rupture [4]. Thus, macrophages are an important early cellular marker that indicate and contribute to increased risk of plaque remodeling and subsequent rupture in the coronary, cerebral, and peripheral circulations. Nanorose used to target macrophages in this study is a spectrally-tunable optical nanoaggregates. The 30 nm diameter nanoroses are formed by kinetically controlled assembly of thin gold shell coated iron oxide nanoparticles in aqueous medium [5]. Intense NIR (700-850 nm) absorbance with an absorption cross-section of  $3.1 \times 10^{-14} \text{ m}^2$  at a wavelength of 800 nm is achieved by the asymmetric core-shell geometry and collective effects from close spacing between primary particles in the clusters. Due to dextran coating, nanorose can be taken up by macrophages via endocytosis [6]. Therefore, macrophages are selectively targeted by nanorose. Since the absorbance spectrum of lipid and normal aortic tissue are known to nadir at 700-800 nm [7] while nanorose has an absorption peak at 800 nm; Moreover, the absorption of water is relatively small compared to lipid at 1210 nm [8], lasers at wavelengths of 800 nm and 1210 nm are chosen to visualize nanorose and lipid respectively. PTW imaging is based on the periodic thermal modulation of a sample using intensity modulated light. Intensity

modulated light enters the sample and is absorbed by targeted chromophores and generates a periodic thermal modulation [9]. In this study, we propose using PTW imaging to visualize nanoroses and lipids in atherosclerotic plaques.

### 4.1.3 Materials and Methods

#### 4.1.3.1 Preparation of Tissues

A double-balloon injury procedure was performed at the bifurcation of the common iliacs on a New Zealand white rabbit. The rabbit was fed with high fat diet for two weeks after balloon injuries for the sake of atherosclerosis growth. The rabbit was then sacrificed three days after marginal ear vein injection with nanorose (1.4 mg nanorose/kg rabbit body weight). The aorta was harvested and flushed until there were no red blood cells. Then the aorta was placed in a specimen container with saline. The abdominal artery, which was 1 cm below diaphragm and 1 cm above bifurcation, was cut off because the double-balloon may not injure those segments. In the remaining abdominal artery, three segments (1.5 cm in length for each segment) were equally harvested and marked A1, A2 and A3 (Figure 4.1). All the procedure was performed using sterile equipment, supplies and aseptic technique. The animal protocol was approved by IACUC at the University of Texas Health Science Center at San Antonio.

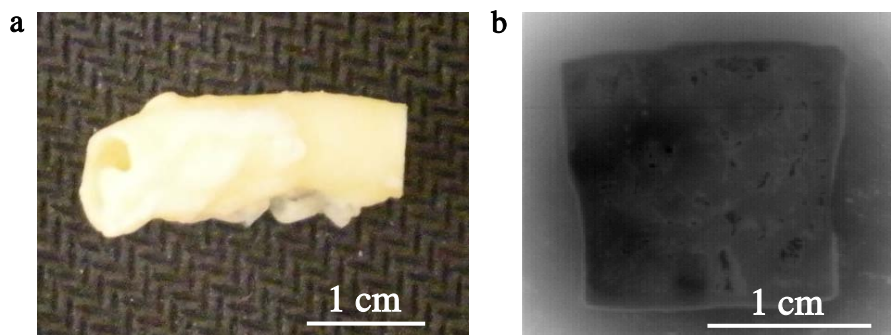


Figure 4.1. (a) Digital image of a piece of abdominal artery. (b) Top view infrared image of a segment on an abdominal artery before laser irradiation (surface in the image is intimal layer of the artery).

#### 4.1.3.2 PTW Theory and System

PTW imaging has played an important role in the area of non-invasive evaluation of subsurface structures in tissue and tissue phantom studies. It is achieved by observing, recording, and analyzing the thermal response at the material surface to a heat stimulus.

In this study, the one dimensional Green's function in frequency domain for a semi-infinite solid with a plane heat source at the position  $x = x_0$  is given as follows [10]:

$$G(x - x_0 | x + x_0, \omega) = \frac{1-i}{2\sqrt{2\alpha\omega}} (e^{-q(\omega)|x-x_0|} + e^{-q(\omega)(x+x_0)}) \quad (4.1)$$

Where the use of “+” signifies that the function satisfies the homogeneous Neumann boundary condition at the irradiated sample surface  $x = 0$ , which is:

$$\nabla G(x, \omega) \Big|_{x=0} = 0 \quad (4.2)$$

The solution for the temperature  $T(x, \omega)$  as a function of depth ( $x$ ) and angular modulation frequency ( $\omega$ ) is then given by [11]:

$$T(x, \omega) = \int_{x_0=0}^{\infty} G(x - x_0 | x + x_0, \omega) Q(x_0, \omega) dx_0 \quad (4.3)$$

Where  $Q(x_0, \omega)$  is the spectral component of the laser-induced volumetric heat source.

In Eq. (4.1),  $q(\omega)$  is a PTW vector defined by:

$$q(\omega) = (1+i)\sqrt{\frac{\omega}{2\alpha}} = (1+i)\sqrt{\frac{\pi f}{\alpha}} \quad (4.4)$$

Where  $\alpha = 0.127 \text{ mm}^2/\text{s}$  is the thermal diffusivity of aortic tissue and  $f$  is modulation frequency. From Eq. (4.4), a thermal diffusion length ( $\mu$ ), which is a measure of depth probed by the PTWs within the sample, can be written as follows:

$$\mu = \sqrt{\frac{\alpha}{\pi f}} \quad (4.5)$$

Because most of the nanoroses (taken up by macrophages) in atherosclerotic plaque are distributed within the intimal layer of artery in rabbit [12], which is several

hundred micrometers from the internal arterial wall [13], the modulation frequency  $f = 4$  Hz is calculated by Eq. (4.5) and used in this study.

Figure 4.2 shows a schematic of the measurement setup used in this study. Two lens coupled fiber optic lasers (Opto Power, Inc., Model FCTS/B; Candela, Model 1200-001) at the wavelengths of 800 nm and 1210 nm respectively with maximum output powers of 5 W were used to irradiate aortic tissues in order to derive information on reflected PTW magnitude signals. A 50 mm diameter lens ( $f = 40$  cm) was used to focus the collimated laser beam onto a 1.5 cm diameter laser spot on the tissue surface. A digital shutter controlled by a function generator (not shown in Figure 4.2) shuttered continuous laser light into a frequency of 4 Hz with 50% laser cycle. The IR signal (radiometric temperature) from the tissue surface was reflected by a dichroic and then recorded by an infrared camera (FLIR Thermal Infrared Camera Systems, Inc.; Model: ThermoVision SC6000 with an InSb detector (3.0-5.0  $\mu\text{m}$ )). The shutter and thermal camera were synchronized by a photodiode connected with a function generator (not shown in Figure 4.2). The extraction of various frequency components present was performed by Fourier transform on each pixel of the thermal image sequence.



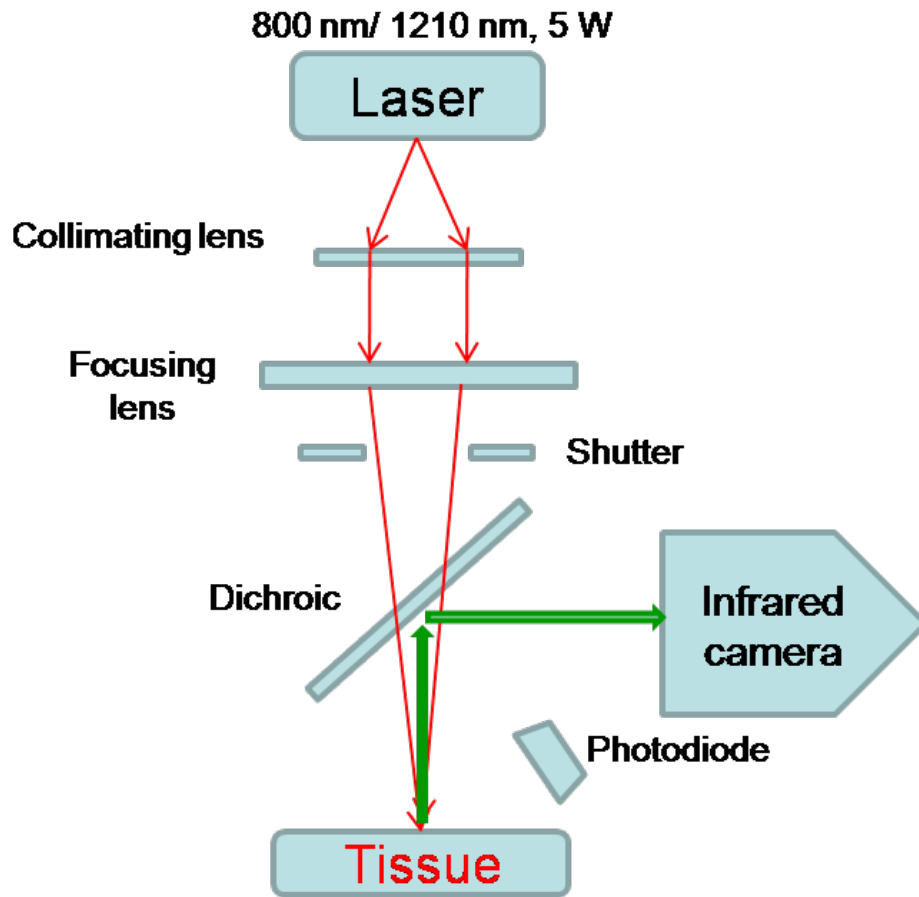


Figure 4.2. Schematic diagram of PTW imaging instrumentation to measure the IR signal of the aortic tissue in response to periodic laser irradiation (800 nm and 1210 nm respectively).

#### 4.1.4 Results

An abdominal artery segment with atherosclerotic plaque was irradiated by 800 nm and 1210 nm lasers respectively at a frequency of 4 Hz to generate PTWs. The radiometric temperature at the tissue surface was recorded by the IR camera over a 10 second time period at the frame rate of 25.6 Hz. Extraction of images ( $256 \times 256$  pixels) at various frequencies was performed by Fourier transform at each pixel. Frequency amplitude images were obtained corresponding to 800 nm and 1210 nm laser irradiation (Figure 4.3) respectively. Computed images suggest that the distributions of nanorose can

be identified in amplitude images at 800 nm (Figure 4.3a) and, shapes of plaque lesions and fatty streaks (lipid deposits) are shown at 1210 nm (Figure 4.3b).

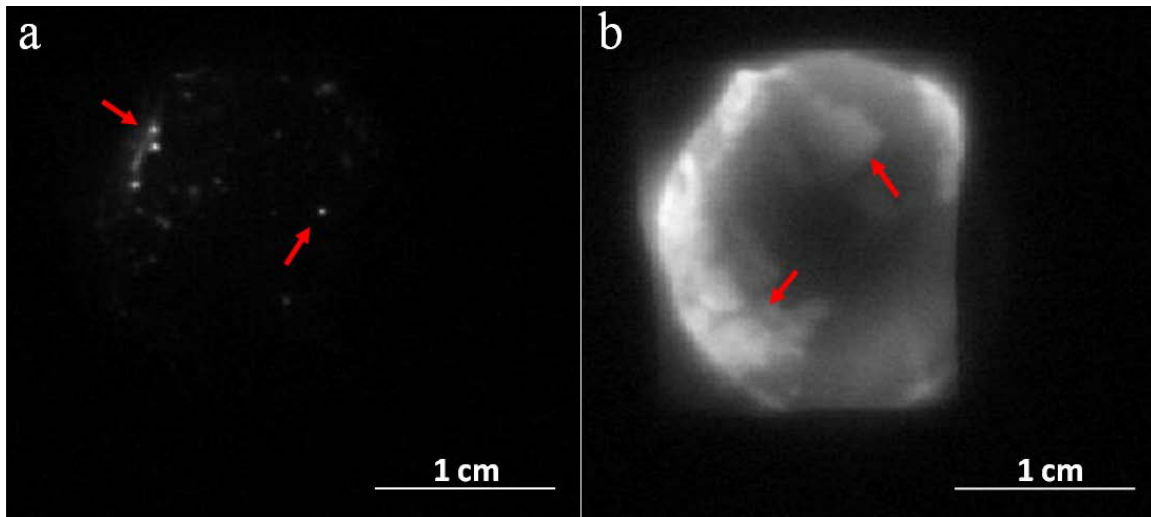


Figure 4.3. (a) Amplitude image at 800 nm laser irradiation (arrows point to the positions of nanoroses). (b) Amplitude image at 1210 nm laser irradiation (arrows point to the positions of lipid deposits).

Overlay of 800 nm and 1210 nm amplitude images shows the relative distribution of nanorose and lipids (Figure 4.4a). Red spots in Figure 4.4a show the locations of nanorose taken up by macrophages. Dense accumulation of nanorose in a lipid deposit region is identified. Nanorose locations correspond to the edges of lipid deposits. However, nanorose is not localized at all lipid boundaries (Figure 4.4a) but located at some “specialized” locations such as 3C, 4C, 5C, 2D, 5D, 8F, 2G and 5G regions in Figure 4.4a. The region of 3C in the frequency amplitude image at 800 nm laser irradiation (Figure 4.3a) shows dense accumulation of nanoroses, which is consistent with the histology image of the same region (dense accumulation of macrophages is identified).

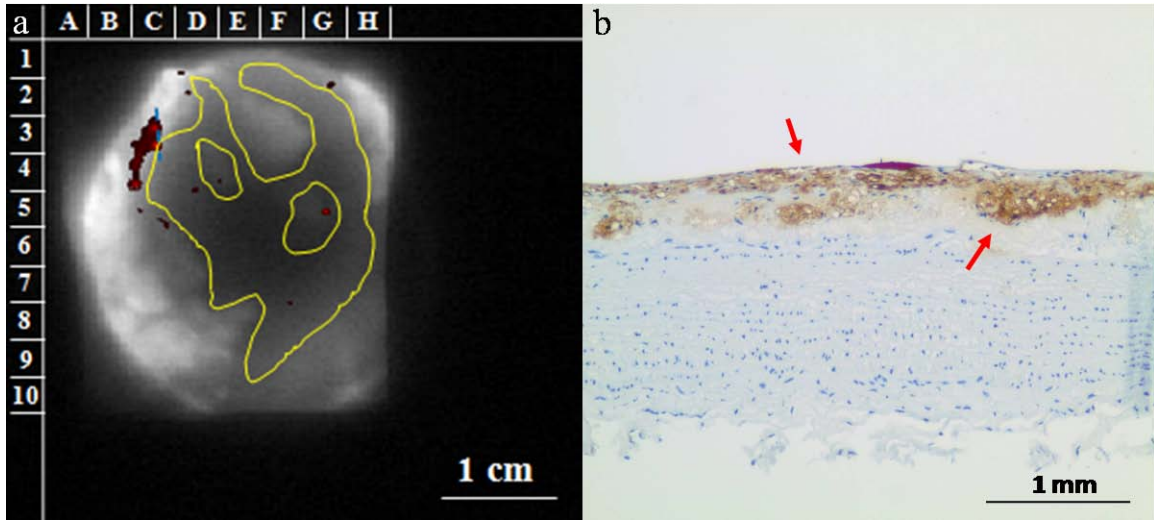


Figure 4.4. (a) Overlay of 800 nm and 1210 nm amplitude images (red color indicates nanorose, yellow line indicates the edges of lipid deposits). (b) Histology image of RAM-11 stain along the blue line at the region of 3C in (a). Brown color indicates macrophages (arrows point to accumulation positions of macrophages).

#### 4.1.5 Discussion

In PTW imaging a common technique to generate thermal waves is through absorption of sinusoidal incident intensity modulated light. Unlike the case of sinusoidal intensity modulated heating of the sample, a square wave intensity modulated light is used in this study. The advantages of square wave signal over the conventional sinusoidal signal can be explained by comparing their spectra. While a simple sine wave has only one spectral component at a frequency  $f(= \omega / 2\pi)$ , a square wave can be represented by its infinite Fourier series,

$$Q_{square}(t) = \frac{4}{\pi} \sum_{b=0}^{\infty} \frac{1}{2b+1} \sin(2b+1)\omega t \quad (4.6)$$

Computing mean square values of sine and square waves, clear that the energy of a square wave is two times higher than the energy of the sine wave of the same amplitude. In a square wave the additional energy is due to higher harmonics. More energy is injected comparably at the fundamental frequency  $b = 0$  in Eq. (4.6), which has

an amplitude  $1.273 (=4/\pi)$  times higher than the sine signal, leading to increased amplitude of reflected signal.

Based on the theory that macrophages are often distributed at sites of plaque lesions [14], it is expected that macrophages are located at all edges of lipid deposits of the plaque. However, no nanorose is detected at regions such as 4G, 8E and 10F, etc. Possible reasons are: (1) Blood flow may influence the distribution of nanorose around macrophages. In other words, some macrophages at edgesproprop of lipid deposits may not take up nanorose because of local blood flow variation. (2) PTW imaging at 800 nm may not show the presence of some nanorose. Because the thermal diffusion length ( $\mu$ ) in this study is 100  $\mu\text{m}$  in depth (corresponding to the modulation frequency of 4 Hz), if nanorose is located deeper than 100  $\mu\text{m}$ , it is possible that IR camera may not detect the radiometric temperature increase at tissue surface due to thermal diffusion. (3) Not all macrophages take up nanorose. Nanorose is taken up by macrophages through endocytosis. However, if macrophages are not in an “activated” state, which is characterized by increased endocytic and phagocytic capacity, anti-inflammatory properties and the ability to remodel extracellular matrix [15], endocytosis of nanorose may not proceed.

#### **4.1.6 Conclusion**

Frequency amplitude images corresponding to 800 nm and 1210 nm laser irradiation suggest that the distributions of both nanorose and lipid can be identified by PTW imaging at a frequency of 4 Hz. Nanoroses taken up by macrophages are distributed at the edges of lipid deposits. Observation of high concentration of nanoroses in atherosclerotic plaque confirms that nanoroses are present at locations associated with lipid deposits.

#### 4.1.7 Acknowledgements

The author thanks Marc D. Feldman, MD and Xiankai Li for the preparation of rabbit tissues. The author also thanks Keith P. Johnston, Ph.D and Li Leo Ma for the supply of nanorose in this study.

#### 4.1.8 References

- [1] Yusuf S, Reddy S, Ounpuu S, Anand S, “Global burden of cardiovascular diseases: part I: general considerations, the epidemiologic transition, risk factors, and impact of urbanization,” *Circulation* 104, 2746-2753 (2001)
- [2] Davies MJ, Richardson PD, Woolf N, Katz DR, Mann J, “Risk of thrombosis in human atherosclerotic plaques: role of extracellular lipid, macrophage, and smooth muscle cell content,” *Br Heart J* 69, 377-381 (1993)
- [3] Davies MJ, ThomasA, “Thrombosis and acute coronary-artery lesions in sudden cardiac ischemic death,” *N Engl J Med* 310, 1137-1140 (1984)
- [4] Kolodgie FD, Virmani R, Burke AP, Farb A, Weber DK, Kutys R, Finn AV, Gold HK, “Pathologic assessment of the vulnerable human coronary plaque,” *Heart* 90, 1385-1391 (2004)
- [5] Ma LL, Feldman MD, Tam JM, Paranjape AS, Cheruku KK, Larson TA, Tam JO, Ingram DR, Paramita V, Villard JW, Jenkins JT, Wang T, Clarke GD, Asmis R, Sokolov K, Chandrasekar B, Milner TE, Johnston KP, “Small multifunctional nanoclusters (nanoroses) for targeted cellular imaging and therapy,” *ACS Nano* 3(9), 2686-2696 (2009)
- [6] Mornet S, Vasseur S, Grasset F, Duguet E, “Magnetic nanoparticle design for

- medical diagnosis and therapy,” *J Mat Chem* 14, 2161-2175 (2004)
- [7] Jacques S, Optical properties spectra, Available at: <http://omlc.ogi.edu/spectra>
- [8] Anderson RR, Farinelli W, Laubach H, Manstein D, Yaroslavsky AN, Gubeli III J, Jordan K, Neil GR, Shinn M, Chandler W, Williams GP, Benson SV, Douglas DR, Dylla HF, “Selective photothermolysis of lipid-rich tissues: A free electron laser study,” *Lasers Surg Med* 38(10), 913-919 (2006)
- [9] Mulaveesala R, Tuli S, “Theory of frequency modulated thermal wave imaging for nondestructive subsurface defect detection,” *Appl Phys Lett* 89, 191-193 (2006)
- [10] Mandelis A, “Green’s functions in thermal-wave physics: Cartesian coordinate representations,” *J Appl Phys* 78(2), 647-655 (1995)
- [11] Welch AJ, van Gemert MJC, "Optical-Thermal Response of Laser-Irradiated Tissue," New York: Plenum Press, 386-390 (1995)
- [12] Cotran RS, Kumar V, Collins T, Robbins SL, "Robbins pathologic basis of disease," Saunders, The University of Michigan, 523-524 (1999)
- [13] Yoshimura K, Esato K, Fujioka K, “Effects of nilvadipine, a calcium antagonist, on intimal thickness of vascular grafting in cholesterol-fed rabbits,” *Int J Angiology* 5(1), 8-14 (1996)
- [14] ten Have AG, Gijzen FJH, Wentzel JJ, Slager CJ, van der Steen AFW, “Temperature distribution in atherosclerotic coronary arteries: influence of plaque geometry and flow (a numerical study),” *Phys Med Biol* 49, 4447-4462 (2004)
- [15] Kzhyshkowska J, Krusell L, “Cross-talk between endocytic clearance and secretion in macrophages,” *Immunobiology* 214(7), 576-593 (2009)

## 4.2 MULTI-FREQUENCY PTW IMAGING OF LIPID DEPOSITS IN EX VIVO TISSUES

### 4.2.1 Summary

Atherosclerosis in combination with rupture of vulnerable plaques is the leading cause of deaths worldwide, surpassing both infectious diseases and cancer. Atherosclerotic plaques are characterized by a thin fibrous cap and a thrombogenic lipid core. PTW imaging is based on the periodic thermal modulation of a sample using intensity modulated light that is absorbed by target chromophores (lipid in this study) generating a periodic thermal modulation. We report use of PTW imaging to visualize three-dimensional distribution of lipid in atherosclerotic plaque in *ex vivo* atherosclerotic tissues taken from a rabbit model of atherosclerosis. The 1210 nm excitation wavelength was selected to target lipid. The atherosclerotic plaque sample was irradiated at modulation frequencies ranging from 0.1 to 5 Hz to generate PTWs. The radiometric temperature at the sample surface was recorded by an infrared (IR) camera over a 20 second time period at the frame rate of 25.6 Hz. Amplitude and phase images (256×256 pixels) at selected frequencies were obtained by computing a fast Fourier transform of the time-dependent radiometric emission at each pixel. Amplitude and phase images obtained at each modulation frequency were related to lateral and depth distribution of lipid in the atherosclerotic tissue samples. PTW images recorded from the atherosclerotic plaque suggest that lateral and depth distribution of lipid can be identified by analysis of amplitude and phase images at selected modulation frequencies. The geometric shape of atherosclerotic plaque is associated with distribution of the lipid deposits.

### 4.2.2 Description of Design Objective

Atherosclerosis and specifically rupture of vulnerable plaques leading to myocardial infarction, stroke and progression of peripheral artery disease remain the

leading cause of death worldwide [1]. Vulnerable plaques are characterized as having a thin fibrous cap of less than 65  $\mu\text{m}$ , increased infiltration of macrophages with decreased smooth muscle cells, and an increased lipid core size when compared to stable plaques [2]. PTW imaging is based on the periodic thermal modulation of a sample using intensity modulated light. Intensity modulated light enters the sample and is absorbed by targeted chromophores and generates a periodic thermal modulation [3]. The objective of this study is to use PTW imaging to visualize the lateral and depth distribution of lipid deposits in atherosclerotic plaques in a rabbit animal model of atherosclerosis. Moreover, the relationship between distribution of lipid deposits and shape of atherosclerotic plaque is discussed.

#### **4.2.3 Analysis and Performance Evaluation**

A double-balloon injury procedure was performed at the bifurcation of the common iliacs on a New Zealand white rabbit. The rabbit was fed with a high fat diet for two weeks after balloon injury to induce growth of atherosclerotic lesions. The rabbit was then sacrificed, and aorta (Figure 4.5a, b) was harvested and cut into  $8 \times 8 \text{ mm}^2$  tissue segments for PTW imaging.

Figure 1c shows a schematic of the measurement setup used in this study. A lens coupled fiber optic diode laser (Candela, Model 1200-001) at the wavelength of 1210 nm with maximum output power of 5 W was used to irradiate aortic tissues. A 50 mm diameter lens ( $f = 40 \text{ cm}$ ) was used to focus the collimated laser beam onto a 1 cm diameter laser spot on the tissue surface. A mechanical shutter controlled by a function generator (not shown in Figure 4.5c) shuttered continuous laser light into different modulation frequencies ranging from 0.1 to 5 Hz. Infrared radiation from the tissue surface was reflected by a dichroic and then recorded by an infrared camera (FLIR



Thermal Infrared Camera Systems, Inc.; Model: ThermoVision SC6000 with an InSb detector (3.0-5.0  $\mu\text{m}$ )).

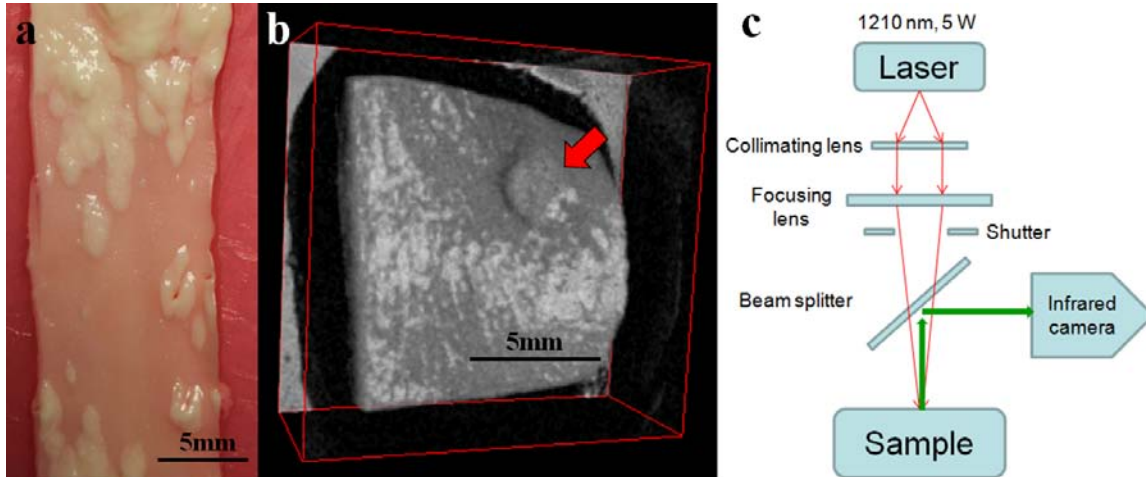


Figure 4.5. (a) Sample of atherosclerotic aorta of a Zealand white rabbit. (b) Reconstructed OCT image of the same atherosclerotic tissue in Figure 2. Arrow points to the plaque. (c) Schematic diagram of PTW imaging instrumentation to measure the IR signal of the aortic tissue in response to frequency modulated laser irradiation.

The radiometric temperature at the tissue surface was recorded by the IR camera over a 20 second time period at the frame rate of 25.6 Hz. Extraction of images (256  $\times$  256 pixels) at various frequencies was performed by fast Fourier transform (FFT) at each pixel of the thermal image sequence. Frequency specific amplitude and phase images were obtained corresponding to 1210 nm laser irradiation (Figure 4.6).

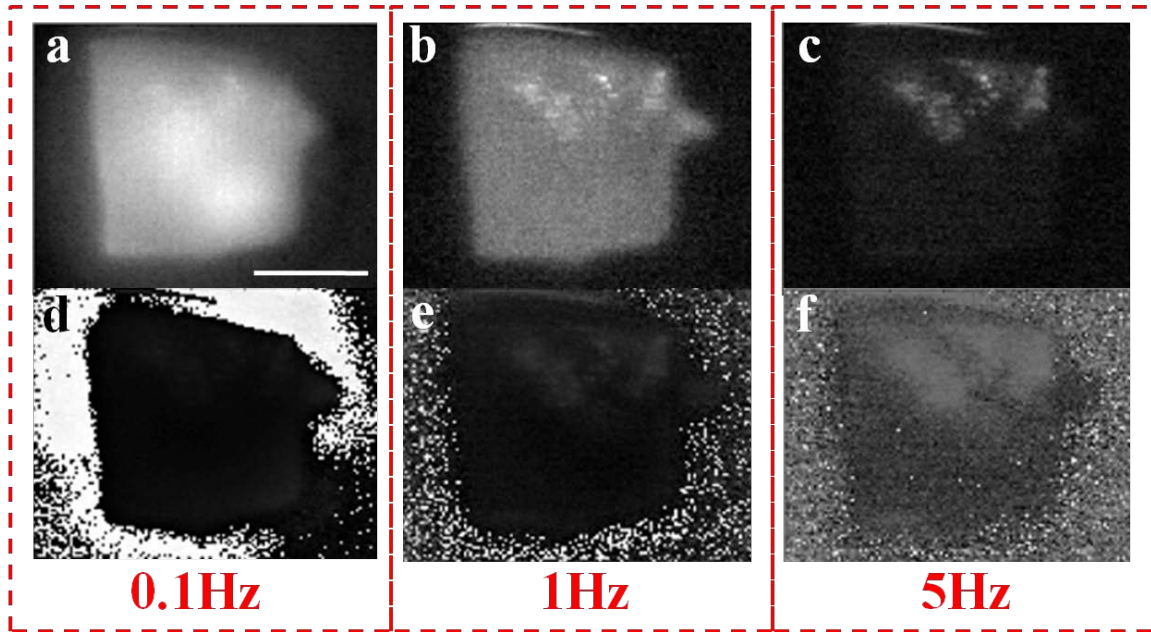


Figure 4.6. (a), (b), (c) FFT amplitude images of a segment of atherosclerotic tissue at modulation frequencies of 0.1, 1 and 5 Hz respectively. (d), (e), (f) FFT phase images of the same tissue at modulation frequencies of 0.1, 1 and 5 Hz respectively. Scale bar is 5 mm.

In both FFT amplitude and phase images (Figure 4.6), lateral distribution of lipid deposits can be identified at plaque locations. Because lower frequencies correspond to deeper thermal wave penetration depth while higher frequencies correspond to more superficial thermal wave penetration depth [4], depth distribution of lipid deposits is evident in both amplitude and phase images.

#### 4.2.4 Discussion

In PTW imaging a common technique to generate thermal waves is through fixed modulation frequency of laser irradiation. Unlike previous studies using a fixed modulation frequency, a swept modulation frequency is used in this study. The advantage of a swept frequency source over the conventional fixed frequency is understood considering the thermal wave penetration depth ( $L_d = (D / \pi f_0)^{1/2}$ , where  $L_d$ ,  $D$  and  $f_0$  are,

respectively, penetration depth, thermal diffusivity and modulation frequency). While a fixed modulation frequency is targeted to one penetration depth, each frequency component in swept modulation frequency corresponds to a different penetration depth allowing interrogation of the depth distribution of lipid deposits.

#### **4.2.5 Conclusion**

Both FFT amplitude and phase images corresponding to 1210 nm laser irradiation suggest that lateral and depth distribution of lipid deposits in atherosclerotic plaque can be identified by PTW imaging at selected modulation frequencies. The shape of atherosclerotic plaque is associated with the distribution of lipid deposits.

#### **4.2.6 References**

- [1] Yusuf S, Reddy S, Ounpuu S, Anand S, “Global burden of cardiovascular diseases: part I: general considerations, the epidemiologic transition, risk factors, and impact of urbanization,” *Circulation* 104, 2746-2753 (2001)
- [2] Davies MJ, Richardson PD, Woolf N, Katz DR, Mann J, “Risk of thrombosis in human atherosclerotic plaques: role of extracellular lipid, macrophage, and smooth muscle cell content,” *Br Heart J* 69, 377-381 (1993)
- [3] Mulaveesala R, Tuli S, “Theory of frequency modulated thermal wave imaging for nondestructive subsurface defect detection,” *Appl Phys Lett* 89, 191-193 (2006)
- [4] Telenkov SA, Vargas G, Nelson JS, Milner TE, “Coherent thermal wave imaging of subsurface chromophores in biological materials,” *Phys Med Biol* 47, 657-671 (2002)

## **4.3 SWEPT-FREQUENCY PTW IMAGING OF NANOROSE IN TISSUE PHANTOMS**

### **4.3.1 Abstract**

We report use of swept-frequency PTW imaging to visualize three-dimensional distribution of nanorose in a phantom mimicking atherosclerotic tissue. The excitation wavelength of 800 nm was selected to target nanorose. The tissue phantoms were irradiated at modulation frequencies ranging from 0.04 Hz to 5 Hz to generate PTWs. The radiometric temperature at phantom surface was recorded by an infrared (IR) camera over a 20 second time period at the frame rate of 12.8 Hz. Extraction of amplitude and phase images (256×256 pixels) at selected frequencies was performed by computing a Fourier transform of the time-dependent radiometric emission at each pixel. Amplitude and phase images were obtained at each modulation frequency and related to depth of nanorose in the phantoms. PTW images recorded from the tissue phantom suggest that three-dimensional distribution of nanorose can be identified by analysis of amplitude and phase images at selected modulation frequencies.

### **4.3.2 Introduction**

Atherosclerosis in combination with rupture of vulnerable plaques is the leading cause of deaths worldwide, surpassing both infectious diseases and cancer. In atherosclerosis, macrophages infiltrate plaques which are characterized by a thin fibrous cap and a lipid core. PTW imaging is based on the periodic thermal modulation of a sample using intensity modulated light. The intensity modulated light is absorbed by target chromophores (nanorose in this study) and generates a periodic thermal modulation.

### 4.3.3 Materials and Methods

In this study, a series of polydimethylsiloxane (PDMS) tissue phantoms were prepared in a two-layered geometry (top-layer and substrate) with different top-layer thicknesses simulating nanoroses imbedded at different depths of the arterial tissue (Figure 4.7). The top-layer ( $d = 130, 450, 930 \mu\text{m}$ ) is composed of PDMS and  $\text{TiO}_2$ , while the substrate (10 mm) is composed of PDMS,  $\text{TiO}_2$  and “UT” letters written by a laser beam on surface of substrate and filled with nanoroses at a concentration of  $5 \times 10^{10}/\text{cm}^3$ . The top-layers were produced by pouring a PDMS solution onto a microscope slide with two identical spacers positioned near the ends of the slide. A second microscope slide was placed on top of the PDMS solution and gently pressed against the spacers. When polymerization was complete after 24 hours, the top slide was carefully removed, exposing a layer of uniform thickness.

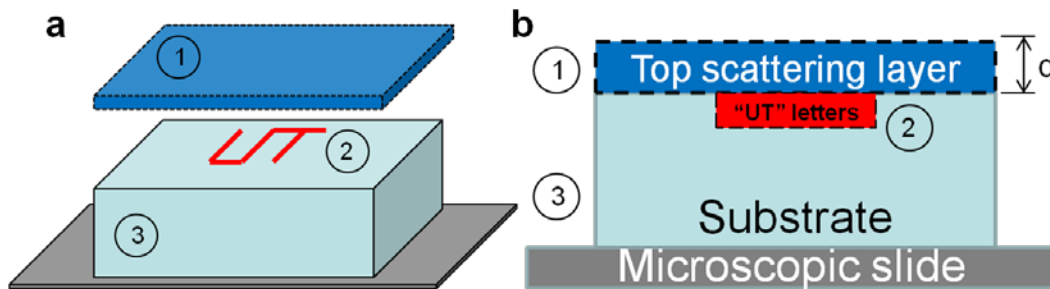


Figure 4.7. Side view (a) and cross-section view (b) of PDMS tissue phantoms. The two-layered geometry consists of top-layer (①), nanoroses (②) and substrate (③).

PTW imaging at fixed frequencies is capable of showing chromophores at different depths. However, the standard approach requires the same amount of recording time for each fixed frequency (i.e., 0.1, 1, 4 Hz). To reduce the recording time, swept laser modulation frequencies were used. A mechanical shutter controlled by a function generator modulated continuous laser light into swept-frequencies (i.e., 0.04-5 Hz). The radiometric temperature at phantom surface was recorded by an infrared (IR) camera over

a 20 second time period at the frame rate of 12.8 Hz. Extraction of amplitude and phase images (256×256 pixels) at selected frequencies was performed by computing a Fourier transform of the time-dependent radiometric emission at each pixel.

#### 4.3.4 Results

Figure 4.8 shows the pixel temperature response ( $T_s$ ) at nanorose location in response to swept-frequency laser modulation irradiation (i.e., 0.04-5 Hz) in PDMS tissue phantom. A third order ( $k = 3$ ) polynomial fit (background) was subtracted from the original temperature response to eliminate lateral heat diffusion, giving much sharper edges at nanorose locations in the tissue phantoms as shown in Figure 4.9.

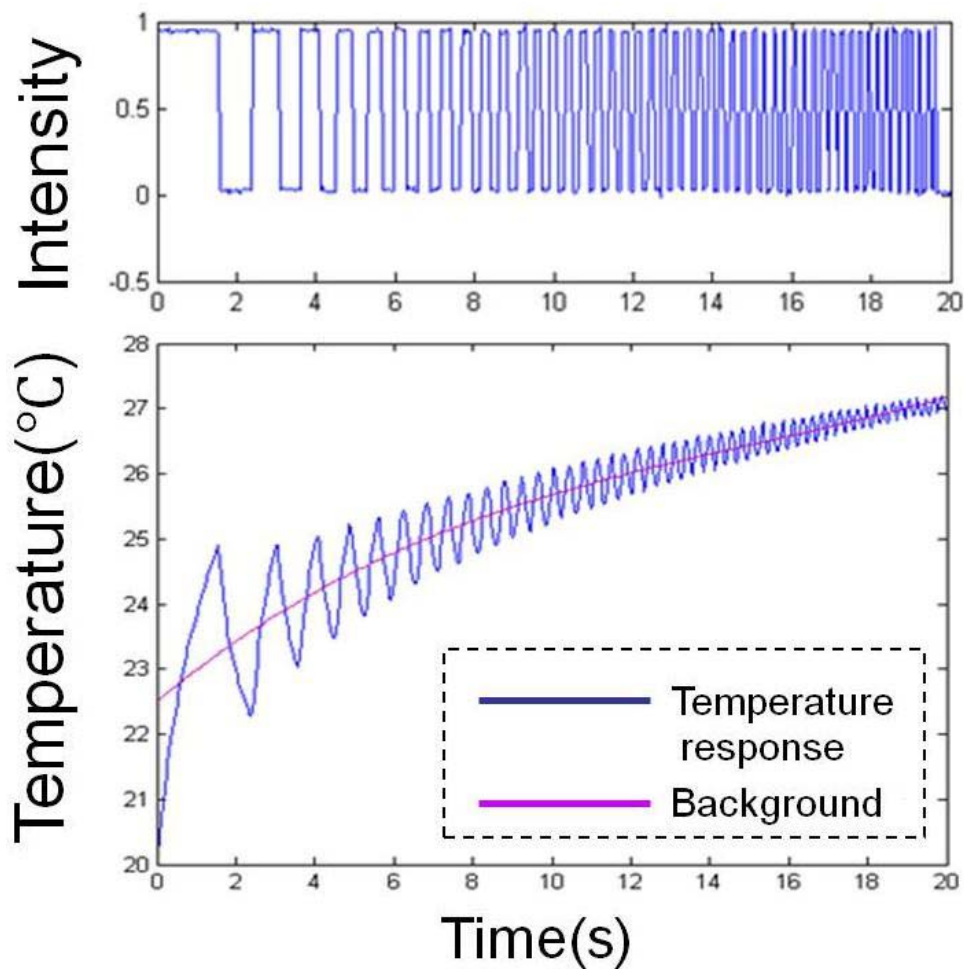


Figure 4.8. Pixel temperature response at nanorose location in response to swept-frequency laser modulation irradiation (800 nm).

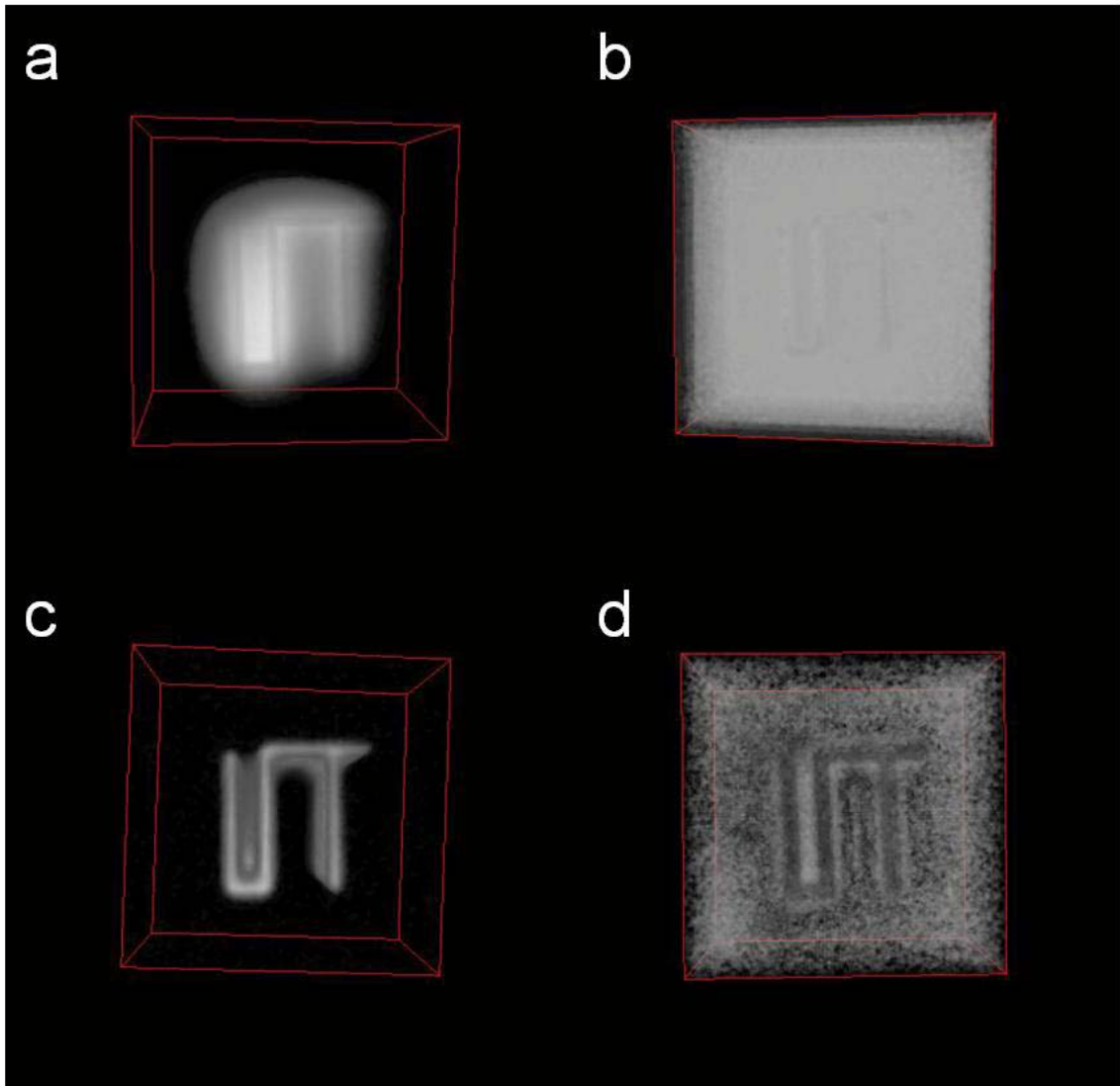


Figure 4.9. Reconstructed three-dimensional amplitude PTW images of nanoroses located at a 130  $\mu\text{m}$  depth in PDMS tissue phantom before (a) and after (c) background subtraction; Reconstructed three-dimensional phase PTW images of nanoroses located at 130  $\mu\text{m}$  depth before (b) and after (d) background subtraction.

Swept-frequency PTW images after background subtraction are shown in Figure 4.10, representing nanoroses at different depths in PDMS tissue phantoms. Each sub-figure in Figure 4.10 is a three-dimensional image reconstructed from a stack of

amplitude PTW image slices. Each image slice from top to the bottom surface represents respectively swept laser modulation frequencies from 5 to 0.04 Hz. “UT” letters composed of nanoroses are located at depths of 130  $\mu\text{m}$  (Figure 4.10a), 450  $\mu\text{m}$  (Figure 4.10b) and 930  $\mu\text{m}$  (Figure 4.10c) respectively. Results show that “UT” letters can be clearly seen from the top to the bottom image slices when nanoroses are located at a 130  $\mu\text{m}$  depth. However, as nanoroses are located deeper in PDMS tissue phantoms, in other words, the top-layer thicknesses of the phantoms increase from 450 to 930  $\mu\text{m}$ , “UT” letters are not observed in top image slices (Figure 4.10b, c). This phenomenon is due to different thermal diffusion lengths at different laser modulation frequencies. Thermal diffusion length is a measure of depth probed by PTWs within the sample defined by  $\mu_D = \sqrt{\alpha / \pi f_m}$ , where  $\mu_D$ ,  $\alpha$  and  $f_m$  are respectively thermal diffusion length, thermal diffusivity and laser modulation frequency. When nanoroses are located deeper, only PTWs at lower laser modulation frequencies (i.e.,  $<5$  Hz) can reach the depth of nanoroses and show contrast in amplitude PTW images.

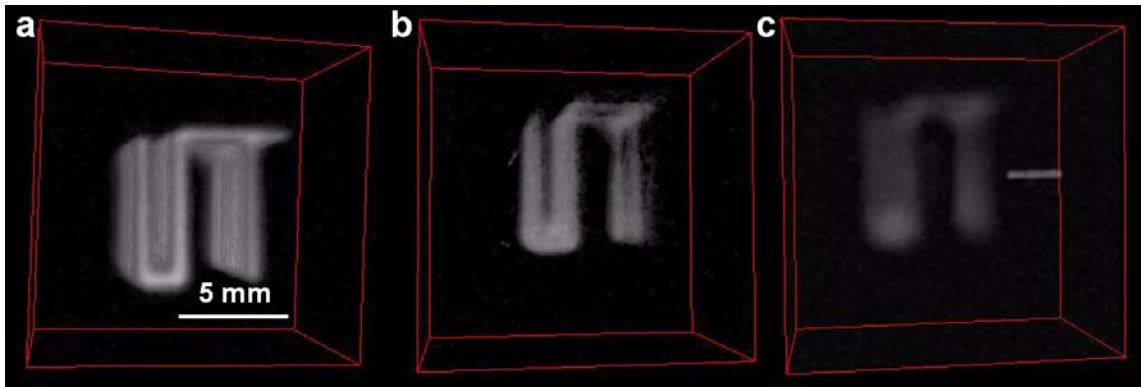


Figure 4.10. Reconstructed three-dimensional amplitude PTW images with nanoroses embedded in PDMS tissue phantoms at depths of (a) 130  $\mu\text{m}$ , (b) 450  $\mu\text{m}$  and (c) 930  $\mu\text{m}$ .

The edge of “UT” letters appear sharper when nanoroses are located at a 130  $\mu\text{m}$  depth (Figure 4.10a) while more blurred edges are observed when nanoroses are located



deeper at 450 and 930  $\mu\text{m}$  depths (Figure 4.10b, c). The result demonstrates that chromophore depth and thermal diffusion length  $\mu_D$  define PTW amplitude response. For laser modulation frequency  $f_m = 0.5$  Hz and thermal diffusivity  $\alpha = 0.104$   $\text{mm}^2/\text{s}$  for PDMS, the thermal diffusion length  $\mu_D = 257$   $\mu\text{m}$ . Amplitude response of superficial chromophores ( $d = 130$   $\mu\text{m} < \mu_D$ ) has sharp edges. In the amplitude response of deeper chromophores ( $d = 450, 930$   $\mu\text{m} > \mu_D$ ), more blurred edges are observed. Though lower modulation frequencies (i.e.,  $f_m < 0.5$  Hz) correspond to longer thermal diffusion lengths and thus are able to generate PTWs that can reach deeper chromophores (i.e.,  $d = 450$  and  $930$   $\mu\text{m}$ ), a longer thermal diffusion time is needed for PTWs to reach surface of the tissue phantom and detected by the infrared camera. As a result, more heat is laterally diffused into the surrounding media and “UT” letters appear more blurred.

#### 4.3.5 Discussion

Although background subtraction provides much sharper edges at nanorose locations in the tissue phantoms as shown in Figure 4.9, this procedure may modify the phase response because subtracting the polynomial fit from the original temperature response can introduce a phase artifact. Moreover, as chromophore depth is dependent on relative phase change to the surface ( $\Delta\theta = L_D / \mu_D$ , where  $\Delta\theta$ ,  $L_D$  and  $\mu_D$  are respectively phase change, chromophore depth and thermal diffusion length), this background subtraction procedure will result in inaccurate calculation of chromophore depth. Therefore, a new background subtraction algorithm is needed to eliminate lateral heat diffusion, in the mean while, preserving the phase response. Specifically, a step temperature response ( $T_c$ ) at the same location from continuous laser irradiation will be recorded (laser power is the mean power of swept-frequency laser modulation irradiation). The subtraction of  $T_c$  from  $T_s$  will preserve the phase information.

The three-dimensional reconstruction algorithm employed in this study is a direct reconstruction from a stack of PTW amplitude/phase image slices from high to low frequencies (i.e., 5-0.04 Hz). However, because each slice contains chromophore information from slices above (higher frequencies than the current slice), a “layer stripping” algorithm [1] may need to be applied to eliminate the affect from overlying slices.

#### **4.3.6 Conclusion**

Swept-frequency PTW imaging is capable to detect nanoroses at different depths. However, when nanoroses are located deeper, blurred edges of chromophores are expected to appear. Based on the results from PDMS tissue phantoms simulating nanoroses imbedded at different depths of the arterial tissue, swept-frequency PTW imaging is able to detect nanoroses as deep as 930  $\mu\text{m}$ .

#### **4.3.7 References**

- [1] Somersalo E, Cheney M, Isaacson D, Isaacson E, “Layer stripping: a direct numerical method for impedance imaging,” *Inverse Prob* 7(6), 899-926 (1991)

## Chapter 5 Fluorescence Imaging of Macrophages in Atherosclerotic Plaques Using Gold Nanoparticles<sup>3</sup>

### 5.1 ABSTRACT

Macrophages are one of the most important cell types involved in the progression of atherosclerosis which can lead to myocardial infarction. To detect macrophages in atherosclerotic plaques, plasmonic gold nanorose is introduced as a nontoxic contrast agent for fluorescence imaging. We report macrophage cell culture and *ex vivo* tissue studies to visualize macrophages targeted by nanorose using scanning confocal microscopy. Atherosclerotic lesions were created in the aorta of a New Zealand white rabbit model subjected to a high cholesterol diet and double balloon injury. The rabbit was injected with nanoroses coated with dextran. A HeNe laser at 633 nm was used as an excitation light source and a acousto-optical beam splitter was utilized to collect fluorescence emission in 650-760 nm spectral range. Results of scanning confocal microscopy of macrophage cell culture and *ex vivo* tissue showed that nanoroses produce a strong fluorescence signal. The presence of nanorose in *ex vivo* tissue was further confirmed by photothermal wave imaging. These results suggest that scanning confocal microscopy can identify the presence and location of nanorose-loaded macrophages in atherosclerotic plaques.

### 5.2 INTRODUCTION

Atherosclerosis is the major pathologic cause of cardiovascular disease (CVD), which is the number one cause of death in the United States - more than any other disease including cancer [1]. From 1900 to 2006, deaths caused by CVD increased dramatically

---

<sup>3</sup> Significant portions of this chapter has been previously published in *Proc SPIE* 7883, 788331-7883318 (2011).

from less than 50,000 to more than 800,000 in the United States [2]. Postmortem studies have revealed that myocardial infarction induced by CVD results from an acute process of plaque rupture or fissuring of modestly stenotic plaques [3-4]. These atherosclerotic plaques are characterized by a thin fibrous cap ( $< 65 \mu\text{m}$ ), a large lipid core and increased macrophage infiltration [5]. Macrophages, originating from monocytes circulating in the blood, are trapped and adhered by the inflammatory endothelial cells in the vessel wall. The activated macrophages infiltrate into the intimal layer of the arterial wall and are capable of degrading the extracellular matrix by secreting matrix metalloproteinases (MMPs) or by reducing collagen synthesis and enhancing smooth muscle cell apoptosis that may weaken the fibrous cap, making it more prone to rupture [6-8]. Clearly, macrophages are one of the key components involved in the pathology and progression of atherosclerosis. The majority of current clinical imaging techniques, including X-ray, computed tomography (CT), coronary angiography, intravascular ultrasound (IVUS) and intravascular optical coherence tomography (IVOCT), focus on detection of morphological alterations of the arterial wall that affect the lumen diameter. However, the assessment of plaque morphology does not provide direct information on staging of atherosclerosis progression and plaque vulnerability. Therefore, molecular imaging techniques such as fluorescence microscopy are being investigated for targeting macrophages in atherosclerotic plaques by using nanoparticles (NPs) as an imaging contrast agent. Scanning confocal microscopy (SCM) is a widely utilized fluorescence microscopy technique for “optical sectioning” of tissue at high resolution [9-10]. When operated in reflectance mode with high incident excitation laser power density, SCM can be used to distinguish cellular components of tissues enhanced by fluorescence dyes. Plasmonic gold nanorose (NR) used to target macrophages in this study is a spectrally-tunable optical nanoaggregate. The 30 nm diameter NR is formed by kinetically

controlled assembly of thin gold-shell coated iron oxide nanoparticles in aqueous medium [11]. Intense NIR (650-800 nm) absorbance is achieved by the asymmetric core-shell geometry and collective plasmonic effects from close spacing between primary particles in the clusters (Figure 5.1a). A dextran coating on NRs enhances macrophage endocytosis and hence macrophages are selectively targeted by NRs. At 633 nm excitation, emission fluorescence spectrum of NR-loaded macrophages is characterized by two fluorescence peaks (650-670 nm and 740-760 nm) in 650-760 nm spectral range (Figure 5.1b). Therefore, NR-loaded macrophages in atherosclerotic plaques are able to provide contrast in 650-760 nm spectral range as a fluorescence contrast agent in SCM.

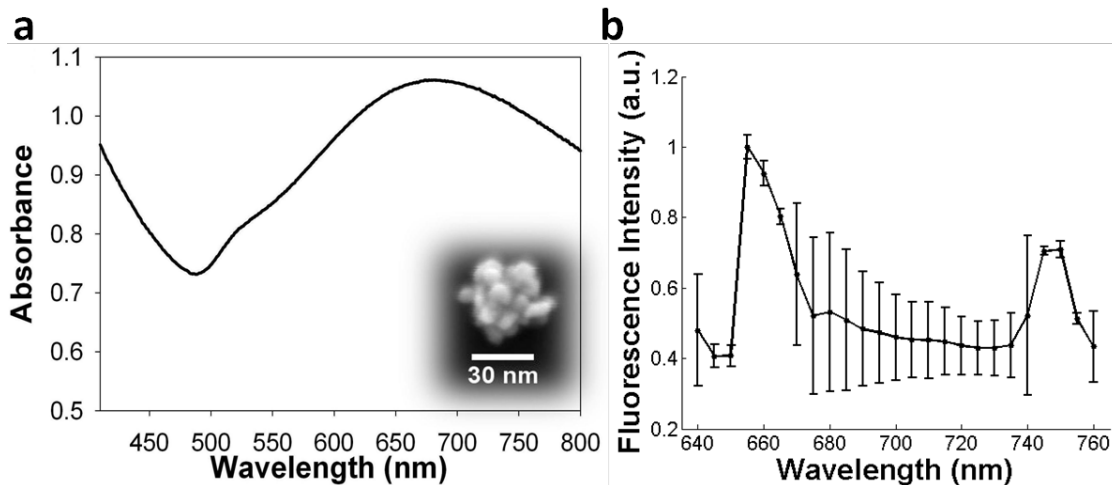


Figure 5.1. (a) Absorbance spectrum of NR colloidal suspension. Inset shows a SEM image of one NR cluster with scale bar. (b) Normalized emission spectrum with scale bar of NR-loaded macrophages at 633 nm excitation.

In this study, we investigated the possibility of using gold NRs as a fluorescence contrast agent for SCM in macrophage cell culture. Macrophage cell culture was chosen to simulate the intimal layer of the atherosclerotic artery since it is well-known that high concentration of macrophages in the arterial intima is a characteristic of atherosclerotic plaques. To further demonstrate that SCM with NRs as a fluorescence contrast agent can be used for imaging superficial macrophages in atherosclerotic plaques, *ex vivo* tissue

experiments were performed on the aortas of a rabbit model of atherosclerosis. Finally, *ex vivo* imaging results from SCM were compared with photothermal wave (PTW) imaging of the same tissue samples to confirm the presence of NRs.

### **5.3 MATERIALS AND METHODS**

#### **5.3.1 Preparation of Macrophage Cell Culture and Ex Vivo Arterial Tissues**

To determine NR uptake by macrophages, mouse peritoneal macrophages characterized by a high uptake rate were used in this study. Macrophage cells were cultivated in DMEM supplemented with 5% FBS at 37 °C in 5% CO<sub>2</sub>. To load cells with NRs, macrophages were incubated with NR suspension ( $\sim 3 \times 10^9$  NRs/ml) in phenol red free and serum free DMEM overnight. NR-loaded macrophages and control macrophages without NR were imaged by SCM.

A double-balloon injury procedure was performed at the bifurcation of the common iliacs on a New Zealand white rabbit. The rabbit was fed a high fat diet for six weeks after balloon injury to induce atherosclerotic lesions. The rabbit was then sacrificed three days after marginal ear vein injection with NRs (1.4 mg NR/kg rabbit body weight). The aorta was harvested and flushed with saline to clear the tissue of red blood cells. The aorta was cut into several tissue samples ( $\sim 8 \times 8$  mm<sup>2</sup>) and placed in a specimen container with saline before imaging. Arterial tissues with NRs and control tissues without NR were imaged by SCM and PTW. All the procedure was performed using sterile equipment, supplies and aseptic technique. The animal protocol was approved by IACUC at the University of Texas Health Science Center at San Antonio.

#### **5.3.2 Imaging Systems**

Fluorescence studies of macrophage cell culture (NR-loaded macrophages and control macrophages without NR) and *ex vivo* arterial tissue (a rabbit with NR injection

and a control rabbit without NR injection) were performed using a scanning confocal microscope (SP2 AOBS, Leica) at the University of Texas at Austin (Figure 5.2a). A single mode HeNe laser (633 nm, 15 mW) was used as an excitation light source. A 10× objective (0.4NA, WD 2200 μm) and an oil immersion 63× objective (1.4NA, WD 100 μm) were used for focusing laser light onto samples and collecting fluorescence emission. The fluorescence emission was spectrally filtered by an acousto-optical beam splitter (650-760 nm), focused onto a 75 μm pinhole for spatial filtering to reject out-of-focus signals and then reached a PMT (R6357, Hamamatsu).

To compare and verify the SCM results, PTW imaging was performed using a custom-built PTW imaging system (Figure 5.2b). A lens coupled fiber optic laser (FCTS/B, Opto Power) at a wavelength of 800 nm with maximum output power of 5 W was used to irradiate arterial tissues to induce photothermal waves. A mechanical shutter controlled by a function generator intensity-modulated continuous laser light at a frequency of 4 Hz. The IR signal (radiometric temperature) emitted from tissue surface was reflected by a dichroic mirror and recorded by an IR camera (SC6000, FLIR) at an acquisition frame rate of 25.6 Hz. The extraction of amplitude PTW images (256 × 256 pixels) at various frequencies was performed by computing a fast Fourier transform (FFT) at each pixel of the recorded temporal IR image sequence.

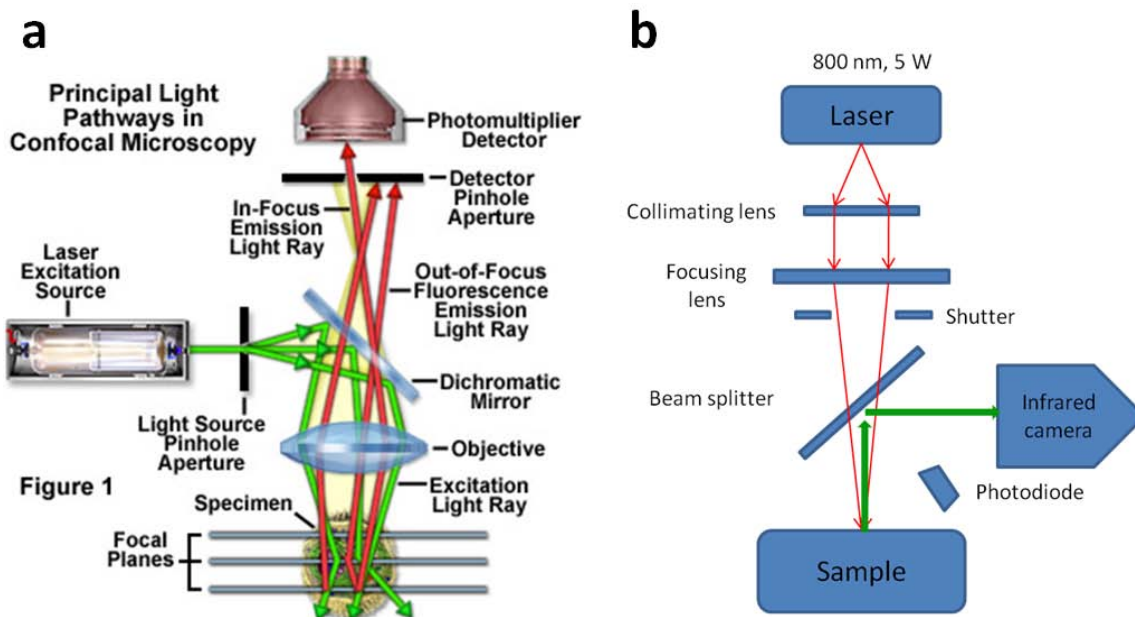


Figure 5.2. Schematic diagrams of (a) SCM (adapted from [12]) and (b) PTW imaging (adapted from [13]).

## 5.4 RESULTS

### 5.4.1 Fluorescence of NRs in Macrophage Cell Culture

Differential interference contrast (DIC) images of NR-loaded macrophages and control macrophages without NR are recorded using a 63 $\times$  objective in SCM and shown respectively in Figure 5.3a, d. DIC images of macrophage cells clearly demonstrate the structures of cell membrane and nuclei. NRs are accumulated and identified as a black color inside and outside the macrophage (Figure 5.3a). High accumulation of NRs in macrophages suggests that macrophage endocytosis process may be enhanced due to dextran coating on NRs. Fluorescence images recorded in 650-760 nm spectral range collected by SCM are shown in Figure 5.3b, e. Strong fluorescence signals are observed in the NR-loaded macrophage (Figure 5.3b) but not in the control macrophage without NR (Figure 5.3e). After image processing, fluorescence images, overlaid in co-registered DIC images (Figure 5.3c, f), identify the location of NRs in the macrophage and confirm



that fluorescence signals are generated from NRs (Figure 5.3c) and not other cell components (Figure 5.3f). Therefore, NR can be used as a fluorescence contrast agent in SCM for targeting macrophages.

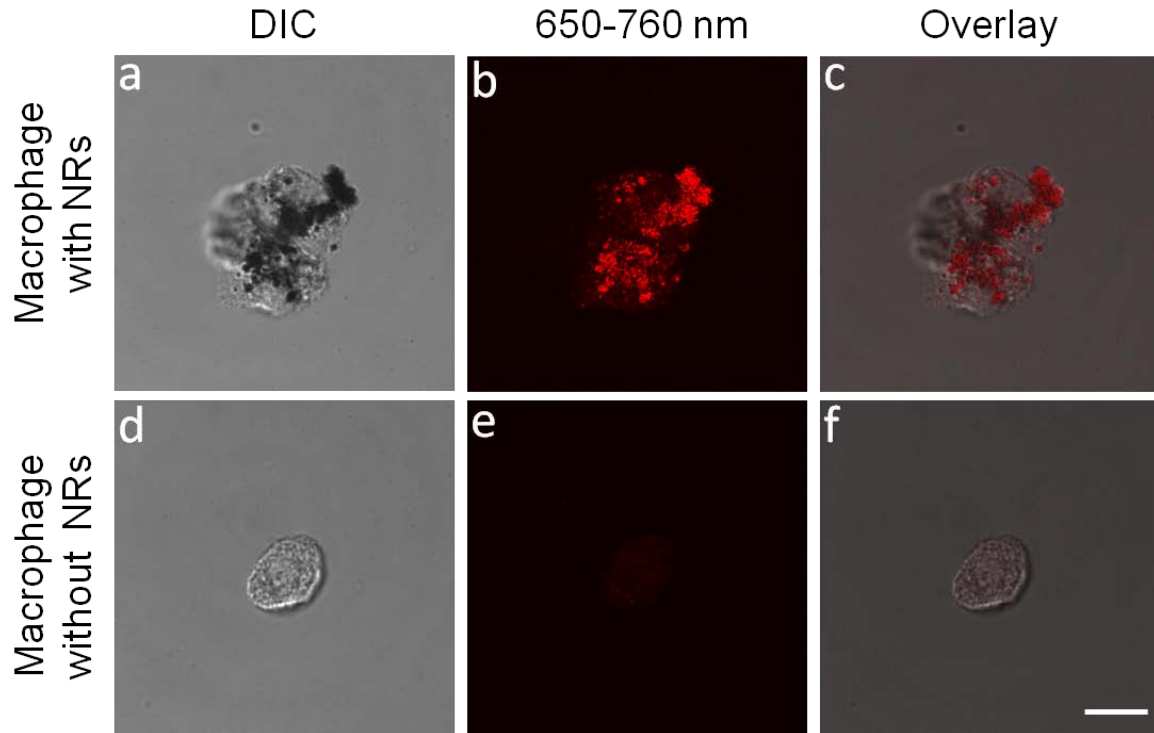


Figure 5.3. (a, d) DIC images, (b, e) fluorescence images (650-760 nm) and (c, f) overlay images of macrophage cell culture with and without NRs. Scale bar is 10  $\mu\text{m}$ .

#### 5.4.2 Fluorescence of NRs in Arterial Tissues

To further demonstrate that SCM with NRs as a fluorescence contrast agent can be used for imaging macrophages in atherosclerotic plaques, *ex vivo* tissue experiments were performed on a NR injected rabbit and a control rabbit without NR injection. *Ex vivo* arterial tissue samples were imaged by SCM using a 10 $\times$  objective, transmission and fluorescence images are shown in Figure 5.4. Strong fluorescence signals in the tissue sample (Figure 5.4c corresponding to the red square region in Figure 5.4a) from a NR injected rabbit may indicate the locations of NR-loaded macrophages on the surface of

atherosclerotic plaque. The distribution of NR-loaded macrophages in the red square region in Figure 5.4a can be better visualized in a 3-D view (Figure 5.4g). The 3-D image was reconstructed from 92 frames of lateral scans from the tissue sample surface with 1  $\mu\text{m}$  apart between each frame. The deposition of NR-loaded macrophages can be observed in all the frames, which may indicate that NR-loaded macrophages are diffusively distributed in the superficial layer (intima) of the aorta. In contrast, fluorescence signals are not detected in the tissue sample (Figure 5.4f corresponding to the red square region in Figure 5.4d) from a control rabbit without NR injection using the same laser output and PMT amplification.

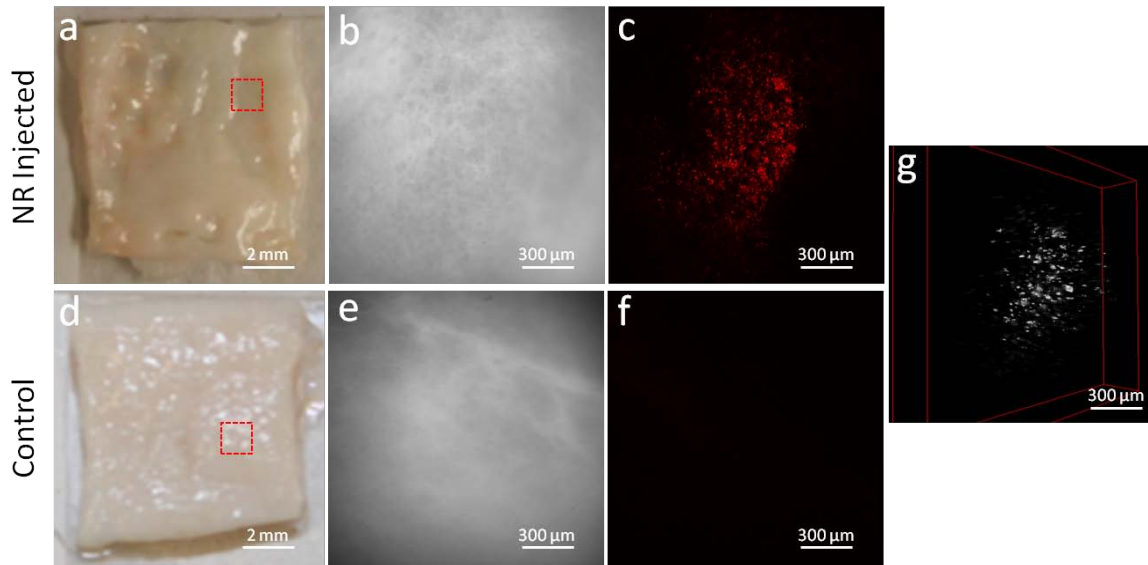


Figure 5.4. (a, d) Digital images, (b, e) transmission images and (c, f) fluorescence images (650-760 nm) of rabbit arterial tissue samples with and without NRs. (g) Reconstructed 3-D fluorescence image of red square region in (a).

Due to intense absorption in the NIR spectral range compared to other arterial tissue components, NR can provide contrast in PTW imaging. Therefore, PTW imaging was performed to verify the presence of NRs in the same tissue samples as shown in Figure 5.4a, d. Because the thermal diffusion length is dependent on laser modulation

frequency ( $\mu = \sqrt{\alpha / \pi f}$ , where  $\mu$ ,  $\alpha$ ,  $f$  are respectively thermal diffusion length, thermal diffusivity and laser modulation frequency), a higher modulation frequency corresponds to shorter thermal diffusion length and hence superficial absorbers. A modulation frequency of 4 Hz was utilized to detect superficial NRs. Amplitude PTW images were obtained corresponding to 800 nm laser irradiation (Figure 5.4a, b). High intensity amplitude signals, as denoted by a higher grey value in Figure 5.5a, are detected from the same tissue sample as shown in Figure 5.4a. NRs are diffusively distributed on plaque surface. The red square region in Figure 5.5a, co-localized with that in Figure 5.4a, suggests high concentration of NRs. In contrast, no grey value contrast is observed in Figure 5.5b representing the same tissue sample as shown in Figure 5.4d. The red square region in Figure 5.5b, co-localized with that in Figure 5.4d, has similar grey values compared with surrounding tissue, suggesting no NR is detected in this region. Figure 5.5c shows the average radiometric temperature increase of the red square regions in Figure 5.5a, b in response to laser irradiation. Temperature increase in NR region (red square in Figure 5.5a) after ten second laser irradiation is more than two times higher than that in control tissue without NR (red square in Figure 5.5b). Moreover, the temperature modulation amplitude of NR region is much larger than that of control tissue without NR (Figure 5.5c). Results of PTW imaging confirm that fluorescence signals obtained by SCM as shown in Figure 5.4c, g are from NRs.

Therefore, the *ex vivo* tissue experiment suggests that SCM is capable to detect NR-loaded macrophages in atherosclerotic plaques.

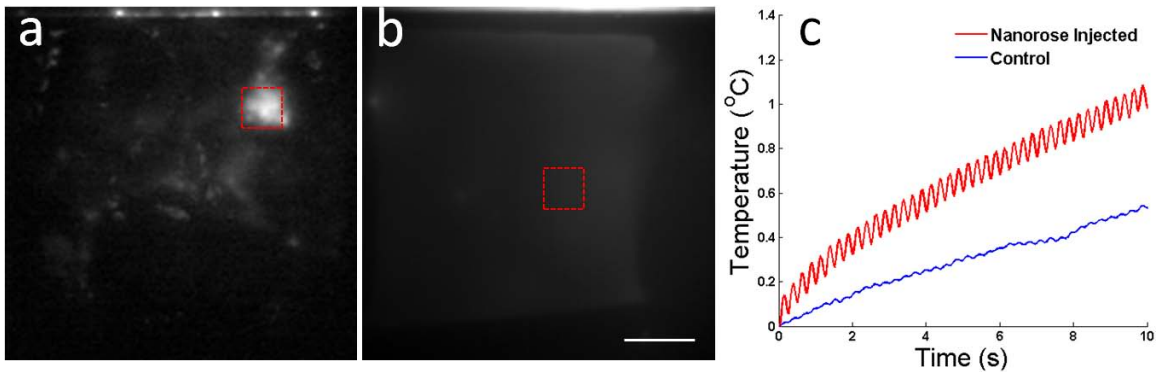


Figure 5.5. (a) Amplitude PTW image of the tissue sample as shown in Figure 5.4(a) at a laser modulation frequency of 4 Hz. (b) Amplitude PTW image of the tissue sample as shown in Figure 5.4(d) at a laser modulation frequency of 4 Hz. Scale bar is 2 mm. (c) Average radiometric temperature increases of red square regions in (a, b) in response to laser irradiation within first ten seconds.

## 5.5 DISCUSSION AND CONCLUSION

Although high yield delivery of NRs into macrophages in atherosclerotic plaques was achieved by conjugating dextran to NRs, other biomarkers such as matrix metalloproteinases (MMPs) [14] and stromelysin-3 [15] are also identified at atherosclerotic lesions. Therefore, investigation of NRs selectively targeting MMPs and stromelysin-3 may provide diagnostic value.

The fluorescence emission spectrum collected in our study is in the range of 650-760 nm. This spectral range is chosen because NR has two fluorescence emission peaks (650-670 nm and 740-760 nm) in this range in response to 633 nm excitation. The fluorescence contrast provided by NR in SCM is due to these two emission peaks. However, further studies are needed to investigate fluorescence emission spectra of NR in response to NIR (650-800 nm) excitation. Due to stronger absorption in NIR range, NR with NIR excitation has the possibility to absorb more strongly than 633 nm excitation and fluoresce at longer wavelengths. Therefore, better penetration depth of SCM may be achieved and deeper NRs could be detected.

In this study, we demonstrated that gold NRs can be used as a fluorescence contrast agent for SCM in macrophage cell culture. Results of *ex vivo* tissue experiments showed that SCM is capable of *ex vivo* detection of NRs that were intravenously injected and endocytosed by macrophages in atherosclerotic plaques of rabbit aorta *in vivo*. In addition, results of PTW imaging of the same tissue samples confirms that fluorescence signals detected by SCM in *ex vivo* arterial tissue are from NRs and not other tissue components in the aorta.

## 5.6 ACKNOWLEDGEMENTS

This work was partially supported by a Veterans Administration Merit Grant. The authors also would like to acknowledge the technical support from the University of Texas Health Science Center at San Antonio.

## 5.7 REFERENCES

- [1] American Heart Association, Available at <http://www.americanheart.org/presenter.jhtml?identifier=3038611>
- [2] American Heart Association, Available at <http://www.americanheart.org/presenter.jhtml?identifier=4478>
- [3] Pasterkamp G, Falk E, Woutman H, Borst C, "Techniques characterizing the coronary atherosclerotic plaque: influence on clinical decision making?," J Am Coll Cardiol 36, 13-21 (2000)
- [4] Virmani R, Kolodgie FD, Burke AP, Farb A, Schwartz M, "Lessons from sudden coronary death. A comprehensive morphological classification scheme for atherosclerotic lesions," Arterioscler Thromb Vasc Biol 20, 1262-1275 (2000)

- [5] Davies MJ, Richardson PD, Woolf N, Katz DR, Mann J, "Risk of thrombosis in human atherosclerotic plaques: role of extracellular lipid, macrophage, and smooth muscle cell content," *Br Heart J* 69, 377-381 (1993)
- [6] Libby P, Aikawa M, "Stabilization of atherosclerotic plaques: New mechanisms and clinical targets," *Nature Med* 8, 1257-1262 (2002)
- [7] Galis ZS, Sukhova GK, Kranzhofer R, Clark S, Libby P, "Macrophage foam cells from experimental atheroma constitutively produce matrix-degrading proteinases," *Proc Natl Acad Sci* 92(2), 402-406 (1995)
- [8] Falk E, Shah PK, Fuster V, "Coronary plaque disruption," *Circulation* 92(3), 657-671 (1995)
- [9] Rajadhyaksha M, Grossman M, Esterowitz D, Webb RH, Anderson RR, "In vivo confocal scanning laser microscopy of human skin: melanin provides strong contrast," *J Invest Dermatol* 104, 946-952 (1995)
- [10] Rajadhyaksha M, González S, Zavislan JM, Anderson RR, Webb RH, "In vivo confocal scanning laser microscopy of human skin II: advances in instrumentation and comparison with histology," *J Invest Dermatol* 113(3), 293-301 (1999)
- [11] Ma LL, Feldman MD, Tam JM, Paranjape AS, Cheruku KK, Larson TA, Tam JO, Ingram DR, Paramita V, Villard JW, Jenkins JT, Wang T, Clarke GD, Asmis R, Sokolov K, Chandrasekar B, Milner TE, Johnston KP, "Small multifunctional nanoclusters (nanoroses) for targeted cellular imaging and therapy," *ACS Nano* 3(9), 2686-2696 (2009)
- [12] Available at <http://www.biology.wustl.edu/imaging-facility/specs-leica.php>
- [13] Wang T, Qiu J, Ma LL, Li X, Sun J, Ryoo S, Johnston KP, Feldman MD, Milner TE, "Nanorose and lipid detection in atherosclerotic plaque using dual-wavelength photothermal wave imaging," *Proc SPIE* 7562, 75620S-75620S-7 (2010)

- [14] Virmani R, Burke AP, Kolodgie FD, Farb A, "Pathology of the thin-cap fibroatheroma: a type of vulnerable plaque," *J Interven Cardiol* 16(3), 267-272 (2003)
- [15] Schonbeck U, Mach F, Sukhova GK, Atkinson E, Levesque E, Herman M, Graber P, Basset P, Libby P, "Expression of stromelysin-3 in atherosclerotic lesions: regulation via CD40- CD40 ligand signaling in vitro and in vivo," *J Exp Med* 189, 843-853 (1999)

## Chapter 6 PTW Imaging Combined with OCT for Macrophage and Lipid Detection in Atherosclerotic Plaques Using Gold Nanoparticles<sup>4</sup>

### 6.1 ABSTRACT

The objective of this study was to assess the ability of combined photothermal wave (PTW) imaging and optical coherence tomography (OCT) to detect, and further characterize the distribution of macrophages (having taken up plasmonic gold nanorose as a contrast agent) and lipid deposits in atherosclerotic plaques. Aortas with atherosclerotic plaques were harvested from 9 male New Zealand white rabbits divided into nanorose- and saline-injected groups and were imaged by dual-wavelength (800 and 1210 nm) multi-frequency (0.1, 1 and 4 Hz) PTW imaging in combination with OCT. Amplitude PTW images suggest that lateral and depth distribution of nanorose-loaded macrophages (confirmed by two-photon luminescence microscopy and RAM-11 stain) and lipid deposits can be identified at selected modulation frequencies. Radiometric temperature increase and modulation amplitude of superficial nanoroses in response to 4 Hz laser irradiation (800 nm) were significantly higher than native plaque ( $P < 0.001$ ). Amplitude PTW images (4 Hz) were merged into a co-registered OCT image, suggesting that superficial nanorose-loaded macrophages are distributed at shoulders on the upstream side of atherosclerotic plaques ( $P < 0.01$ ) at edges of lipid deposits. Results suggest that combined PTW-OCT imaging can simultaneously reveal plaque structure and composition, permitting characterization of nanorose-loaded macrophages and lipid deposits in atherosclerotic plaques.

---

<sup>4</sup> Significant portions of this chapter have been previously published in *J Biomed Opt* 17(3), 03600901-03600910 (2012).



## 6.2 INTRODUCTION

Atherosclerosis remains the leading cause of death worldwide [1]. The macrophage is an important early cellular marker that provides information relevant to the risk of future rupture of atherosclerotic plaques. Macrophage infiltration into the intimal layer of plaques accelerates inflammation by releasing matrix metalloproteinases (MMPs) which erode the fibrous cap and make the plaques more prone to rupture [2-3]. Lipid is another important constituent in the progression of atherosclerosis. After entering an activated endothelial layer, low density lipoproteins (LDL) are taken up by macrophages which have entered the arterial wall. These LDL-loaded macrophages are observed in the lipid core as foam cells in post-mortem vulnerable plaques [4-5]. Since the vulnerability of plaques is related to cellular composition as well as anatomical structure [6], developing a diagnostic method that can simultaneously reveal both is critical to identify vulnerable plaques and would allow the determination of macrophage density in longitudinal studies in response to therapies without cutting tissue.

Optical coherence tomography (OCT) has been demonstrated to visualize microstructural features such as fibrous cap and surface structure of atherosclerotic plaques with high resolution [7-10]. Although Tearney *et al* showed a correlation between OCT and histological measurements of macrophage density in the center of fibrous caps [11], and more recently, Liu *et al* showed that micro-OCT is capable of detecting plaque-based macrophages with higher resolution [12], the specificity of OCT/micro-OCT alone to identify macrophages is limited by scattering contrast between macrophages, lipids and other plaque components such as crystals of cholesterol esters and microcalcifications. Photothermal wave (PTW) imaging is a potential screening tool for imaging and distinguishing macrophages and lipid deposits in atherosclerotic plaques. PTW imaging is based on absorption of light by targeted chromophores which generate a

periodic thermal modulation [13-15]. Differences in optical absorption among tissue constituents provide contrast in PTW imaging [16]. Multi-wavelength PTW imaging can selectively visualize different chromophores in plaque that absorb at selected laser irradiation wavelengths. Multi-frequency PTW imaging can localize chromophores at multiple depths due to different thermal diffusion lengths at selected modulation frequencies [17]. The combination of PTW imaging and OCT may identify the distribution of macrophages and lipid deposits in the context of anatomical plaque structure in a single merged PTW-OCT image.

No endogenous optical absorption contrast exists between macrophages and other plaque components. A novel gold nanoparticle called nanorose was developed by our group to serve as a macrophage targeting chromophore and has been shown to be taken up much more aggressively by macrophages than either aortic smooth muscle cells or aortic endothelial cells [18]. The 30 nm diameter nanoroses are formed by kinetically controlled assembly of thin gold shell coated iron oxide nanoparticles in aqueous medium. Nanoroses were injected intravenously, engulfed by plaque-based macrophages or blood-based monocytes due to a dextran coating [19], and utilized as a contrast agent for PTW imaging to identify macrophages. Broad near infrared (650-800 nm) absorption of nanorose with an absorption cross-section (in solution) of  $3.1 \times 10^{-14} \text{ m}^2$  at a wavelength of 800 nm is achieved by the asymmetric core-shell geometry and plasmonic effects from close spacing between primary particles in the cluster [Figure 6.1(a)]. Nanorose specificity is provided since the absorption spectra of lipid and other plaque components are known to nadir at 800 nm [20] while nanorose has high absorption at this wavelength. Moreover, since fatty acids have a local absorption maxima around 1210 nm while the absorption of water is relatively lower and nearly constant in this spectral range [Figure 6.1(b)] [21-22], lasers that emit at wavelengths of 800 nm and 1210 nm were selected to

target nanorose and lipid respectively in PTW imaging. Nanorose concentration of  $\sim 2 \times 10^{10}$  particles/ml, approximately equal to that on plaque surfaces in our *ex vivo* animal studies, was measured and corresponding nanorose absorption coefficient spectrum is shown [Figure 6.1 (b)].

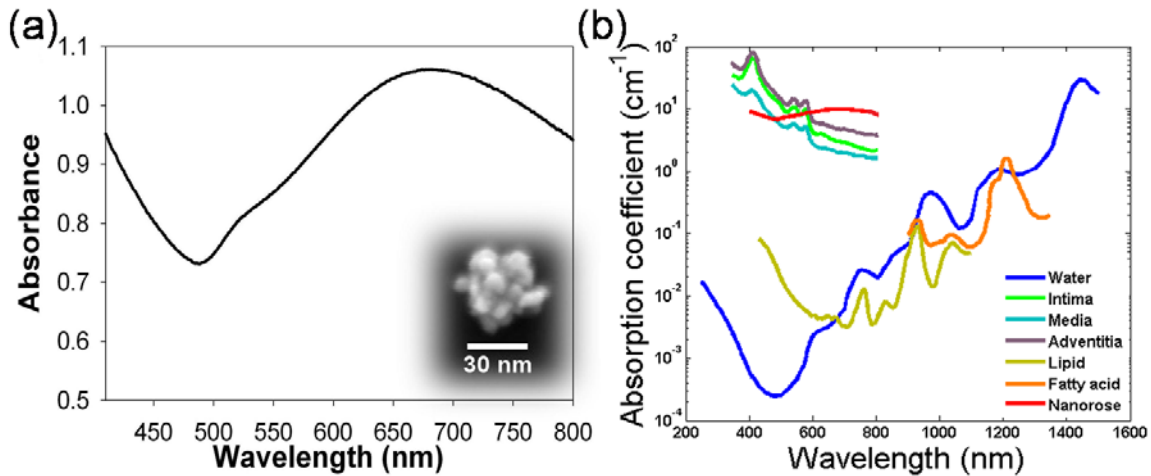


Figure 6.1. (a) Absorbance spectrum of nanorose colloidal suspension. Inset shows a scanning electron microscopy (SEM) image of a single nanorose cluster. (b) Absorption coefficient spectra of arterial tissues, lipid, water and nanorose. Nanorose concentration was typical of that found inside macrophages on plaque surface, based on surface radiometric temperature measurement in response to a pulsed laser irradiation at 800 nm [23].

In this study, we demonstrate for the first time that combined PTW-OCT imaging can identify nanorose-loaded macrophages and lipid deposits in a rabbit atherosclerosis model. Presence of nanorose-loaded macrophages was confirmed by co-localization of two-photon luminescence (TPL) microscopy of nanorose and RAM-11 stain of macrophages in histological sections. Our results suggest that nanorose-loaded macrophages are (1) localized at the shoulders on the upstream side of atherosclerotic plaques associated with lipid deposits and (2) detected superficially within 20  $\mu\text{m}$  of plaque surface. This approach could be used to characterize the distribution of nanorose-loaded macrophages and lipid deposits in atherosclerotic plaques.

## **6.3 MATERIALS AND METHODS**

### **6.3.1 Macrophage Cell Culture**

To demonstrate nanorose uptake by macrophages, C57/BLK6 mouse peritoneal macrophages were incubated with nanorose suspension. Macrophage cells were cultivated in Dulbecco's modified Eagle's medium (DMEM) supplemented with 10% fetal bovine serum (FBS), L-glutamine (2 mM), penicillin (50 U/ml) and streptomycin (100 µg/ml) at 37°C in 5% CO<sub>2</sub>. To load cells with nanorose, macrophages were incubated with nanorose suspension (approximately  $3 \times 10^9$  nanoroses/ml) in phenol red free and serum free DMEM overnight. Nanorose-loaded macrophages and control macrophages without nanorose were imaged by transmission electron microscopy (TEM).

### **6.3.2 Preparation of Rabbit Arterial Tissues**

A rabbit animal model of atherosclerosis was used to create macrophage-rich atherosclerotic plaques in the aorta [24]. Nine male New Zealand white rabbits were fed a 0.25% cholesterol chow for six months. Six rabbits (Positive group) were sacrificed three days following marginal ear vein injection with nanorose (1.4 mg Au/kg rabbit body weight) as done previously [25]. The dose of nanorose injection used in this study is comparable to the current FDA approved value of 100 mg for a single injection of gold sodium thiomalate (per a 70 kg human body) used in the treatment of rheumatoid arthritis [26]. The remaining three rabbits (Control group) were sacrificed three days following saline injection. The aortas were harvested, cut open, flushed clean of red blood cells and placed in sample containers with saline and stored at 4°C before use. Several plaque segments (about  $8 \times 8 \times 2$  mm<sup>3</sup>) were harvested from the aortas (44 plaque segments from the Positive group and 30 plaque segments from the Control group) and positioned en

face onto glass-slide sample holders with the luminal side face-up to be imaged by PTW imaging and OCT. Orthogonally oriented tape rulers affixed to sample holders indicated coordinate positions of plaque segments so that recorded PTW and OCT images could be co-registered. All imaging experiments were completed within 12 hours after animal sacrifice. The animal protocol was approved by the University of Texas Health Science Center at San Antonio IACUC.

### **6.3.3 Imaging Systems**

#### **6.3.3.1 PTW Imaging**

Schematic diagram of a custom-built PTW imaging system used in this study is presented in Figure 6.2(a). Two lens coupled fiber optic lasers (FCTS/B, Opto Power; 1200-001, Candela) that emit at wavelengths of 800 and 1210 nm respectively with radiant output power of 0.25 W were used to irradiate plaque segments to induce PTWs. A 50 mm diameter lens ( $f=40$  cm) was used to focus the laser beam to a 1 cm diameter spot size on the plaque segments. A mechanical shutter controlled by a function generator (not shown in Figure 6.3) intensity-modulated continuous laser light at fixed frequencies (0.1, 1, and 4 Hz) with a 50% duty cycle. The infrared (IR) signal (radiometric temperature) emitted from plaque surface was reflected by a dichroic beam splitter and recorded by an IR camera (SC6000 with an InSb detector (3.0-5.0  $\mu\text{m}$ ), FLIR) over a 20 second time period at a frame acquisition rate of 25.6 Hz. The extraction of amplitude and phase PTW images (256 $\times$ 320 pixels) at each modulation frequency was performed by computing a fast Fourier transform (FFT) at each pixel of the recorded temporal IR image sequence.

### 6.3.3.2 OCT

A swept source (SS) laser (HSL-1000, Santec) with center wavelength of 1060 nm and a bandwidth of 80 nm scanning at a repetition rate of 34 KHz was used in the custom-built intensity OCT system [Figure 6.2(b)]. Power at the sample arm was 1.2 mW. The measured free space axial resolution was 20  $\mu\text{m}$  with a 2.8 mm scan depth. The OCT signal was sampled with a linear k-space sampling clock to allow real-time OCT image acquisition and display. The linear k-space clock was generated from a portion of the source light directed into a Mach-Zehnder interferometer and detected by a balanced detector. This clock signal was filtered, frequency-quadrupled and used as the input to the external clock port of the ADC card. The laser sweep rate governs the A-scan rate of 34 kHz and images were acquired at a rate of 68 B-scans per second with 500 A-scans per B-scan.

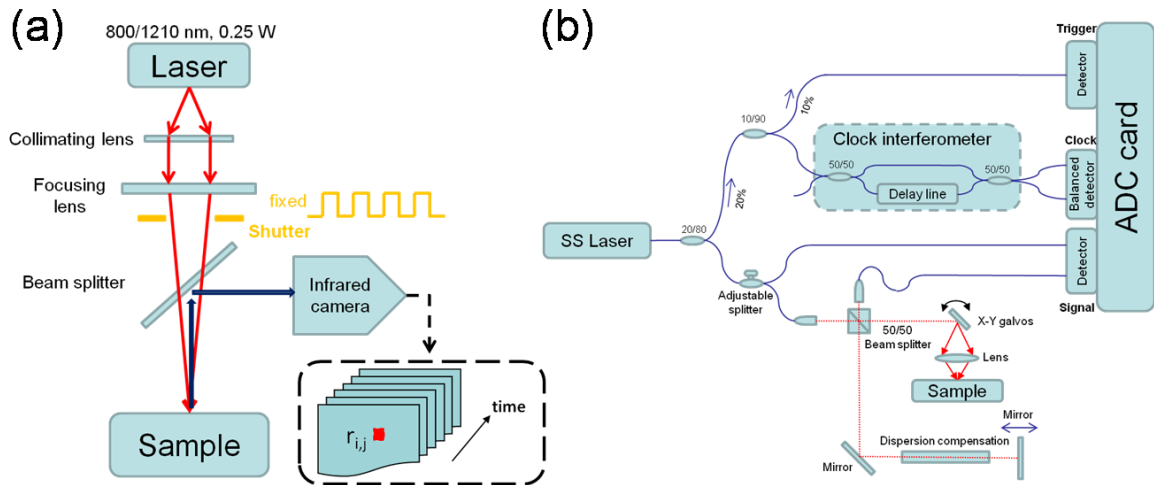


Figure 6.2. Schematic diagrams of (a) PTW imaging instrumentation to measure the IR signal from plaques in response to periodic laser irradiation (800 and 1210 nm) and (b) intensity OCT system to measure plaque surface structure. SS: swept source.

### 6.3.3.3 TPL Microscopy

Measurements of TPL from nanoroses were performed using the custom-built NIR laser scanning multiphoton microscope described in a previous study [27]. As the

TPL excitation source, a femtosecond Ti:Sapphire laser (Mira 900, Coherent) with excitation wavelength of 800 nm was used. The laser beam entering the microscope was modulated by an acousto-optic modulator (AOM: 23080-1, NEOS Technologies). The focal volume of the objective lens (20×, NA=0.95, water emersion, Olympus) was scanned along the sample in the x-y plane using a pair of galvanometric scanning mirrors (6215HB, Cambridge Technology) to produce 2-D images. TPL from plaque segments was detected by two photomultiplier tubes (PMT1: H7422P-40, PMT2: H7422P-50, Hamamatsu) through a dichroic beam splitter (FF735-Di01, Semrock). TPL emission spectra (in response to 800 nm excitation) of plaque components such as collagen, elastin fibers, oxidized-LDL, neutral lipid and calcification are well below 650 nm [28-30] while nanorose has intensive and broad luminescence emission within the wavelength band of 650-750 nm, endogenous plaque fluorescence and nanorose luminescence were separated by a long-pass filter (E570LP, Chroma Technology) with reflection wavelengths shorter than 570 nm and a band-pass filter (HQ700/75m, Chroma Technology) with center wavelength of 700 nm. Wavelengths shorter than 570 nm from endogenous plaque fluorescence were collected by PMT1. Wavelengths longer than 570 nm from nanorose luminescence transmitted through the band-pass filter and were collected by PMT2. The average Ti:Sapphire laser power incident at the tissue surface was 20 mW and no nanorose damage or photo-bleaching effect was observed during imaging.

#### **6.3.4 Histology Analysis**

Aorta sections (5  $\mu$ m in thickness) were immersion-fixed in formalin, processed with paraffin embedding and stained with RAM-11 [31], a marker of rabbit macrophage cytoplasm.

### **6.3.5 Statistical Analysis**

Statistical analysis was performed using SPSS Software for Windows (Version 19.0.0, SPSS). Radiometric temperature increase of plaque is given as mean temperature increase per excitation pulse over specific regions (nanorose regions in the Positive group and plaque regions with no nanorose in the Control group) in each plaque segment using PTW imaging. The comparison of superficial nanorose distribution in plaques is given as an area percentage of nanorose at plaque shoulders on the upstream versus downstream side. A two-tailed independent-sample Student's *t* test was performed for comparison of mean temperature increase of plaques from Positive and Control groups. The findings of nanorose distribution in plaques from the Positive group were compared by applying a two-tailed paired-sample Student's *t* test. A two-tailed *P* value less than 0.05 was considered statistically significant for both tests.

### **6.3.6 Analysis of Area Percentage of Nanorose in Plaques**

Area percentage of nanorose at plaque shoulders on the upstream versus downstream side in each plaque segment (N=44) in the Positive group was calculated according to the ratio of nanorose pixel number defined by the pixel number of nanorose at plaque shoulders on the upstream versus downstream side, respectively, to a total pixel number of nanorose in each plaque segment. ImageJ software was used for the percentage measurement. Data are presented as mean±SD.

## **6.4 RESULTS**

### **6.4.1 Nanorose Uptake by Macrophages**

After overnight (24 hours) macrophage incubation, nanoroses are observed to accumulate in lysosomes inside macrophages [Figure 6.3(a)]. Nanoroses are not localized in all lysosomes but appear more frequently in those close to the cell surface. Both single



nanorose and nanorose clusters are observed (inset in [Figure 6.3 (a)], suggesting that nanoparticle aggregation occurs during macrophage internalization. Dense accumulation of nanoroses in lysosomes indicates substantial macrophage endocytosis of 30 nm dextran-coated nanorose in cell culture.

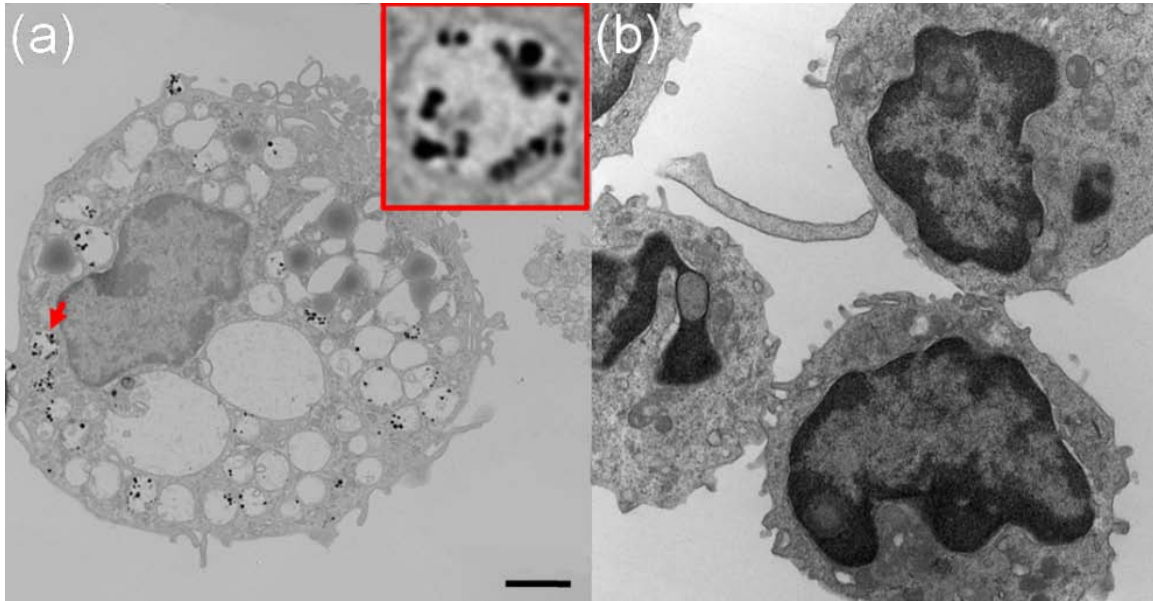


Figure 6.3. TEM images of (a) peritoneal macrophages loaded with nanorose and (b) peritoneal macrophages without nanorose. Red arrow points to a lysosome which is magnified in a red square at the upper right corner in (a) where single nanorose and nanorose clusters are observed. Scale bar is 2  $\mu\text{m}$ .

#### 6.4.2 Nanorose Identification by TPL Microscopy in Histological Sections

TPL microscopy was used to identify the presence of nanorose in unstained histological sections (5  $\mu\text{m}$  in thickness) excised from plaque segments in the Positive group. To demonstrate plaque fluorescence and nanorose luminescence simultaneously, TPL images from the two PMTs were recorded separately and merged into a single image. Figure 6.4(a) illustrates a TPL image of plaque measured with emission wavelengths shorter than 570 nm. Figure 6.4 (b) shows nanorose TPL collected through a 700 nm band-pass filter. These two images collected in separate emission wavelengths

were assigned to different channels (plaque: green channel; nanorose: red channel) and merged [Figure 6.4 (c)]. In images presented throughout the remainder of this manuscript, endogenous fluorescence from plaque is green while luminescence from nanorose is red.

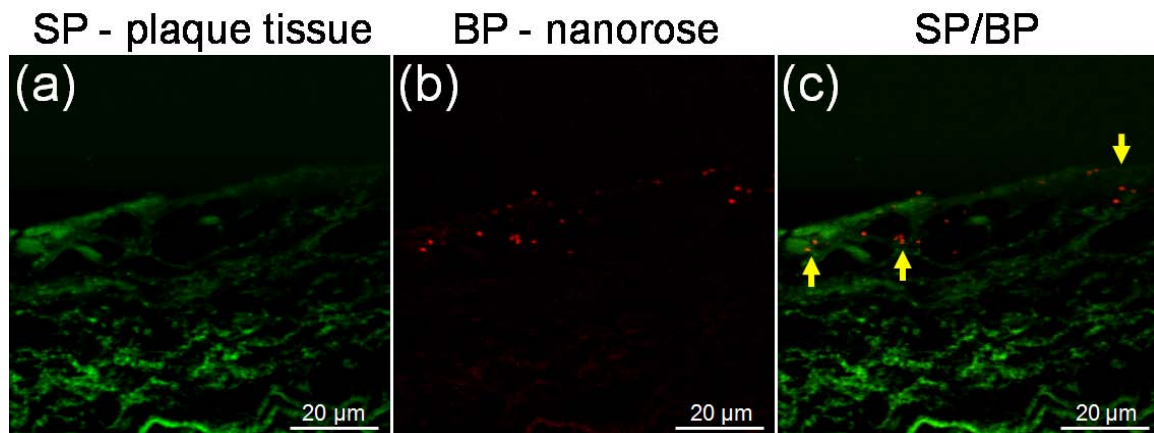


Figure 6.4. Co-registered TPL images of an unstained histological section of plaque from the Positive group. (a) TPL images of plaque measured at emission wavelengths shorter than 570 nm (green). (b) TPL images of nanoroses measured via a 700 nm band-pass filter (red). (c) Merged image of (a) and (b). Yellow arrows in (c) point to nanorose locations. SP: short-pass (<570 nm); BP: band-pass (700/75 nm).

### 6.4.3 PTW Imaging of Superficial Nanoroses and Lipid Deposits in Atherosclerotic Plaques

Plaque segments from Positive and Control groups were irradiated by 800 and 1210 nm laser radiation at a frequency of 4 Hz to generate PTWs from superficial chromophores (nanoroses and lipid deposits that are within 100 μm in depth from plaque surface). Amplitude and phase PTW images at a modulation frequency of 4 Hz were computed (Figure 6.5). Location of stronger light absorption corresponding to nanoroses can be identified in both amplitude and phase PTW images at 800 nm [Figure 6.5(a) and (5e)] and, shapes of plaque lesions and lipid deposits are revealed at 1210 nm [Figure 6.5(b), 5(f), 5(d) and 5(h)]. Phase PTW images not only show locations of nanoroses and lipid deposits, but also reveal depth information as the gray scale assigns darker colors to

smaller phase values [Figure 6.5(e) and 5(h)]. Because amplitude PTW images have better contrast and SNR than phase images, amplitude PTW images were used for further image analysis.

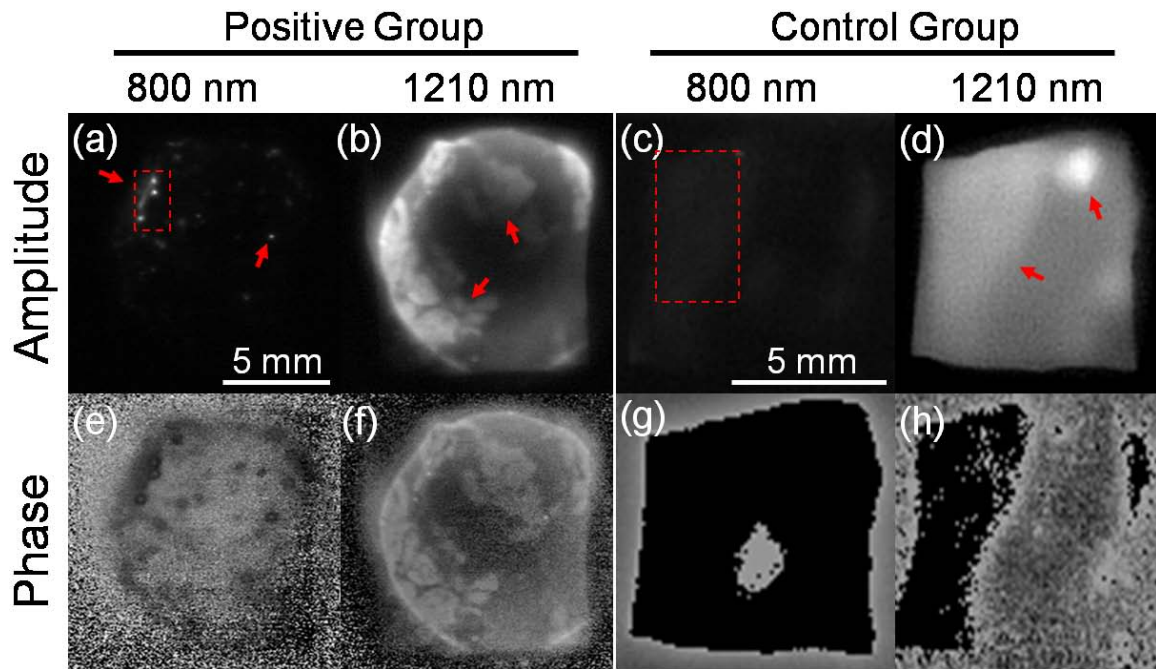


Figure 6.5. Amplitude (a,b,c,d) and phase (e,f,g,h) PTW images of atherosclerotic plaques from Positive and Control groups respectively at 800 and 1210 nm laser irradiation. Laser modulation frequency is 4 Hz. Red arrows point to the position of nanorose in (a) and lipid deposits in (b, d). Red squares indicate regions with and without nanorose in (a) and (c), respectively. Scale bar is the same in (a,b,e,f) and (c,d,g,h), respectively.

Radiometric temperature increase in 44 plaque segments from the Positive group and 30 plaque segments from the Control group were compared to determine the presence of nanorose and to distinguish nanorose from plaque. Figure 6.6(a) shows the average radiometric temperature response from red square areas in Figure 6.5(a) and 6.5(c). The highest radiometric temperature increase and modulation amplitude were observed in regions with nanorose aggregation from the Positive group over the first ten seconds after laser irradiation. In contrast, a much lower radiometric temperature increase

and smaller modulation amplitude were observed in the Control group. Figure 6.6(b) shows the comparison of mean radiometric temperature increase per excitation pulse at regions with (red) and without (blue) nanorose in all plaque segments from Positive and Control groups, respectively. An independent-sample Student's *t* test reveals a significantly higher mean radiometric temperature increase per excitation pulse at nanorose regions in the Positive group compared to the Control group ( $P < 0.001$ ).

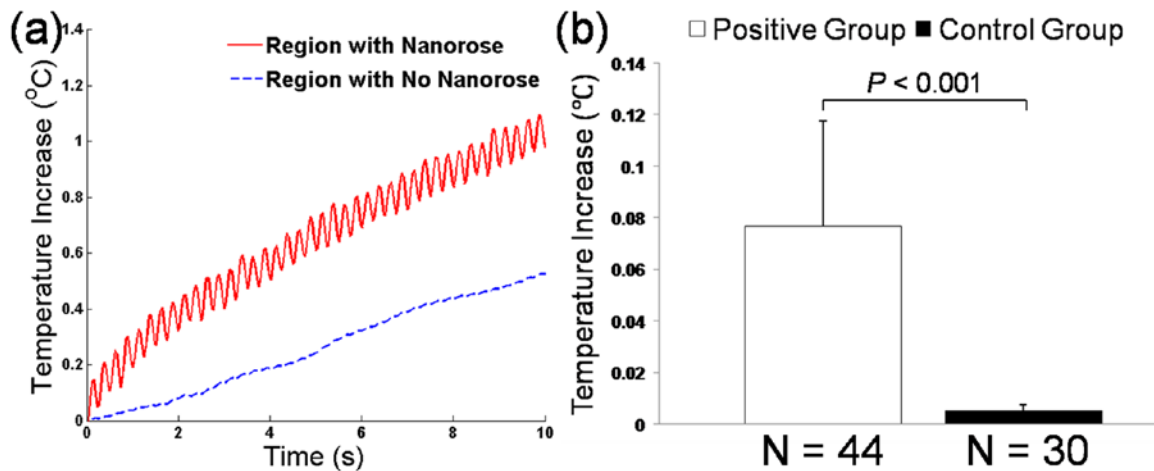


Figure 6.6. (a) Average radiometric temperature increase in response to 800 nm laser irradiation at a modulation frequency of 4 Hz measured from plaque area containing nanorose (bright regions in the red square in Figure 6.5(a)) in the Positive group and area with no nanorose (red square in Figure 6.5(c)) in the Control group. (b) Radiometric temperature increase per pulse at a laser modulation frequency of 4 Hz from all plaque segments in Positive and Control groups, respectively. Data are given as mean $\pm$ SD.

Overlay of 800 and 1210 nm amplitude PTW images from Figure 6.5(a) and 6.5(b) shows the relative spatial distribution of nanorose and lipid deposits [Figure 6.7(a)]. Red regions in Figure 6.7(a) show locations of superficial nanorose aggregates as detected by PTW imaging at 800 nm. Detected regions of nanorose correspond to the edges of superficial lipid deposits. Nanorose is not present at all lipid edges but at discrete locations (e.g., 1B,1C,2A,3B,3C) in Figure 6.7(a). The blue dashed line in region 2A in the overlay image [Figure 6.7(a)] shows an accumulation of nanoroses, consistent with

the histological section from the same region where a dense accumulation of macrophages is identified by RAM-11 stain [Figure 6.7(b)]. In contrast, macrophages are not observed [Figure 6.7(c)] in regions with no PTW signals from nanorose (yellow dashed line in Figure 6.7(a)).

Merged TPL images from an unstained histological section adjacent to the section in Figure 6.7(b) are shown in Figure 6.7(e)-6.7(g) with increased magnification. Strong TPL signals from nanorose are observed (red color pointed by yellow arrows in Figure 6.7(g)). Endogenous plaque fluorescence, which may originate from elastin fibers and collagen [28,30,32], is also observed in the plaque (green color in Figure 6.7(e)-6.7(j)). Nanoroses identified by TPL microscopy co-localize with superficial macrophages [Figure 6.7(g)], indicating that PTW signals at 800 nm laser irradiation are generated by nanorose-loaded macrophages. The size of nanorose aggregations in macrophages varies from less than 1  $\mu\text{m}$  to about 10  $\mu\text{m}$  [Figure 6.7(g)], suggesting that the concentration of engulfed nanoroses in macrophages is variable. Although macrophages are observed as deep as 200  $\mu\text{m}$  from the plaque surface [Figure 6.7(b)], nanorose distribution is restricted within the first 20  $\mu\text{m}$  [Figure 6.7(g)]. This observation may suggest that the nanorose-loaded macrophages mostly reside in the very superficial regions of intima and have not migrated to deeper locations up to three days after intravenous nanorose injection. In a region of the same plaque segment from the Positive group where no PTW signals from nanorose are detected [Figure 6.7(c)], only endogenous plaque fluorescence from elastin fibers is observed [Figure 6.7(h)-6.7(j)]. A histological section of plaque from the Control group with a dense accumulation of macrophages [Figure 6.7(d)] was also imaged by

TPL microscopy [Figure 6.7(k)-6.7(m)]. Fluorescence from elastin fibers is detected. Moreover, macrophage-like cellular structures with dark nuclei (indicated by a yellow circle) and possibly lipid droplets in or outside macrophages (pointed by yellow arrow heads) are observed in Figure 6.7(m) [33-34].

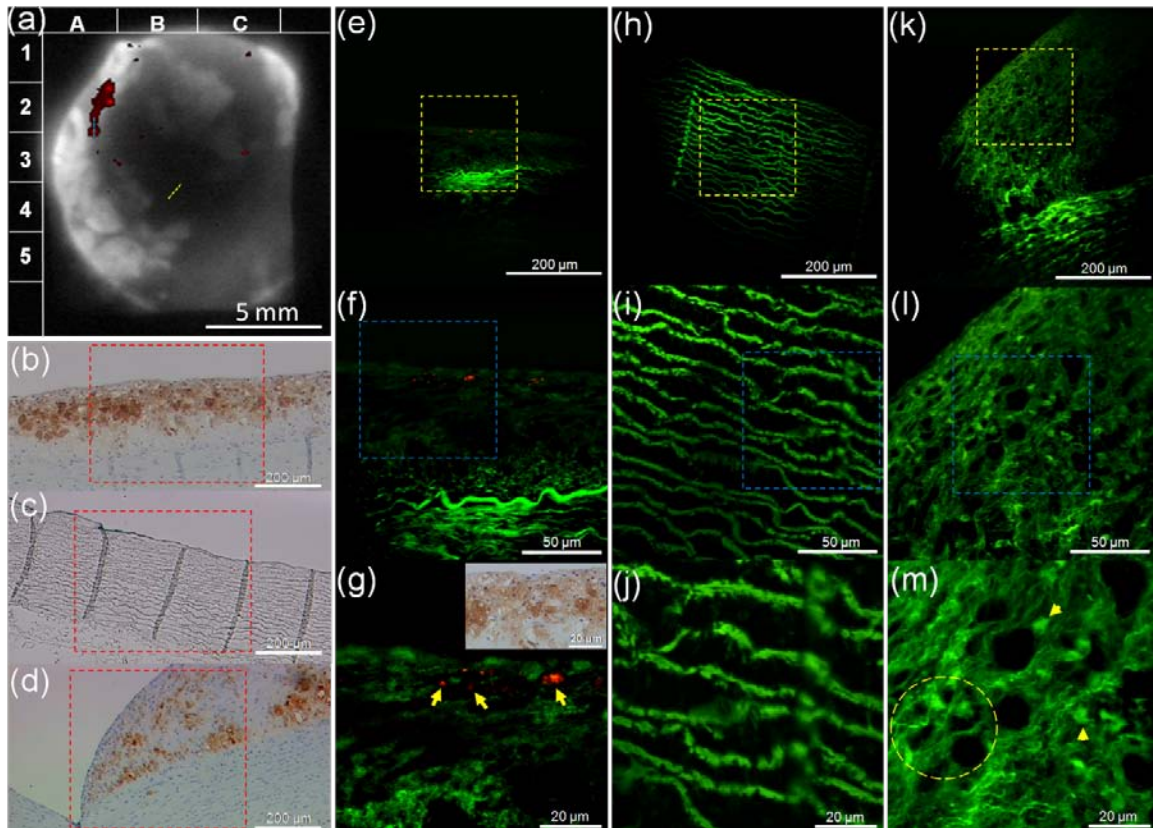


Figure 6.7. (a) Overlay of amplitude PTW images from Figure 6.5(a) and 5(b). Red color indicates nanorose. (b,c) Histological sections of plaque from the Positive group with RAM-11 stain along blue and yellow dashed lines in regions 2A and 4B respectively in (a). (d) Histological section of plaque from the Control group with RAM-11 stain. Brown color in (b) and (d) indicates macrophages. (e,f,g), (h,i,j), (k,l,m) Merged TPL images of unstained histological section adjacent to the section in (b), (c) and (d), respectively. Red square region in (b), (c) and (d) corresponds to (e), (h) and (k), respectively. Yellow square region in (e), (h) and (k) corresponds to (f), (i) and (l), respectively. Blue square region in (f), (i) and (l) corresponds to (g), (j) and (m), respectively. Inset in (g) shows co-localized RAM-11 stain of (g) magnified from (b). Yellow arrows in (g) point to nanorose locations. Yellow arrow heads in (m) point to lipid droplets. Yellow circle in (m) indicates clusters of macrophages.

#### 6.4.4 Multi-Frequency PTW Imaging in Combination with OCT

Detection of chromophores located deeper in the tissue using PTW imaging requires reduced laser modulation frequencies. Therefore, laser modulation frequencies of 0.1 and 1 Hz were applied to visualize deeper nanorose-loaded macrophages and lipid deposits (600 and 200  $\mu\text{m}$  thermal diffusion lengths in response to 0.1 and 1 Hz laser modulation frequencies, respectively). In Figure 6.8, amplitude PTW images at three modulation frequencies are shown. At 800 nm laser irradiation, nanoroses produce the strongest PTW signals at 4 Hz [Figure 6.8(c)], much weaker at 1 Hz [Figure 6.8(b)] and negligible signal contrast at 0.1 Hz [Figure 6.8(a)], suggesting that nanorose-loaded macrophages are primarily superficially distributed in the plaque (i.e.,  $< 100 \mu\text{m}$ ), consistent with merged TPL microscopy images (red color in Figure 6.8(i)-6.8(k)).

At 1210 nm laser irradiation, lipid deposits produce strong PTW signals at all three frequencies, denoted by black arrows in Figure 6.8(d)-6.8(f). This observation indicates that lipid deposits distribute over multiple depths in the plaque. The bright region where the arrow points in Figure 6.8(d) reveals the location of a lipid core in the plaque. Amplitude PTW images at lower modulation frequencies [Figure 6.8(a), 6.8(b), 6.8(d) and 6.8(e)] appear more blurred than images at higher frequency [Figure 6.8(c) and 6.8(f)] due to greater lateral heat diffusion in the plaque.

Amplitude PTW images at a modulation frequency of 4 Hz [Figure 6.8(c) and 6.8(f)] were merged into a co-registered OCT image [Figure 6.8(g)]. The merged PTW-OCT image shows a topographic surface structure of the plaque. Peak (P) and valley (V) regions are observed. The blue dashed line in the merged PTW-OCT image shows an

accumulation of nanoroses, consistent with the histological section from the same region where a dense accumulation of macrophages is identified [Figure 6.8(h)]. Merged TPL images from an unstained histological section adjacent to the section in Figure 6.8(h) are shown in Figure 6.8(i)-6.8(k). Strong TPL signals from nanorose are observed within 20  $\mu\text{m}$  from plaque surface [Figure 6.8(k)] and endogenous plaque fluorescence from elastin fibers and lipid droplets is also observed [Figure 6.8(j)]. Interestingly, Figure 6.8(g) shows that superficial lipid deposits are surrounded by nanorose-loaded macrophages located close to the shoulders of the plaque. The relative distribution of nanorose-loaded macrophages to lipid deposits is consistent with that in Figure 6.7(a) and observed repeatedly in other plaques (19 of 44 plaque segments (43%) in the Positive group). Of note is that the direction of blood flow in the live animal is from top to bottom in the image as depicted by red arrows above Figure 6.8(g).

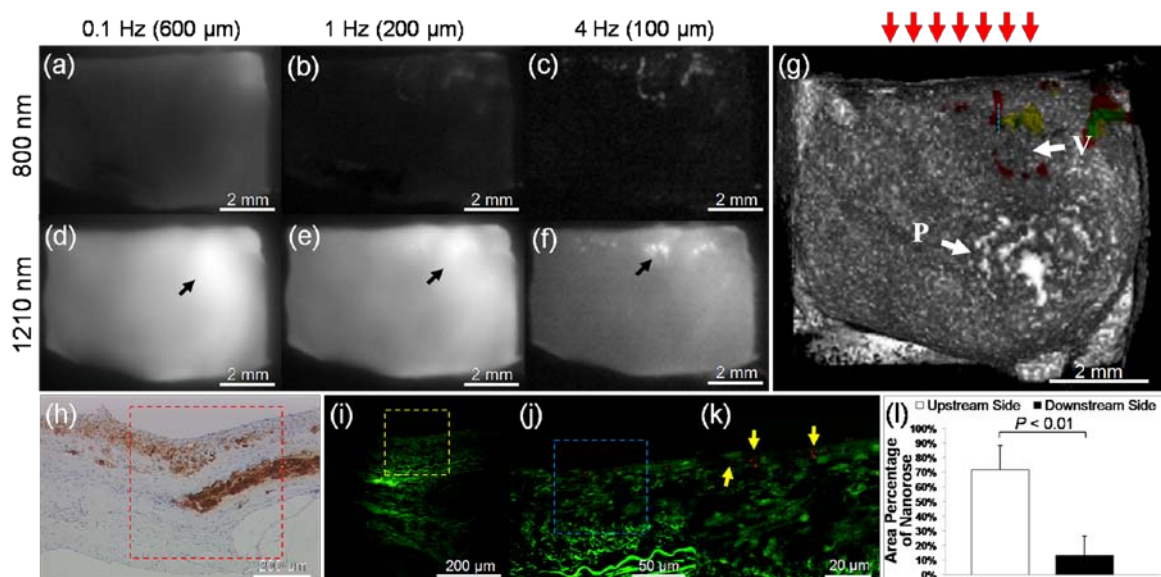




Figure 6.8. (a,b,c,d,e,f) Amplitude PTW images of a plaque segment from the Positive group at 800 and 1210 nm laser irradiation, respectively. Laser modulation frequencies are respectively 0.1, 1 and 4 Hz with corresponding thermal diffusion lengths of 600, 200 and 100  $\mu\text{m}$ . Black arrows point to lipid deposits in (d), (e) and (f). (g) Co-registered and merged PTW-OCT image (Video 1, MPEG, 2.5 MB). Red, yellow, and green colors in (g) represent respectively nanorose-loaded macrophages, lipid deposits and both. White arrows point to peak (P) and valley (V) regions of the plaque in (g). Red arrows above (g) indicate direction of blood flow. (h) Histological section with RAM-11 stain along blue dashed line in (g). (i,j,k) Merged TPL images of unstained histological section adjacent to the section in (h). (i), (j) and (k) respectively represents red, yellow and blue square region in (h), (i) and (j). (l) Area percentage of nanorose at shoulders on the upstream versus downstream side of the plaques (N=44) from the Positive group. Larger area percentage of nanorose are observed at plaque shoulders on the upstream side ( $P < 0.01$ ). Yellow arrows in (k) point to nanorose locations.

## 6.5 DISCUSSION

The presently employed imaging contrast agent, nanorose, represents a novel gold nanoparticle that is taken up by macrophages. Many investigators have noted that particle size is an important factor in cellular uptake of gold nanoparticles. Chithrani *et al* observed that gold nanoparticle endocytosis by Hela cells is strongly size-dependent with higher uptake rates for particle sizes between 30 and 60 nm [35]. Recently, Jiang *et al* showed that the internalization of Herceptin-gold nanoparticles by human breast cancer cells was most efficient at 25-50 nm size range [36]. Furthermore, larger nanoparticles tend to have a short blood half-life and are quickly removed from circulation by liver and spleen [37]. In contrast, smaller nanoparticles have a longer blood residence time giving greater chance of being taken up by circulating blood-based monocytes and plaque-based macrophages [38]. Therefore, nanorose with a 30 nm particle size and non-ionic dextran coating is potentially effective to increase macrophage uptake and decrease opsonization and subsequent removal by liver and spleen. In this study, a 3-day interval between nanorose injection and PTW-OCT imaging was used to ensure nanorose uptake by macrophages. However, this time interval may not be clinically optimal. Interestingly,

magnetic susceptibility artifacts (MSAs) induced by the injected ferumoxtran-10 (one type of ultrasmall superparamagnetic nanoparticles of iron oxide) have been detected optimally in the carotid arteries of patients 24 to 48 hours after the injection while almost no signal contrast was observed at 72 hours [39], suggesting that shorter time intervals may be considered in future studies.

In this study, the majority of nanoroses observed were found to be superficial and localized at the shoulders of plaques, especially on the upstream side of lesions, suggesting that macrophages which had engulfed the nanorose were co-localized at these regions. A paired-sample Student's *t* test reveals a significantly larger area percentage of nanorose at shoulders on the upstream compared to the downstream side ( $P < 0.01$ ) of the plaques [Figure 6.8(1)]. This finding is consistent with a previous study by Dirksen *et al* who showed that 67% of the 33 human carotid plaques collected contained more macrophages in upstream shoulder regions where higher flow rate and higher shear stress prevails [40]. Recently, a review by Slager *et al* confirmed that macrophages predominate on the upstream side of the plaque induced by high shear stress [41]. In fact, increased expression of MMPs by macrophages in plaques appears to be restricted to shoulder regions of plaques [42-45]. Moreover, rupture of atherosclerotic plaques has been reported to occur predominantly at macrophage-rich shoulders of the plaque's fibrous cap [40,46-48]. Therefore, the observation of high density of nanorose, engulfed by macrophages, at plaque shoulders on the upstream side in our study demonstrates that a combined PTW-OCT imaging approach with nanorose as a contrast agent has predictive value for plaque vulnerability.

Most nanoroses detected by TPL microscopy were superficial, within 20  $\mu\text{m}$  from plaque surface. However, RAM-11 stained macrophages were distributed as deep as 200  $\mu\text{m}$ . This observation suggests that only superficial macrophages in the plaque took up

nanorose. Macrophages that already migrate into deeper locations may not be able to take up nanorose either because nanorose cannot penetrate deeply into the intima or probability of nanorose's delivery through the vasa vasorum is low or does not occur. Moreover, apoptotic and necrotic macrophages contribute to lipid core formation in plaques [49], and these macrophage debris could stain RAM-11 positive but are not intact and are unable to take up free nanorose *in situ*.

Although nanorose uptake by macrophages has been identified in our cell culture study (Figure 6.3), their transport pathway to plaque-based macrophages is not clear. Previous studies have proposed three mechanisms for transport of superparamagnetic nanoparticles to arterial tissue [50-53]: 1) nanoparticles are endocytosed by activated blood monocytes which migrate through the lumen into the intimal surface; 2) transcytosis of nanoparticles across the endothelium and into the intima followed by uptake by *in situ* macrophages; and 3) diffusion of individual nanoparticles into the adventitia via the vasa vasorum. Our PTW imaging (at 0.1 Hz laser modulation) and TPL microscopy results of a plaque segment [Figure 6.8(a)] and histological section [Figure 6.8(i)], respectively, show that nanorose is not detected at deeper plaque locations (e.g., 100-600  $\mu\text{m}$ ), suggesting that nanorose transport via the vasa vasorum may not have occurred in our study. Interestingly, TPL images of a histological section of plaque from the Positive group show a "snapshot" of a nanorose-loaded monocyte-like cell entering the plaque surface (Figure 6.9). Sparsely distributed nanoroses are visible inside the cell. This image suggests that nanoroses can be first endocytosed by monocytes in the blood stream and then enter the plaques through the lumen. Further study, however, is needed to determine the relative contributions of these proposed mechanisms to enhance the clinical value of PTW-OCT imaging.

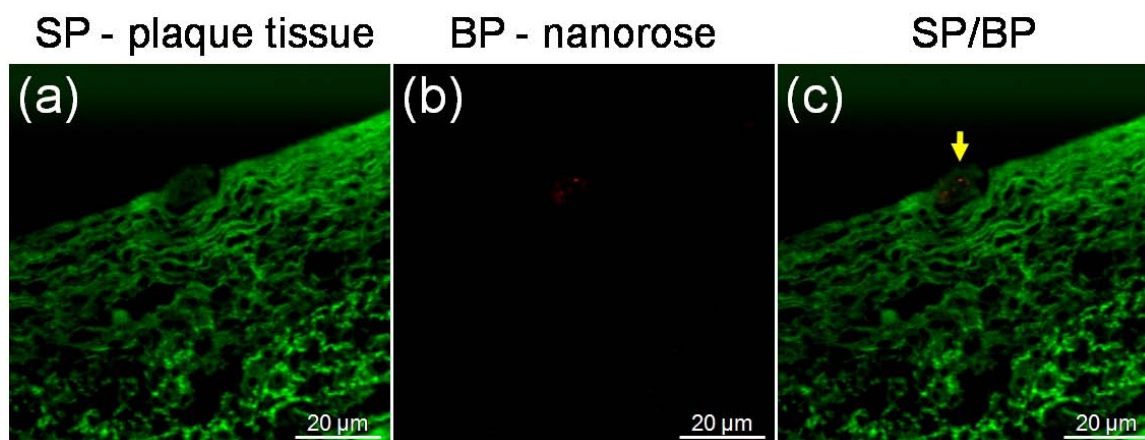


Figure 6.9. Co-registered TPL images of a nanorose-loaded monocyte-like cell entering the plaque surface from an unstained histological slice of plaque from the Positive group. (a) TPL images of plaque measured at emission wavelengths shorter than 570 nm (green). (b) TPL images of nanoroses measured via a 700 nm band-pass filter (red). (c) Merged image of (a) and (b). Yellow arrow in (c) points to nanorose location. SP: short-pass (<570 nm); BP: band-pass (700/75 nm).

We demonstrate for the first time that dual-wavelength multi-frequency PTW imaging can be used to detect and distinguish plaque components. With excitation wavelengths that match high absorption spectral regions of different chromophores in atherosclerotic plaques, PTW imaging provides contrast for nanorose-loaded macrophages and lipid deposits. Moreover, axial distribution of nanorose-loaded macrophages and lipid deposits can be determined at selected laser modulation frequencies, giving additional diagnostic information of atherosclerotic plaques such as macrophage infiltration depth and lipid core location. Although OCT shows tomographic plaque surface structure and is able to resolve fibrous caps (usually less than 65 μm in thickness), this imaging method alone does not provide specificity for macrophages and lipid deposits due to lack of scattering contrast among different plaque components. Merged tomographic PTW-OCT images can simultaneously reveal plaque composition with respect to plaque surface structure, which substantially enhances the capability of OCT in the study of characterizing plaque components and allows observation of known

biological phenomena (e.g., macrophages distributed at shoulders on the upstream side of atherosclerotic plaques). From a clinical perspective, imaging macrophages and lipid deposits in the context of plaque surface structure offers the ability to identify plaque regions more prone to rupture. Currently, our study utilized *ex vivo* tissues and the clinical translation of combined PTW-OCT imaging would face many implementation challenges. Beard *et al* demonstrated an optical fiber photoacoustic-photothermal probe [54] which has the potential to perform intravascular PTW imaging. Recently, photothermal OCT systems [25,55-57] have been reported to record optical pathlength variation due to thermal-elastic and thermorefractive changes induced by absorption of incident radiation. Both candidate approaches require engineering development to incorporate into an intravascular catheter. The motivation for future development of intravascular PTW imaging in combination with an OCT catheter [58-59] during heart catheterization to detect nanorose-loaded macrophages and lipid deposits in plaques *in vivo* appears promising. Intravascular PTW-OCT imaging using nanorose as a contrast agent could allow clinical studies that monitor nanorose-loaded macrophages in response to various therapeutic interventions *in vivo*. Such an imaging tool would be of value to determine macrophage and lipid density over time rather than the current standard of autopsy studies that provide a single time point measurement.

## 6.6 CONCLUSION

By utilizing PTW imaging in response to 800 and 1210 nm laser irradiation we demonstrated detection of PTW signals from nanorose and lipid deposits in atherosclerotic plaques. Moreover, multi-frequency (0.1, 1 and 4 Hz) PTW imaging can be used to distinguish nanorose and lipid deposits distributed at different depths. Nanorose presence was also identified with TPL microscopy in histological sections. Co-

localization of nanorose shown in TPL microscopy with RAM-11 stained macrophages suggests that PTW signals at 800 nm laser irradiation is generated by superficial nanorose-loaded macrophages. Amplitude PTW images (800 and 1210 nm) at a modulation frequency of 4 Hz merged with a co-registered OCT image demonstrated the location and distribution of superficial nanorose-loaded macrophages and lipid deposits with respect to plaque surface structure and direction of blood flow. Our results suggest that nanorose-loaded macrophages are distributed at plaque shoulders on the upstream side, at edges of lipid deposits, and superficially located (within 20  $\mu\text{m}$  from plaque surface). This *ex vivo* animal study suggests that combined PTW-OCT imaging is a promising imaging approach for multi-depth screening of nanorose-loaded macrophages and lipid deposits in atherosclerotic plaques.

## **6.7 ACKNOWLEDGEMENTS**

The authors would like to acknowledge the technical support from the University of Texas Health Science Center at San Antonio. This work was supported by a Veterans Administration merit grant to Feldman, a Welch Foundation grant F-1319 and NSF grant CBET-0968038 to Johnston, and the Department of Energy Center for Frontiers of Subsurface Energy Security.

## **6.8 REFERENCES**

- [1] Yusuf S, Reddy S, Ounpuu S, Anand S, "Global burden of cardiovascular diseases: part I: general considerations, the epidemiologic transition, risk factors, and impact of urbanization," *Circulation* 104, 2746-2753 (2001)
- [2] Falk E, Shah PK, Fuster V, "Coronary plaque disruption," *Circulation* 92(3), 657-671 (1995)

- [3] Kolodgie FD, Virmani R, Burke AP, Farb A, Weber DK, Kutys R, Finn AV, Gold HK, "Pathologic assessment of the vulnerable human coronary plaque," *Heart* 90, 1385-1391 (2004)
- [4] Davies MJ, Thomas A, "Thrombosis and acute coronary-artery lesions in sudden cardiac ischemic death," *N Engl J Med* 310, 1137-1140 (1984)
- [5] Falk E, "Pathogenesis of atherosclerosis," *J Am Coll Cardiol* 47(8 Suppl), C7-C12 (2006)
- [6] Sanz J, Fayad ZA, "Imaging of atherosclerotic cardiovascular disease," *Nature* 451(7181), 953-957 (2008)
- [7] Brezinski ME, Tearney GJ, Bouma BE, Boppart SA, Hee MR, Swanson EA, Southern JF, Fujimoto JG, "Imaging of coronary artery microstructure (in vitro) with optical coherence tomography," *Am J Cardiol* 77, 92-93 (1996)
- [8] Raffel OC, Tearney GJ, Gauthier DD, Halpern EF, Bouma BE, Jang IK, "Relationship between a systemic inflammatory markers, plaque inflammation, and plaque characteristics determined by intravascular optical coherence tomography," *Arterioscler Thromb Vasc Biol* 27, 1820-1827 (2007)
- [9] Tanaka A, Imanishi T, Kitabata H, Kubo T, Takarada S, Tanimoto T, Kuroi A, Tsujioka H, Ikejima H, Ueno S, Kataiwa H, Okouchi K, Kashiwagi M, Matsumoto H, Takemoto K, Nakamura N, Hirata K, Mizukoshi M, Akasaka T, "Morphology of exertion-triggered plaque rupture in patients with acute coronary syndrome: an optical coherence tomography study," *Circulation* 118, 2368-2373 (2008)
- [10] Vancraeynest D, Pasquet A, Roelants V, Gerber BL, Vanoverschelde JJ, "Imaging the vulnerable plaque," *J Am Coll Cardiol* 57, 1961-1979 (2011)
- [11] Tearney GJ, Yabushita H, Houser SL, Aretz HT, Jang I, Schendorff KH, Kauffman CR, Shishkov M, Halpern EF, Bouma BE, "Quantification of macrophage content in

- atherosclerotic plaques by optical coherence tomography," *Circulation* 107, 113-119 (2003)
- [12] Liu L, Gardecki JA, Nadkarni SK, Toussaint JD, Yagi Y, Bouma BE, Tearney GJ, "Imaging the subcellular structure of human coronary atherosclerosis using micro-optical coherence tomography," *Nat Med* 17(8), 1010-1014 (2011)
- [13] Rosencwaig A, "Thermal-wave imaging," *Science* 218(4569), 223-228 (1982)
- [14] Thomas RL, Favro LD, Kuo PK, "Thermal-wave imaging for nondestructive evaluation," *Can J Phys* 64, 1234-1237 (1986)
- [15] Mandelis A, Williams A, Siu EKM, "Photothermal wave imaging of metal-oxide-semiconductor field-effect transistor structures," *J Appl Phys* 63(1), 92-98 (1988)
- [16] Telenkov SA, Vargas G, Nelson JS, Milner TE, "Coherent thermal wave imaging of subsurface chromophores in biological materials," *Phys Med Biol* 47, 657-671 (2002)
- [17] Busse G, Dewhurst RJ, Nikoonahad M, Scruby CB, "Imaging with optically generated thermal waves," *Phil Trans R Soc Lond A* 320, 181-186 (1986)
- [18] Ma LL, Feldman MD, Tam JM, Paranjape AS, Cheruku KK, Larson TA, Tam JO, Ingram DR, Paramita V, Villard JW, Jenkins JT, Wang T, Clarke GD, Asmis R, Sokolov K, Chandrasekar B, Milner TE, Johnston KP, "Small multifunctional nanoclusters (nanoroses) for targeted cellular imaging and therapy," *ACS Nano* 3(9), 2686-2696 (2009)
- [19] Mornet S, Vasseur S, Grasset F, Duguet E, "Magnetic nanoparticle design for medical diagnosis and therapy," *J Mat Chem* 14, 2161-2175 (2004)
- [20] Jacques S, Optical properties spectra, Available at: <http://omlc.ogi.edu/spectra>
- [21] Anderson RR, Farinelli W, Laubach H, Manstein D, Yaroslavsky AN, Gubeli III J, Jordan K, Neil GR, Shinn M, Chandler W, Williams GP, Benson SV, Douglas DR,



- Dylla HF, "Selective photothermolysis of lipid-rich tissues: A free electron laser study," *Lasers Surg Med* 38(10), 913-919 (2006)
- [22] Tsai CL, Chen JC, Wang WJ, "Near-infrared absorption property of biological soft tissue constituents," *J Med Biol Eng* 21, 7-14 (2001)
- [23] Walsh Jr JT, (1995), "Pulsed laser angioplasty: a paradigm for tissue ablation in optical-thermal response of laser-irradiated tissue," Welch AJ, van Gemert MJC (Eds), 869-874, New York: Plenum Press
- [24] Kolodgie FD, Katocs AS Jr, Largis EE, Wrenn SM, Cornhill JF, Herderick EE, Lee SJ, Virmani R, "Hypercholesterolemia in the rabbit induced by feeding graded amounts of low-level cholesterol: Methodological considerations regarding individual variability in response to dietary cholesterol and development of lesion type," *Arterioscler Thromb Vasc Biol* 16(12), 1454-1464 (1996)
- [25] Paranjape AS, Kuranov R, Baranov S, Ma LL, Villard JW, Wang T, Sokolov KV, Feldman MD, Johnston KP, Milner TE, "Depth resolved photothermal OCT detection of macrophages in tissue using nanorose," *Biomed Opt Exp* 1(1), 2-16 (2010)
- [26] Shaw III CF, "Gold-based therapeutic agents," *Chem Rev* 99, 2589-2600 (1999)
- [27] Park J, Estrada A, Sharp K, Sang K, Schwartz JA, Smith DK, Coleman C, Payne JD, Korgel BA, Dunn AK, Tunnell JW, "Two-photon-induced photoluminescence imaging of tumors using near-infrared excited gold nanoshells," *Opt Exp* 16(3), 1590-1599 (2008)
- [28] Lilledahl MB, Haugen OA, de Lange Davies C, Svaasand LO, "Characterization of vulnerable plaques by multiphoton microscopy," *J Biomed Opt* 12(4), 0440051-04400512 (2007)

- [29] Le TT, Langohr IM, Locker MJ, Sturek M, Cheng JX, "Label-free molecular imaging of atherosclerotic lesions using multimodal nonlinear optical microscopy," *J Biomed Opt* 12(5), 0540071-05400710 (2007)
- [30] Yu W, Braz JC, Dutton AM, Prusakov P, Rekhter M, "In vivo imaging of atherosclerotic plaques in apolipoprotein E deficient mice using nonlinear microscopy," *J Biomed Opt* 12(5), 0540081-05400810 (2007)
- [31] Leibovich SJ, Polverini PJ, Shepard HM, Wiseman DM, Shively V, Nuseir N, "Macrophage-induced angiogenesis is mediated by tumor necrosis factor-alpha," *Nature* 329, 630-632 (1987)
- [32] van Zandvoort M, Engels W, Douma K, Beckers L, Oude Egbrink M, Daemen M, Slaaf DW, "Two-photon microscopy for imaging of the (atherosclerotic) vascular wall: a proof of concept study," *J Vasc Res* 41, 54-63 (2004)
- [33] Lim RS, Kratzer A, Barry NP, Miyazaki-Anzai S, Miyazaki M, Mantulin WW, Levi M, Potma EO, Tromberg BJ, "Multimodal CARS microscopy determination of the impact of diet on macrophage infiltration and lipid accumulation on plaque formation in ApoE-deficient mice," *J Lipid Res* 51, 1729-1737 (2010)
- [34] Wang HW, Langohr IM, Sturek M, Cheng JX, "Imaging and quantitative analysis of atherosclerotic lesions by CARS-based multimodal nonlinear optical microscopy," *Arterioscler Thromb Vasc Biol* 29, 1342-1348 (2009)
- [35] Chithrani BD, Ghazani AA, Chan WC, "Determining the size and shape dependence of gold nanoparticle uptake into mammalian cells," *Nano Lett* 6, 662-668 (2006)
- [36] Jiang W, Kim BY, Rutka JT, Chan WC, "Nanoparticle-mediated cellular response is size-dependent," *Nat Nanotech* 3, 145-150 (2008)
- [37] Owens DE III, Peppas NA, "Opsonization, biodistribution, and pharmacokinetics of polymeric nanoparticles," *Int J Pharmaceu* 307, 93-102 (2006)

- [38] Wenger Y, Schneider RJ 2nd, Reddy GR, Kopelman R, Jolliet O, Philbert MA, "Tissue distribution and pharmacokinetics of stable polyacrylamide nanoparticles following intravenous injection in the rat," *Toxicol Appl Pharmacol* 251, 181-190 (2011)
- [39] Trivedi RA, U-King-Im JM, Graves MJ, Cross JJ, Horsley J, Goddard MJ, Skepper JN, Quartey G, Warburton E, Joubert I, Wang L, Kirkpatrick PJ, Brown J, Gillard JH, "In vivo detection of macrophages in human carotid atheroma: temporal dependence of ultrasmall superparamagnetic particles of iron oxide-enhanced MRI," *Stroke* 35, 1631-1635 (2004)
- [40] Dirksen MT, van der Wal AC, van den Berg FM, van der Loos CM, Becker AE, "Distribution of inflammatory cells in atherosclerotic plaques relates to the direction of flow," *Circulation* 98(19), 2000-2003 (1998)
- [41] Slager CJ, Wentzel JJ, Gijzen FJ, Thury A, van der Wal AC, Schaar JA, Serruys PW, "The role of shear stress in the destabilization of vulnerable plaques and related therapeutic implications," *Nat Rev Cardiol* 2, 456-464 (2005)
- [42] Nikkari ST, O'Brien KD, Ferguson M, Hatsukami T, Welgus HG, Alpers CE, Clowes AW, "Interstitial collagenase (MMP-1) expression in human carotid atherosclerosis," *Circulation* 92, 1393-1398 (1995)
- [43] Henney AM, Wakeley PR, Davies MJ, Foster K, Hembry R, Murphy G, Humphries S, "Localization of stromelysin gene expression in atherosclerotic plaques by in situ hybridization," *Proc Natl Acad Sci* 88, 8154-8158 (1991)
- [44] Halpert I, Sires UI, Roby JD, Potter-Perigo S, Wight TN, Shapiro SD, Welgus HG, Wickline SA, Parks WC, "Matrilysin is expressed by lipid-laden macrophages at sites of potential rupture in atherosclerotic lesions and localizes to areas of versican

- deposition, a proteoglycan substrate for the enzyme," *Proc Natl Acad Sci* 93, 9748-9753 (1996)
- [45] Uzui H, Harpf A, Liu M, Doherty TM, Shukla A, Chai NN, Tripathi PV, Jovinge S, Wilkin DJ, Asotra K, Shah PK, Rajavashisth TB, "Increased expression of membrane type 3-matrix metalloproteinase in human atherosclerotic plaque: role of activated macrophages and inflammatory cytokines," *Circulation* 106, 3024-3030 (2002)
- [46] Rajagopalan S, Meng XP, Ramasamy S, Harrison DG, Galis ZS, "Reactive oxygen species produced by macrophage-derived foam cells regulate the activity of vascular matrix metalloproteinases in vitro. Implications for atherosclerotic plaque stability," *J Clin Invest* 98(11), 2572-2579 (1996)
- [47] Kovanen PT, Kaartinen M, Paavonen T, "Infiltrates of activated mast cells at the site of coronary atheromatous erosion or rupture in myocardial infarction," *Circulation* 92, 1084-1088 (1995)
- [48] Schieffer B, Schieffer E, Hilfiker-Kleiner D, Hilfiker A, Kovanen PT, Kaartinen M, Nussberger J, Harringer W, Drexler H, "Expression of angiotensin ii and interleukin 6 in human coronary atherosclerotic plaques: potential implications for inflammation and plaque instability," *Circulation* 101, 1372-1378 (2000)
- [49] Tabas I, "Macrophage apoptosis in atherosclerosis: consequences on plaque progression and the role of endoplasmic reticulum stress," *Antioxid Redox Signal* 11(9), 2333-2339 (2009)
- [50] Corot C, Petry KG, Trivedi R, Saleh A, Jonkmanns C, Le Bas JF, Blezer E, Rausch M, Brochet B, Foster-Gareau P, Balériaux D, Gaillard S, Dousset V, "Macrophage imaging in central nervous system and in carotid atherosclerotic plaque imaging

- using ultrasmall superparamagnetic iron oxide in magnetic resonance imaging," *Invest Radiol* 39, 619-625 (2004)
- [51] Dousset V, Delalande C, Ballarino L, Quesson B, Seilhan D, Coussemaçq M, Thiaudière E, Brochet B, Canioni P, Caillé JM, "In vivo macrophage activity imaging in the central nervous system detected by magnetic resonance," *Magn Reson Med* 41, 329-333 (1999)
- [52] Rausch M, Hiestand P, Baumann D, Cannet C, Rudin M, "MRI-based monitoring of inflammation and tissue damage in acute and chronic relapsing EAE," *Magn Reson Med* 50, 309-314 (2003)
- [53] Corot C, Robert P, Idée JM, Port M, "Recent advances in iron oxide nanocrystal technology for medical imaging," *Adv Drug Deliv Rev* 58, 1471-1504 (2006)
- [54] Beard PC, Pérennès F, Draguioti E, Mills TN, "Optical fiber photoacoustic-photothermal probe," *Opt Lett* 23(15), 1235-1237 (1998)
- [55] Adler DC, Huang SW, Huber R, Fujimoto JG, "Photothermal detection of gold nanoparticles using phase-sensitive optical coherence tomography," *Opt Exp* 16(7), 4376-4393 (2008)
- [56] Skala MC, Crow MJ, Wax A, Izatt JA, "Photothermal optical coherence tomography of epidermal growth factor receptor in live cells using immunotargeted gold nanospheres," *Nano Lett* 8(10), 3461-3467 (2008)
- [57] Zhou C, Tsai TH, Adler DC, Lee HC, Cohen DW, Mondelblatt A, Wang Y, Connolly JL, Fujimoto JG, "Photothermal optical coherence tomography in ex vivo human breast tissues using gold nanoshells," *Opt Lett* 35(5), 700-702 (2010)
- [58] Bouma BE, Tearney GJ, Yabushita H, Shishkov M, Kauffman CR, DeJoseph Gauthier D, MacNeill BD, Houser SL, Aretz HT, Halpern EF, Jang IK, "Evaluation

of intracoronary stenting by intravascular optical coherence tomography," *Heart* 89, 317-320 (2003)

[59] Yabushita H, Bouma BE, Houser SL, Aretz HT, Jang IK, Schlendorf KH, Kauffman CR, Shishkov M, Kang DH, Halpern EF, Tearney GJ, "Characterization of human atherosclerosis by optical coherence tomography," *Circulation* 106, 1640-1645 (2002)

## Chapter 7 Two-photon Luminescence (TPL) Microscopy Combined with OCT for Macrophage Detection in the Hypercholesterolemic Rabbit Aorta Using Gold Nanoparticles<sup>5</sup>

### 7.1 ABSTRACT

The macrophage is an important early cellular marker related to risk of future rupture of atherosclerotic plaques. Two-channel two-photon luminescence (TPL) microscopy combined with optical coherence tomography (OCT) was used to detect, and further characterize the distribution of aorta-based macrophages using plasmonic gold nanorose as an imaging contrast agent. Nanorose uptake by macrophages was identified by TPL microscopy in macrophage cell culture. *Ex vivo* aorta segments (8×8×2 mm<sup>3</sup>) rich in macrophages from a rabbit model of aorta inflammation were imaged by TPL microscopy in combination with OCT. Aorta histological sections (5 μm in thickness) were also imaged by TPL microscopy. Merged two-channel TPL images showed the lateral and depth distribution of nanorose-loaded macrophages (confirmed by RAM-11 stain) and other aorta components (e.g., elastin fiber and lipid droplet), suggesting that nanorose-loaded macrophages are diffusively distributed and mostly detected superficially within 20 μm from the luminal surface of the aorta. Moreover, OCT images depicted detailed surface structure of the diseased aorta. Results suggest that TPL microscopy combined with OCT can simultaneously reveal macrophage distribution with respect to aorta surface structure, which has the potential to detect vulnerable plaques and monitor plaque-based macrophages overtime during cardiovascular interventions.

---

<sup>5</sup> Significant portions of this chapter have been previously published in *Lasers Surg Med* 44(1), 49-59 (2012).

## 7.2 INTRODUCTION

Atherosclerosis and plaque rupture leading to myocardial infarction, stroke and progression of peripheral artery disease remain the leading cause of death worldwide, far surpassing both infectious diseases and cancer [1]. Many investigators once believed that progressive luminal narrowing or stenosis beginning from increased lipid storage and continued growth of smooth-muscle cells in the plaque was the main cause of myocardial infarction [2]. Angiographic studies have, however, identified that culprit lesions do not arise from critical stenosis. Previous work by Ambrose *et al*, Little *et al*, Nobuyoshi *et al* and Giroud *et al* demonstrated that nearly two thirds of myocardial infarctions occur in lesions that showed only moderate stenosis [3-8]. Recent advances in basic and experimental science have established a fundamental role that inflammation and underlying cellular and molecular mechanisms [9-11] contribute to atherogenesis from initiation through progression, plaque rupture and ultimately, thrombosis. The principal pathologic features of atherosclerotic plaques that are prone to rupture are now well described [12]. Accumulations of macrophages in atherosclerotic plaques over-express matrix metalloproteinases (MMPs), such as MMP-1 (collagenase-1), MMP-3 (stromelysin-1), and MMP-9 (gelatinase-B) [13-16]. Over-expression of such matrix-degrading enzymes is believed to contribute to plaque instability and thrombogenicity [17-19]. Thus, the macrophage is an important early cellular marker that indicates and contributes to increased risk of plaque remodeling and subsequent rupture in the coronary, cerebral, and peripheral circulations. Since plaque instability is related to cellular composition as well as anatomical structure, developing a diagnostic method that can simultaneously reveal both is critical to identify vulnerable plaques and would allow *in vivo* monitoring of macrophage density in longitudinal studies in response to cardiovascular interventions.



Currently, x-ray angiography, magnetic resonance imaging (MRI), intravascular ultrasound (IVUS), computed tomography (CT), single-photon emission CT (SPECT) and positron emission tomography (PET) have been utilized to image atherosclerotic cardiovascular diseases (e.g., atherosclerotic plaques in the arterial wall) [20,21]. MRI can achieve molecular imaging using contrast agents [22,23]. IVUS can perform virtual histology by using spectral analysis to identify plaque components [24,25]. CT and PET/CT using contrast agents can image macrophage infiltration into arterial wall with improved sensitivity [26,27]. SPECT/CT can track monocytes recruitment to atherosclerotic plaques *in vivo* [28]. However, none of these techniques is able to provide cellular or subcellular resolution. Two-photon luminescence (TPL) microscopy uses nonlinear optical properties of tissue and has been recently utilized to image plaque components such as endothelial cells, smooth muscle cells [29], elastin fibers [30,31], oxidized LDL [32] and lipid droplets [33] based on their endogenous autofluorescence. Optical coherence tomography (OCT) has been demonstrated to visualize microstructural features such as fibrous cap and surface structure of atherosclerotic plaques with high resolution [34-37]. Due to poor scattering and weak two-photon absorption contrast between macrophages and other plaque components, OCT or TPL microscopy alone, is not able to detect macrophages with high specificity while depicting detailed plaque structures.

To solve this problem, a novel gold nanoparticle called nanorose [38] was used as an imaging contrast agent for TPL microscopy to target macrophages. The 30 nm diameter nanorose is characterized by the assembly of thin gold shell (1-2.5 nm in thickness) coated iron oxide (5 nm in diameter) nanoparticles. Dextran-coated nanoroses were injected intravenously and engulfed by aorta-based macrophages or blood-based monocytes [39]. Broad near infrared (650-800 nm) absorption of nanorose is achieved by

the asymmetric core-shell geometry and plasmonic effects arising from close spacing between primary particles in the cluster (Figure 7.1A). Nanorose specificity is achieved since endogenous fluorescence emission (in response to 800 nm two-photon excitation) of collagen, elastin fibers, oxidized-LDL, calcification and lipid are all below 650 nm [32,33,40] while TPL emission of nanorose is broad and emission intensity increases beyond this wavelength (Figure 7.1B). Two emission channels (<570 nm and 700/75 nm) were selected to separate nanorose-loaded macrophages and other aorta components in TPL microscopy.

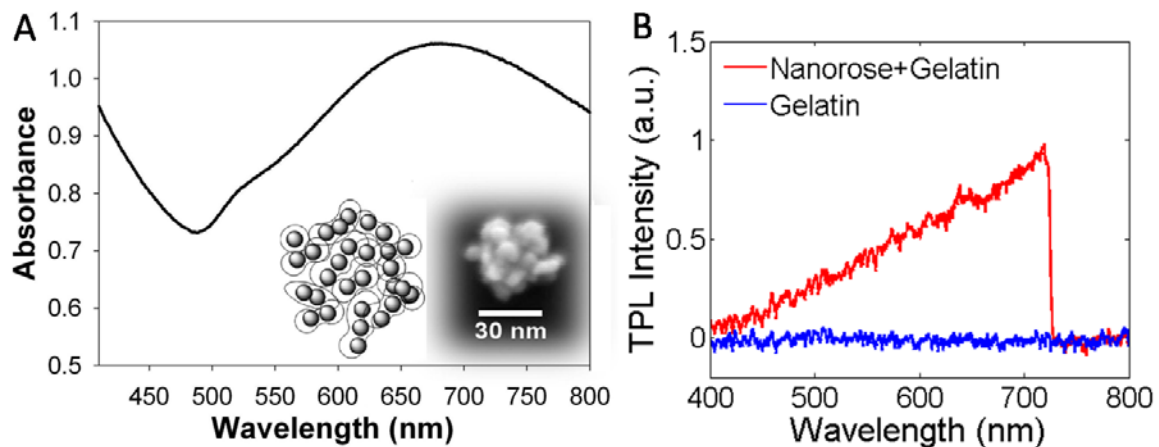


Figure 7.1. A: Absorbance spectrum of nanorose colloidal suspension. Inset shows a schematic cartoon (left) and scanning electron microscopy image (right) of a single nanorose cluster. B: TPL emission spectra of nanorose in gelatin (red) and gelatin alone (blue) at an excitation wavelength of 800 nm. Nanorose suspension ( $3.3 \times 10^{11}$  nanoroses/ml) was mixed with 8% (wt/wt) gelatin to make a nanorose-gelatin tissue phantom ( $1.99 \times 10^{11}$  nanoroses/ml). A shortpass filter (<750 nm) was placed in front of the spectrometer detector in order to block the laser line.

In this study, we demonstrate for the first time that TPL microscopy in combination with OCT using nanorose as a contrast agent can identify aorta-based macrophages in the context of aorta surface structure in a double-balloon injured hypercholesterolemic rabbit model. Presence of nanorose-loaded macrophages was confirmed by co-localization of TPL microscopy of nanorose and RAM-11 staining of

macrophages in aorta histological sections. This combined imaging approach can simultaneously reveal cellular composition and anatomical structure of the aorta and has the potential to assess macrophage distribution over time.

## 7.3 MATERIALS AND METHODS

### 7.3.1 Synthesis of Imaging Contrast Agent (Nanorose)

Details of nanorose synthesis were described previously [38]. Briefly, iron oxide nanoparticles were first synthesized using a method modified from Shen *et al* [41]. 4 ml of  $\text{NH}_4\text{OH}$  (>25% wt/wt) was used to titrate 15 ml of a dextran aqueous solution (15% wt/wt) to pH 11.7. To this, 5 ml of freshly prepared 0.75 g of  $\text{FeCl}_3 \cdot 6\text{H}_2\text{O}$  and 0.32 g of  $\text{FeCl}_2 \cdot 4\text{H}_2\text{O}$  aqueous solution was injected dropwise after passing through a hydrophilic 0.2  $\mu\text{m}$  filter. The suspension immediately turned black and was stirred for 0.5 h. The mixture was then centrifuged at 10,000 rpm for 9 min to remove aggregates. The supernatant was decanted and dialyzed (Spectra/Pro 7, Spectrum Laboratories) against DI water for 24 h. To concentrate dispersions, a centrifugal filter device (Ultracel YM-30, Millipore) was used with a relative centrifugal force of 1500 g. To synthesize the gold-coated iron oxide clusters, 0.1 ml (14.6 mg Fe/ml) of dextran-coated iron oxide nanoparticles was dispersed in 8.9 ml of DI water, along with 100  $\mu\text{l}$  of 1% hydroxylamine seeding agent was added and 0.5 g of dextrose. The solution pH was adjusted to 9.0 using 20  $\mu\text{l}$  of 7%  $\text{NH}_4\text{OH}$  solution.  $\text{HAuCl}_4$  aqueous solution (6.348 mM) was added in aliquots of 100  $\mu\text{l}$  to the stirred dispersion. A total of 4 injections were added with 10 min between each injection. The gold-coated iron oxide nanoclusters were separated from iron oxide only clusters by centrifugation at 6000 rpm for 6 min. The supernatant was decanted and the pellet was redispersed in 0.1 ml 10% dextran solution and 0.01 ml of a 5% polyvinyl alcohol solution to form a nanorose suspension.

### 7.3.2 Preparation of Macrophage Cell Culture and Rabbit Arterial Tissues

Macrophage cells were cultivated in Dulbecco's modified Eagle's medium (DMEM) supplemented with 10% fetal bovine serum (FBS). To load nanorose in cells, macrophages were incubated with nanorose suspension ( $3 \times 10^{10}$  nanoroses/ml) in DMEM overnight and then mixed with 6% gelatin (wt/wt). Nanorose-loaded macrophages ( $2.97 \times 10^6$  cells/ml) and control macrophages without nanorose ( $2.59 \times 10^6$  cells/ml) were imaged by TPL microscopy with 800 nm excitation and TPL from macrophages was detected in two channels (red channel: bandpass (700/75 nm), green channel: shortpass (< 570 nm)).

Abdominal aortas were collected from two male double-balloon injured and fat fed New Zealand white rabbits: nanorose- (Positive) and saline-injected (Control) rabbits (Figure 7.2A). Briefly, following a two-week 0.25% cholesterol chow diet, the abdominal aorta was balloon injured twice and became rich in intimal hyperplasia and macrophages, while the thoracic aorta was not balloon injured and had little intimal hyperplasia and few macrophages (Figure 7.2B,C,D). The rabbits were continuously fat fed for six weeks and intravenously injected with nanorose (1.4 mg Au/kg) and saline respectively three days before sacrifice. *Ex vivo* abdominal aorta with macrophages were harvested, flushed clean of red blood cells and cut into aorta segments ( $8 \times 8 \times 2$  mm<sup>3</sup>) positioned en face onto glass slides with the luminal side face-up for imaging as shown in Figure 2E,F. The aorta segments were first imaged by OCT, then pre-screened by photothermal wave (PTW) imaging [42] to identify "hot spots" where high concentration of nanoroses are located, and finally the hot spots were imaged by TPL microscopy with 800 nm excitation. All imaging experiments were completed within 12 hours after animal sacrifice. The animal protocol was approved by the University of Texas Health Science Center at San Antonio IACUC.

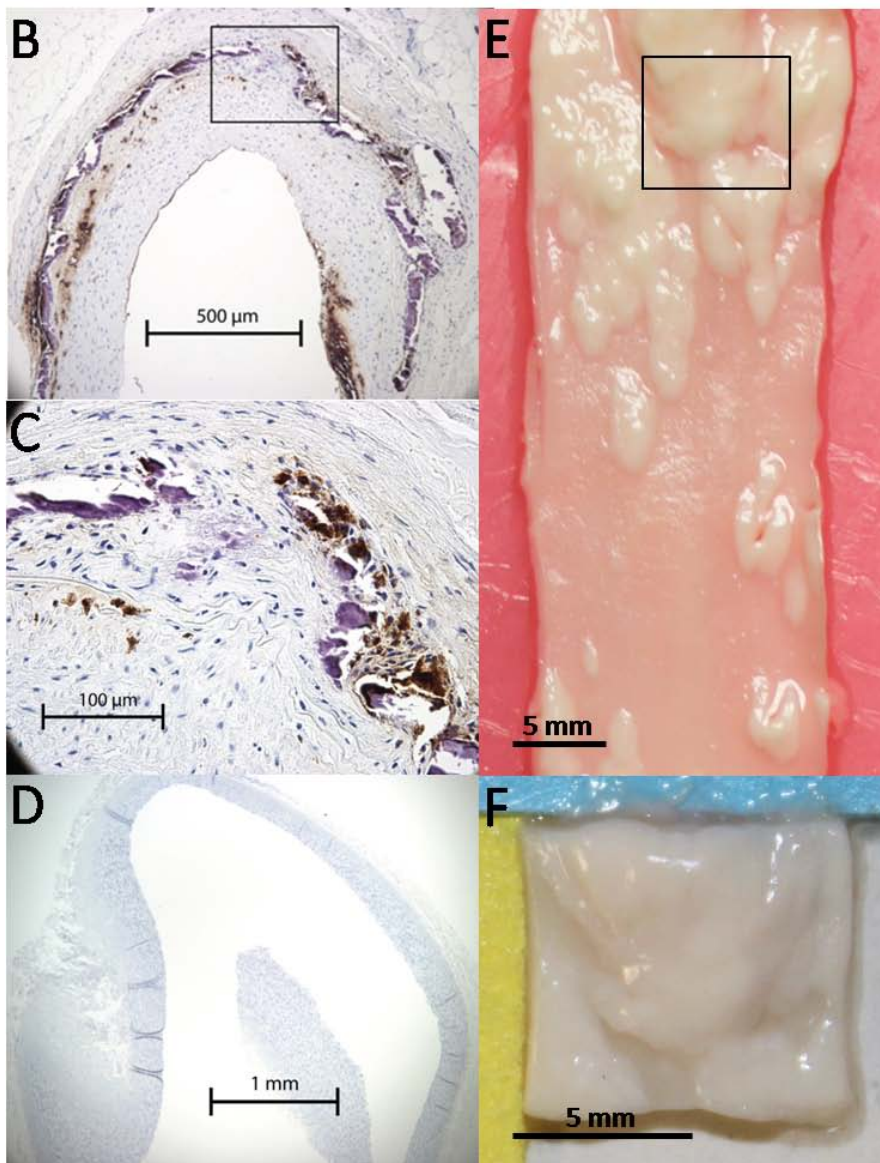
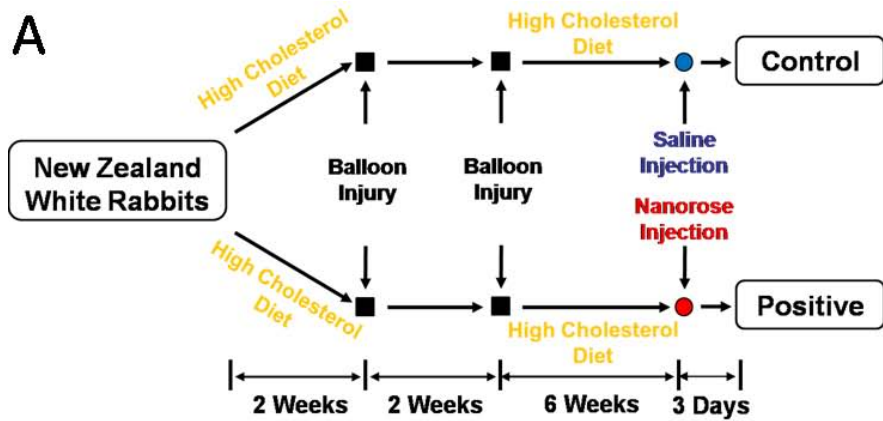


Figure 7.2. A: Rabbit model of aorta inflammation with intimal hyperplasia. B: RAM-11 staining of a cross-section of abdominal aorta. C: Amplified view of the black box in (B). Brown color indicates macrophages. D: RAM-11 staining of a cross-section of thoracic aorta. E: A piece of abdominal aorta with intimal hyperplasia. F: An aorta segment ( $8 \times 8 \times 2 \text{ mm}^3$ ) cut from the black box in (E).

### 7.3.3 Experimental Setup

#### *TPL Microscopy*

TPL from nanorose was measured using a custom-built NIR laser scanning multiphoton microscope described previously (Figure 7.3A) [43]. A femtosecond Ti:Sapphire laser (Mira 900, Coherent) emitting at 800 nm (76 MHz, 300 fs) was used as an excitation light source. Intensity of the laser beam entering the microscope was modulated by an acousto-optic modulator (23080-1, NEOS Technologies) and monitored by a pick-off mirror (reflectance 1 %) with a photodiode calibrated for measuring the power delivered to the objective's back aperture. The focal volume of the objective lens (20 $\times$ , NA=0.95, water emersion, Olympus) was scanned over the sample in the x-y plane using a pair of galvanometric scanning mirrors (6215HB, Cambridge Technology) to produce 2-D images. TPL from the aorta segment was directed into two channels and detected by two photomultiplier tubes (PMT1: H7422P-40, PMT2: H7422P-50, Hamamatsu). To separate endogenous aorta fluorescence from nanorose luminescence, aorta fluorescence with emission wavelengths shorter than 570 nm was reflected by a long-pass filter (E570LP, Chroma Technology) and collected by PMT1 (green channel), while nanorose luminescence with emission wavelengths longer than 570 nm transmitted through a band-pass filter (HQ700/75m, Chroma Technology) and was collected by PMT2 (red channel). The laser power applied at cell culture and arterial tissue (*ex vivo* aorta segment and histological section) was 15 and 20 mW, respectively. No nanorose damage or photo-bleaching effect was observed during imaging.

## OCT

A swept source (SS) laser (HSL-1000, Santec) with a center wavelength of 1060 nm and a bandwidth of 80 nm scanning at a repetition rate of 34 KHz was used in the custom-built intensity OCT system (Figure 7.3B). Average power incident on the sample arm was 1.2 mW. The measured free-space axial resolution was 20  $\mu\text{m}$  with a 2.8 mm scan depth. The OCT signal was sampled with a linear k-space sampling clock to allow real-time OCT image acquisition and display. The linear k-space clock was generated by splitting a portion of the source light into a Mach-Zehnder interferometer and into a balanced detector. The clock signal was filtered, frequency-quadrupled and used as the input to the external clock port of the ADC card. The laser sweep rate governs the A-scan rate of 34 kHz and images were acquired at a rate of 68 B-scans per second with 500 A-scans per B-scan.

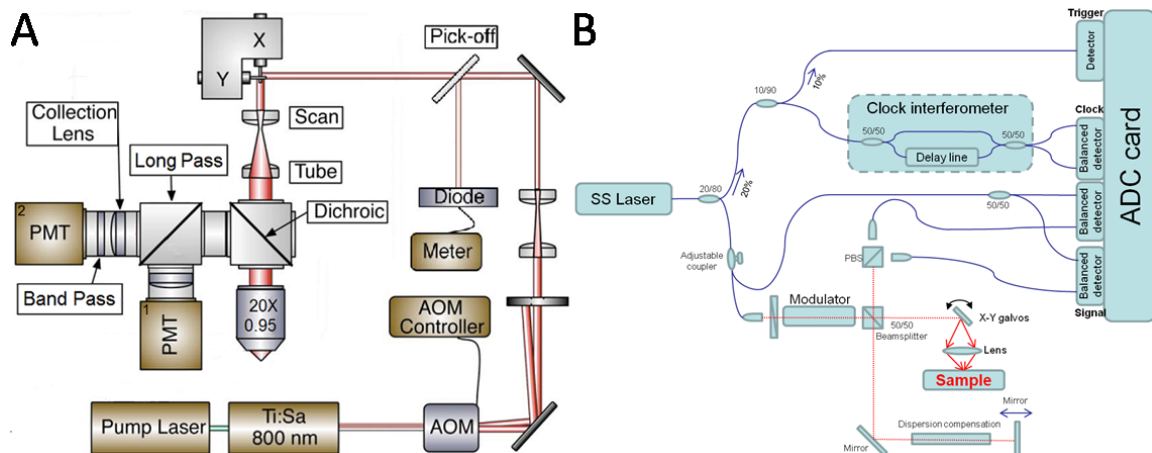


Figure 7.3. Schematic diagrams of (A) TPL microscopy and (B) intensity OCT system.

## PTW Imaging System

A semiconductor laser (FCTS/B, Opto Power) that emits at a wavelength of 800 nm with output power of 0.25 W was used to irradiate rabbit arterial and liver tissues to induce photothermal waves from nanorose. A 50 mm diameter lens ( $f=40$  cm) was used

to focus the laser beam to a 1 cm diameter spot on the tissue samples. A mechanical shutter intensity-modulated continuous laser light at a fixed frequency of 4 Hz with a 50% duty cycle. The IR signal (radiometric temperature) emitted from the tissue surface was reflected by a dichroic mirror and recorded by an IR camera (ThermoVision SC6000 with an InSb detector (3.0-5.0  $\mu\text{m}$ ), FLIR) over a 20 second time period at a frame acquisition rate of 25.6 Hz. The extraction of amplitude PTW images ( $256 \times 320$  pixels) at 4 Hz was performed by computing a fast Fourier transform (FFT) at each pixel of the recorded temporal IR image sequence.

#### **7.3.4 Histology Analysis**

Aorta sections (5  $\mu\text{m}$  in thickness) were immersion-fixed in formalin, processed with paraffin embedding and stained with RAM-11 [44], a marker of rabbit macrophage cytoplasm.

## **7.4 RESULTS**

### **7.4.1 TPL Microscopy of Nanorose-loaded Macrophages in Cell Culture**

We investigated the capability of nanorose uptake by macrophages and use of nanorose as an imaging contrast agent for TPL microscopy in macrophage cell culture. Macrophage cell cultures were selected to simulate the intimal layer of an atherosclerotic aorta since high concentration of macrophages in the arterial intima are characteristic of atherosclerotic plaques. TPL from macrophages were divided into two channels and co-registered into a merged two-channel image (Figure 7.4). In macrophage culture with nanorose, strong TPL signals are detected inside macrophages in the red channel while much weaker TPL signal level is observed in the green channel (Figure 7.4A,B). In the control macrophages without nanorose no TPL signal is detected in either red or green channel (Figure 7.4D,E) at the same input laser power (15 mW). When TPL from



nanorose is detected in both red and green channels, nanorose appears yellowish red (Figure 7.4C). The nonlinear nature of the TPL signal was analyzed by measuring the dependence of the luminescence intensity as a function of laser excitation power. Excitation laser power was monitored by a photodiode giving the power of 13-30 mW delivered to the nanorose-loaded macrophages in cell culture. Luminescence intensities were measured by PMT2 (red channel). Figure 4G illustrates the quadratic dependence of luminescence intensity on the excitation laser power with a slope value of 2.07, confirming a TPL process.

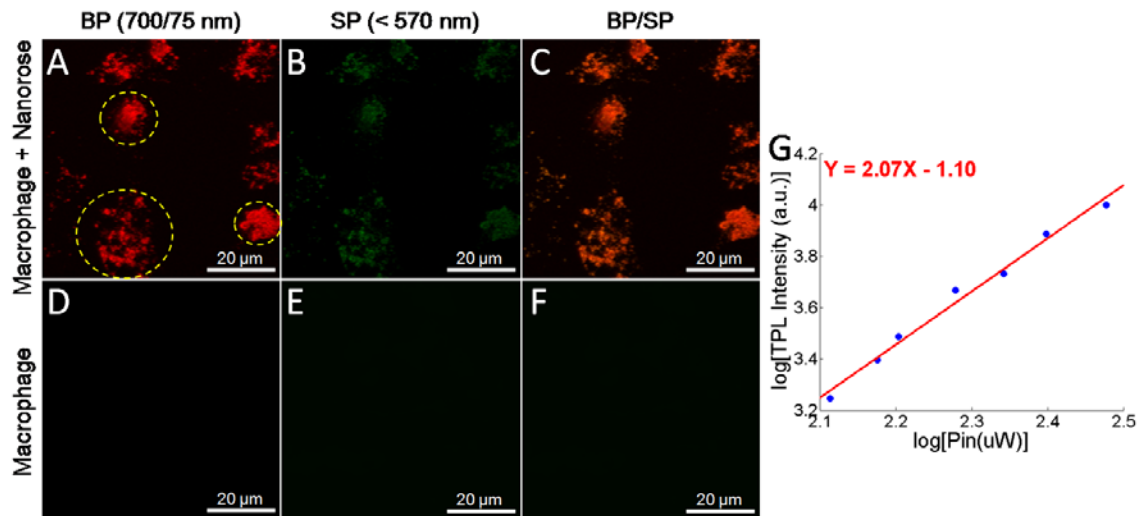


Figure 7.4. Co-registered TPL images of (A,B) nanorose-loaded macrophages and (D,E) control macrophages without nanorose in two channels (red and green). C,F: Merged two-channel images of (A,B) and (D,E) respectively. G: Quadratic dependence of luminescence intensity (red channel) of nanoroses in macrophage cell culture on excitation laser power of 13-30 mW at 800 nm. A slope of 2.07 confirms the TPL process. Yellow circles in (A) indicate macrophage cells. BP: band-pass (700/75 nm); SP: short-pass (<570 nm).

#### 7.4.2 Imaging Ex Vivo Rabbit Tissues

*Ex vivo* segments of rabbit liver and aorta were imaged by OCT, PTW imaging and TPL microscopy to obtain aorta surface structure and nanorose distribution. Rabbit liver was selected as a positive control because liver is known to contain a high density of

macrophages. Several interesting findings of these imaging experiments are illustrated in Figure 5. Detailed surface structure of aorta segments is depicted by OCT (Figure 7.5B,F). Peak and valley regions of the aorta surface are clearly visible in the 3-D OCT image. Due to strong NIR absorption by nanorose, PTW imaging is able to screen nanorose distribution in the whole aorta segment. High intensity PTW signals are observed in both abdominal aorta and liver segments (bright region Figure 7.5C,I) from the Positive rabbit with nanorose injection but not from the Control rabbit (Figure 7.5G,K). Moreover, PTW signals are not observed in healthy thoracic aorta regions with no intimal hyperplasia from the Positive rabbit (data not shown). Due to the double-balloon injury process, the distribution of nanorose in abdominal aorta from the Positive rabbit is diffusive (Figure 7.5C) with respect to the corresponding aorta surface structure as shown by OCT (Figure 7.5B).

Nanorose is also detected by TPL microscopy in the same aorta and liver segments from the Positive rabbit over a smaller field of view ( $500 \times 500 \times 80 \mu\text{m}^3$ ) as denoted by the red boxes in Figure 5C,I. Strong TPL signals from nanorose are observed (red color in Figure 7.5D,J). Nanoroses are identified to be diffusely located in lateral directions of the tissue segments (Figure 7.5D,J). From a side view of Figure 5D, nanoroses are also observed to be diffusely distributed in the axial direction along the luminal surface of the aorta segment within  $20 \mu\text{m}$  in depth. In comparison, endogenous fluorescence signal detected from control aorta and liver segments is much weaker than nanorose TPL from the Positive rabbit at the same laser power delivered to the tissue (Figure 7.5H,L). Moreover, the endogenous fluorescence signal is only detected in the green channel, suggesting that no nanorose is identified which emits stronger TPL in the red channel. Insets of Figure 5D,J show a closer view of nanorose distribution with strong TPL signal intensity, while much higher laser powers (59 and 45 mW), respectively, were

needed to show the tissue structures from the Control rabbit at a similar endogenous fluorescence signal intensity in insets of Figure 5H,L.

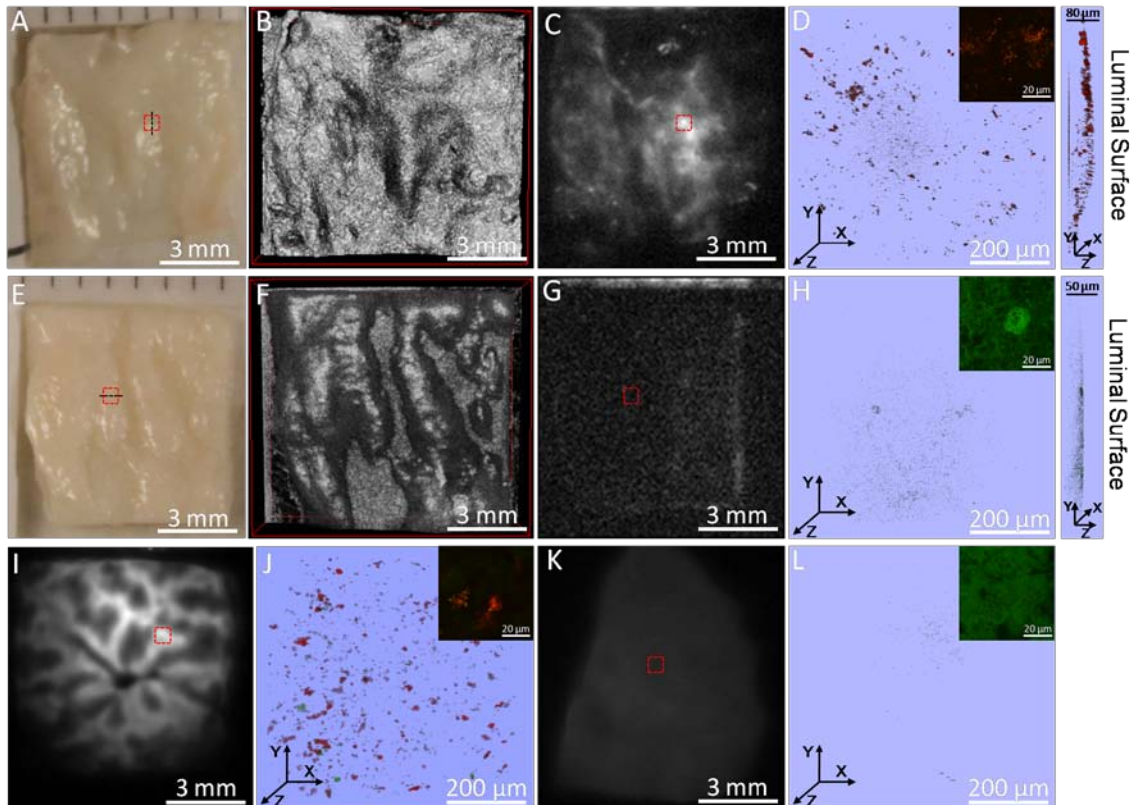


Figure 7.5. A,B,C,D: Digital image, 3-D OCT, PTW imaging and 3-D two-channel TPL microscopy (red box in (A,C)) of an abdominal aorta segment from the Positive rabbit. E,F,G,H: Digital image, 3-D OCT, PTW imaging and 3-D two-channel TPL microscopy (red box in (E,G)) of an abdominal aorta segment from the Control rabbit. I,J: PTW imaging and 3-D two-channel TPL microscopy (red box in (I)) of a liver segment from the Positive rabbit. K,L: PTW imaging and 3-D two-channel TPL microscopy (red box in (K)) of a liver segment from the Control rabbit. Inset in (D,H,J,L) shows a two-channel TPL image at a single depth at an amplified view within the corresponding 3-D TPL image. Right side of (D,H) shows a side view of the corresponding 3-D TPL image. Laser power delivered to the sample is 20 mW in all TPL measurements except insets of (H) 59 mW and (L) 45 mW.

To verify that TPL signals from abdominal aorta segment from the Positive rabbit (Figure 7.5D) originate from nanorose-loaded macrophages, unstained histological sections as denoted by the black dashed lines in Figure 5A,E were cut off and imaged by

TPL microscopy. Sister histological sections (5  $\mu\text{m}$  apart from the corresponding unstained sections) were stained with RAM-11. Positive RAM-11 staining of the intimal layer (Figure 7.6A,E) indicates presence of infiltrated macrophages in the aorta. High intensity TPL signals from nanorose (red color in Figure 7.6B,C,D and pointed by yellow arrows in Figure 7.6D) in the intimal layer co-localize with corresponding RAM-11 staining of superficial macrophages (Figure 7.6A and inset in Figure 7.6D), suggesting that TPL signals in red color are generated from superficial nanorose-loaded macrophages. The size of nanorose aggregations in the macrophages are 1-2  $\mu\text{m}$  (Figure 7.6D). Although macrophages are observed as deep as 100  $\mu\text{m}$  from luminal surface of the aorta, most nanoroses are detected within 20  $\mu\text{m}$  (Figure 7.6D), consistent with nanorose distribution in the axial direction in the reconstructed 3-D TPL image of the same aorta segment from the Positive rabbit (side view of Figure 7.5D). This observation may suggest that the nanorose-loaded macrophages mostly reside in the very superficial regions of intima and have not migrated to deeper locations up to three days after intravenous nanorose injection. In contrast, in the unstained histological section from the Control rabbit, only endogenous fluorescence from aorta (green color) is observed in both superficial intima (Figure 7.6F,I) and deeper intima (Figure 7.6G,J) although dense accumulation of macrophages are identified with corresponding RAM-11 stain in these regions (Figure 7.6E).

Endogenous fluorescence from aorta may originate from elastin fibers (pointed by white arrows in media layer in Figure 7.6B,H) [29,33,40]. Moreover, macrophage-like cellular structures with dark nuclei (indicated by yellow circles in Figure 7.6I,J) and possibly lipid droplets (pointed by yellow arrow heads in Figure 7.6D,J) in or outside macrophages are also observed [45,46].

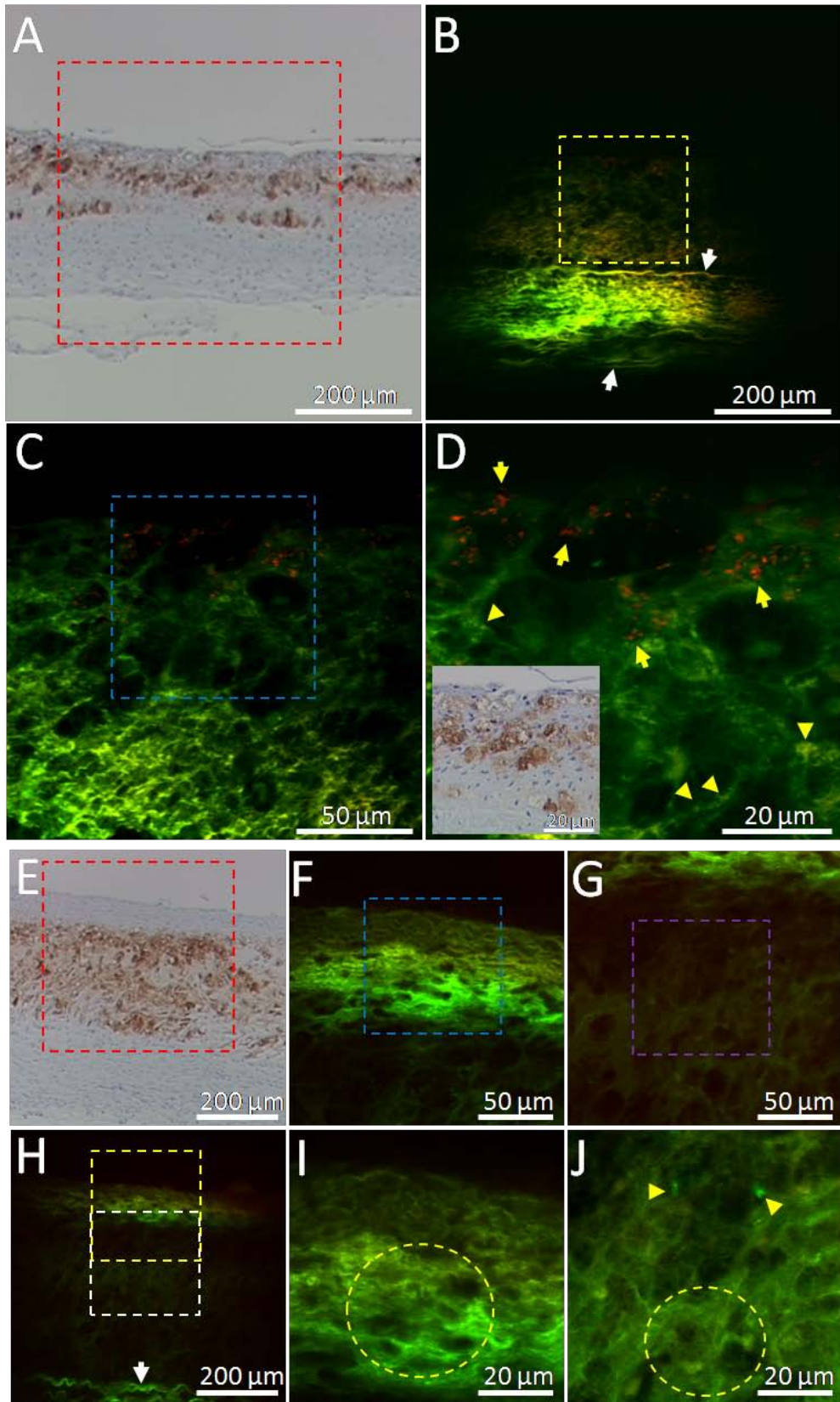


Figure 7.6. A: RAM-11 stain with positive macrophage staining of the black dashed line in Figure 5A. B,C,D: Two-channel TPL images of the red, yellow and blue boxes in (A), (B) and (C) respectively. Red color indicates TPL signals from nanorose. Green color indicates endogenous fluorescence from aorta. Inset in (D) is a co-localized RAM-11 stain image of (D) amplified from (A). E: RAM-11 stain with positive macrophage staining of the black dashed line in Figure 5E. H: TPL image of the red box in (E). F,I: TPL images of the yellow and blue boxes in (H) and (F) respectively. G,J: TPL images of the white and purple boxes in (H) and (G) respectively. Yellow arrows in (D) point to nanoroses. Yellow arrow heads in (D,J) point to lipid droplets. White arrows in (B,H) point to elastin fibers. Yellow circles in (I,J) indicate clusters of macrophage cells defined by dark nuclei. Laser power delivered to the sample is 20 mW. High intensity TPL signals from nanorose in intimal layer (B,C,D) co-localize with corresponding RAM-11 staining of superficial macrophages in the histological section from the Positive rabbit (A), while no TPL signal from nanorose (red color) is observed in the histological section from the Control rabbit (F,G,H,I,J).

## 7.5 DISCUSSION

Nanorose was tested in macrophage cell culture as an imaging contrast agent for TPL microscopy. Due to a dextran coating and 30 nm particle size, a high uptake rate of nanorose by macrophages compared to gold nanoshells is observed and measured to be more than 7500 nanoroses per macrophage cell [47]. Higher TPL signal intensity is observed in the red channel (700/75 nm) compared to green channel (<570 nm) from the nanorose-loaded macrophages (Figure 7.4A,B), consistent with the TPL spectrum of nanorose (Figure 7.1B). Endogenous fluorescence from control macrophages without nanorose is not observed when the same laser power is applied (Figure 7.4D,E). In fact, 10 times greater laser power than that used in nanorose-loaded macrophages is needed (data not shown) to bring endogenous fluorescence intensity from control macrophages to the same signal level induced by nanorose as shown in Figure 4A.

To demonstrate the capability of TPL microscopy in combination with OCT to detect aorta-based macrophages, a hypercholesterolemic rabbit model of focal aorta inflammation induced by endothelial abrasion followed by double-balloon injury was utilized. The resulting injury-induced neointima in abdominal aorta was particularly rich

in macrophages, simulating macrophage accumulation in atherosclerotic plaques. In contrast to previous studies performed in animal models with diffuse atherosclerosis, this inflammation model allows straightforward anatomic localization of the inflammatory arterial lesion and a direct comparison of diseased versus normal artery portions in the same rabbit (Figure 7.2B,C,D) in a much shorter formation time (from 4-5 months [48] to 10 weeks). Double-balloon injured lesions are widely spread in the aorta, consistent with the high accumulation and diffusive distribution of nanoroses in these areas as detected by TPL microscopy (Figure 7.5D and Figure 7.6B,C,D) and PTW imaging (Figure 7.5C).

Most nanoroses are superficially detected by TPL microscopy within 20  $\mu\text{m}$  from luminal surface of the aorta as shown in the histological section (Figure 7.6D). However, RAM-11 stained macrophages from corresponding sister section were distributed as deep as 100  $\mu\text{m}$  (Figure 7.6A). This observation suggests that macrophages taking up nanorose are superficial in the aorta and nanoroses may migrate and then reside (no-slip condition) on the endothelial surface and be partially engulfed by superficial macrophages. Deeper *in situ* macrophages and macrophages that migrated into deeper locations before nanorose injection may not be able to take up nanorose possibly because nanorose cannot penetrate into the intima directly through diffusion or no nanorose is delivered through the vasa vasorum. In fact, vascular permeability and rate of particle (molecule or nanoparticle) transfer from the vascular lumen to peripheral tissue is regulated and limited by transcytosis of endothelial cells [49,50]. Moreover, apoptotic and necrotic macrophages contribute to lipid core formation in advanced atherosclerotic plaques [51]. These macrophage debris can stain RAM-11 positive but are not intact and would no longer take up nanorose *in situ*.

Although nanorose uptake by macrophages has been identified in our cell culture study (Figure 7.4), their transport pathway to aorta-based macrophages is not elucidated.

Previous studies have proposed three possible mechanisms for transport of superparamagnetic nanoparticles to arterial tissue [52-55], including monocyte-mediated migration, transcytosis across the endothelium followed by uptake by *in situ* macrophages and diffusion into the adventitia via the vasa vasorum. TPL microscopy results of histological sections (Figure 7.6B) show that nanorose is not detected at deeper locations (e.g., 100-300  $\mu\text{m}$ ) in the aorta, indicating that nanorose diffusion via the vasa vasorum may not have occurred in our study. However, the relative contributions of monocyte-mediated migration and endothelial diffusion of nanorose remain to be determined.

Simultaneous observation of macrophage distribution and plaque surface structure offers the ability to characterize plaque composition and identify vulnerable plaque regions more prone to rupture. However, several limitations need to be addressed before the current imaging approach can be used in patients with atherosclerosis to study the natural history of plaque inflammation over time and the efficacy of treatments aimed at plaque stabilization. First, TPL microscopy and OCT were performed in this study, respectively, on *ex vivo* tissues. An intravascular catheter is required to realize *in vivo* imaging of macrophages in plaques. Second, TPL microscopy has a smaller field of view than OCT in the current study. Co-registered fields of view can be achieved by coupling two-photon excitation light with OCT light into a catheter. Third, the penetration depth of TPL microscopy is shorter than OCT at current wavelength (800 nm versus 1060 nm). A longer wavelength for two-photon excitation will provide deeper penetration depth in tissue. Although the current study utilized a model of arterial wall inflammation which does not contain the complex nature of advanced atherosclerotic plaques, TPL microscopy in combination with OCT using nanorose as a contrast agent to detect plaque-based macrophages and assess macrophage density quantitatively is promising.



Additional studies are required to test the capability of this combined imaging approach for detection of macrophages in vulnerable atherosclerotic plaques.

## **7.6 CONCLUSION**

By utilizing TPL microscopy in combination with OCT we demonstrated detection of nanorose with respect to aorta surface structure in a double-balloon injured hypercholesterolemic rabbit model. Nanorose presence was also detected with PTW imaging. Co-localization of nanorose identified by TPL microscopy with RAM-11 stained macrophages in the corresponding histological section suggests that TPL signal in the red channel (700/75 nm) is generated by superficial nanorose-loaded macrophages. Our results suggest that nanorose-loaded macrophages are diffusively distributed in the aorta and superficially located (within 20  $\mu\text{m}$  from the luminal surface). This study indicates that combined TPL microscopy and OCT is promising for detection of aorta inflammation in the hypercholesterolemic rabbit using nanorose as a contrast agent. This combined imaging approach will need to be tested in further studies for macrophage detection in atherosclerotic plaques.

## **7.7 ACKNOWLEDGEMENTS**

The authors would like to acknowledge the technical support from the University of Texas Health Science Center at San Antonio. This study was supported in part by a travel grant from the American Society for Laser Medicine and Surgery to Wang, a Veterans Administration merit grant to Feldman, a Welch Foundation grant F-1319 and NSF grant CBET-0968038 to Johnston, and the Department of Energy Center for Frontiers of Subsurface Energy Security.

## 7.8 REFERENCES

- [1] Yusuf S, Reddy S, Ounpuu S, Anand S, "Global burden of cardiovascular diseases: part I: general considerations, the epidemiologic transition, risk factors, and impact of urbanization," *Circulation* 104, 2746-2753 (2001)
- [2] Libby P, Aikawa M, "Stabilization of atherosclerotic plaques: New mechanisms and clinical targets," *Nature Med* 8, 1257-1262 (2002)
- [3] Ambrose JA, Winters SL, Stern A, Eng A, Teichholz LE, Gorlin R, Fuster V, "Angiographic morphology and the pathogenesis of unstable angina pectoris," *J Am Coll Cardiol* 5, 609-616 (1985)
- [4] Ambrose JA, Tannenbaum MA, Alexopoulos D, Hjemdahl-Monsen CE, Leavy J, Weiss M, Borricco S, Gorlin R, Fuster V, "Angiographic progression of coronary artery disease and the development of myocardial infarction," *J Am Coll Cardiol* 12, 56-62 (1988)
- [5] Hackett D, Davies G, Maseri A, "Pre-existing coronary stenosis in patients with first myocardial infarction are not necessarily severe," *Eur Heart J* 9, 1317-1323 (1988)
- [6] Little WC, Downes TR, Applegate RJ, "The underlying coronary lesion in myocardial infarction: implications for coronary angiography," *Clin Cardiol* 14, 868-874 (1991)
- [7] Nobuyoshi M, Tanaka M, Nosaka H, Kimura T, Yokoi H, Hamasaki N, Kim K, Shindo T, Kimura K, "Progression of coronary atherosclerosis: is coronary spasm related to progression?," *J Am Coll Cardiol* 18, 904-910 (1991)
- [8] Giroud D, Li JM, Urban P, Meier B, Rutishauer W, "Relation of the site of acute myocardial infarction to the most severe coronary arterial stenosis at prior angiography," *Am J Cardiol* 69, 729-732 (1992)

- [9] Libby P, Ridker PM, Maseri A, "Inflammation and atherosclerosis," *Circulation* 105, 1135-1143 (2002)
- [10] Libby P, Theroux P, "Pathophysiology of coronary artery disease," *Circulation* 111, 3481-3488 (2005)
- [11] Lucas AR, Korol R, Pepine CJ, "Inflammation in atherosclerosis: some thoughts about acute coronary syndromes," *Circulation* 113, e728-732 (2006)
- [12] Davies MJ, Thomas A, "Thrombosis and acute coronary-artery lesions in sudden cardiac ischemic death," *N Engl J Med* 310, 1137-1140 (1984)
- [13] Johnson JL, George SJ, Newby AC, Jackson CL, "Divergent effects of matrix metalloproteinases 3, 7, 9, and 12 on atherosclerotic plaque stability in mouse brachiocephalic arteries," *Proc Natl Acad Sci* 102, 15575-15580 (2005)
- [14] Henney AM, Wakeley PR, Davies MJ, Foster K, Hembry R, Murphy G, Humphries S, "Localization of stromelysin gene expression in atherosclerotic plaques by in situ hybridization," *Proc Natl Acad Sci* 88,8154-8158 (1991)
- [15] Galis ZS, Sukhova GK, Lark MW, Libby P, "Increased expression of matrix metalloproteinases and matrix degrading activity in vulnerable regions of human atherosclerotic plaques," *J Clin Invest* 94, 2493-2503 (1994)
- [16] Nikkari ST, O'Brien KD, Ferguson M, Hatsukami T, Welgus HG, Alpers CE, Clowes AW, "Interstitial collagenase (MMP-1) expression in human carotid atherosclerosis," *Circulation* 92, 1393-1398 (1995)
- [17] Libby P, Geng YJ, Aikawa M, Schoenbeck U, Mach F, Clinton SK, Sukhova GK, Lee, RT, "Macrophages and atherosclerotic plaque stability," *Curr Opin Lipidol* 7, 330-335 (1996)

- [18] Taubman MB, Fallon JT, Schechter AD, Giesen P, Mendlowitz M, Fyfe BS, Marmur JD, Nemerson Y, "Tissue factor in the pathogenesis of atherosclerosis," *Thromb Haemost* 78, 200-204 (1997)
- [19] Kolodgie FD, Virmani R, Burke AP, Farb A, Weber DK, Kutys R, Finn AV, Gold HK, "Pathologic assessment of the vulnerable human coronary plaque," *Heart* 90, 1385-1391 (2004)
- [20] Sanz J, Fayad ZA, "Imaging of atherosclerotic cardiovascular disease," *Nature* 451(7181), 953-957 (2008)
- [21] Gershlick AH, de Belder M, Chambers J, Hackett D, Keal R, Kelion A, Neubauer S, Pennell DJ, Rothman M, Signy M, Wilde P, "Role of non-invasive imaging in the management of coronary artery disease: an assessment of likely change over the next 10 years. A report from the British Cardiovascular Society Working Group," *Heart* 93, 423-431 (2007)
- [22] Nahrendorf M, Jaffer FA, Kelly KA, Sosnovik DE, Aikawa E, Libby P, Weissleder R, "Noninvasive vascular cell adhesion molecule-1 imaging identifies inflammatory activation of cells in atherosclerosis," *Circulation* 114, 1504-1511 (2006)
- [23] Amirbekian V, Lipinski MJ, Briley-Saebo KC, Amirbekian S, Aguinaldo JGS, Weinreb DB, Vucic E, Frias JC, Hyafil F, Mani V, Fisher EA, Fayad ZA, "Detecting and assessing macrophages in vivo to evaluate atherosclerosis noninvasively using molecular MRI," *Proc Natl Acad Sci* 104, 961-966 (2007)
- [24] Nair A, Kuban BD, Obuchowski N, Vince DG, "Assessing spectral algorithms to predict atherosclerotic plaque composition with normalized and raw intravascular ultrasound data," *Ultrasound Med Biol* 27, 1319-1331 (2001)
- [25] Kenya N, Etsuo T, Osamu K, Vince DG, Renu V, Jean-Francois S, Akira M, Yoshihiro T, Tatsuya I, Mariko E, Tetsuo M, Mitsuyasu T, Takahiko S, "Accuracy of

- in vivo coronary plaque morphology assessment: a validation study of in vivo virtual histology compared with in vitro histopathology," *J Am Coll Cardiol* 47, 2405-2412 (2006)
- [26] Hyafil F, Cornily JC, Feig JE, Gordon R, Vucic E, Amirbekian V, Fisher EA, Fuster V, Feldman LJ, Fayad ZA, "Noninvasive detection of macrophages using a nanoparticulate contrast agent for computed tomography," *Nature Med* 13, 636-641 (2007)
- [27] Nahrendorf M, Zhang H, Hembrador S, Panizzi P, Sosnovik DE, Aikawa E, Libby P, Swirski FK, Weissleder R, "Nanoparticle PET-CT imaging of macrophages in inflammatory atherosclerosis," *Circulation* 117, 379-387 (2008)
- [28] Kircher MF, Grimm J, Swirski FK, Libby P, Gerszten RE, Allport JR, Weissleder R, "Noninvasive in vivo imaging of monocyte trafficking to atherosclerotic lesions," *Circulation* 117, 388-395 (2008)
- [29] van Zandvoort M, Engels W, Douma K, Beckers L, Oude Egbrink M, Daemen M, Slaaf DW, "Two-photon microscopy for imaging of the (atherosclerotic) vascular wall: a proof of concept study," *J Vasc Res* 41, 54-63 (2004)
- [30] Zoumi A, Lu XA, Kassab GS, Tromberg BJ, "Imaging coronary artery microstructure using secondharmonic and two-photon fluorescence microscopy," *Biophys J* 87, 2778-2786 (2004)
- [31] Boulesteix T, Pena AM, Pages N, Godeau G, Sauviat MP, Beaurepaire E, Schanne-Klein MC, "Micrometer scale ex vivo multiphoton imaging of unstained arterial wall structure," *Cytometry Part A* 69A, 20-26 (2006)
- [32] Le TT, Langohr IM, Locker MJ, Sturek M, Cheng JX, "Label-free molecular imaging of atherosclerotic lesions using multimodal nonlinear optical microscopy," *J Biomed Opt* 12(5), 0540071-05400710 (2007)

- [33] Lilledahl MB, Haugen OA, de Lange Davies C, Svaasand LO, "Characterization of vulnerable plaques by multiphoton microscopy," *J Biomed Opt* 12(4), 0440051-04400512 (2007)
- [34] Brezinski ME, Tearney GJ, Bouma BE, Boppart SA, Hee MR, Swanson EA, Southern JF, Fujimoto JG, "Imaging of coronary artery microstructure (in vitro) with optical coherence tomography," *Am J Cardiol* 77, 92-93 (1996)
- [35] Raffel OC, Tearney GJ, Gauthier DD, Halpern EF, Bouma BE, Jang IK, "Relationship between a systemic inflammatory markers, plaque inflammation, and plaque characteristics determined by intravascular optical coherence tomography," *Arterioscler Thromb Vasc Biol* 27, 1820-1827 (2007)
- [36] Tanaka A, Imanishi T, Kitabata H, Kubo T, Takarada S, Tanimoto T, Kuroi A, Tsujioka H, Ikejima H, Ueno S, Kataiwa H, Okouchi K, Kashiwagi M, Matsumoto H, Takemoto K, Nakamura N, Hirata K, Mizukoshi M, Akasaka T, "Morphology of exertion-triggered plaque rupture in patients with acute coronary syndrome: an optical coherence tomography study," *Circulation* 118, 2368-2373 (2008)
- [37] Vancraeynest D, Pasquet A, Roelants V, Gerber BL, Vanoverschelde JJ, "Imaging the vulnerable plaque," *J Am Coll Cardiol* 57, 1961-1979 (2011)
- [38] Ma LL, Feldman MD, Tam JM, Paranjape AS, Cheruku KK, Larson TA, Tam JO, Ingram DR, Paramita V, Villard JW, Jenkins JT, Wang T, Clarke GD, Asmis R, Sokolov K, Chandrasekar B, Milner TE, Johnston KP, "Small multifunctional nanoclusters (nanoroses) for targeted cellular imaging and therapy," *ACS Nano* 3(9), 2686-2696 (2009)
- [39] Mornet S, Vasseur S, Grasset F, Duguet E, "Magnetic nanoparticle design for medical diagnosis and therapy," *J Mat Chem* 14, 2161-2175 (2004)

- [40] Yu W, Braz JC, Dutton AM, Prusakov P, Rekhter M, "In vivo imaging of atherosclerotic plaques in apolipoprotein E deficient mice using nonlinear microscopy," *J Biomed Opt* 12(5), 0540081-05400810 (2007)
- [41] Shen T, Weissleder R, Papisov M, Bogdanov A, Jr, Brady TJ, "Monocrystalline iron oxide nanocompounds (Mion): physicochemical properties," *Magn Reson Med* 29, 599-604 (1993)
- [42] Wang T, Qiu J, Ma LL, Li X, Sun J, Ryoo S, Johnston KP, Feldman MD, Milner TE, "Nanorose and lipid detection in atherosclerotic plaque using dual-wavelength photothermal wave imaging," *Proc SPIE* 7562, 75620S-75620S-7 (2010)
- [43] Park J, Estrada A, Sharp K, Sang K, Schwartz JA, Smith DK, Coleman C, Payne JD, Korgel BA, Dunn AK, Tunnell JW, "Two-photon-induced photoluminescence imaging of tumors using near-infrared excited gold nanoshells," *Opt Exp* 16(3), 1590-1599 (2008)
- [44] Leibovich SJ, Polverini PJ, Shepard HM, Wiseman DM, Shively V, Nuseir N, "Macrophage-induced angiogenesis is mediated by tumor necrosis factor-alpha," *Nature* 329, 630-632 (1987)
- [45] Lim RS, Kratzer A, Barry NP, Miyazaki-Anzai S, Miyazaki M, Mantulin WW, Levi M, Potma EO, Tromberg BJ, "Multimodal CARS microscopy determination of the impact of diet on macrophage infiltration and lipid accumulation on plaque formation in ApoE-deficient mice," *J Lipid Res* 51, 1729-1737 (2010)
- [46] Wang HW, Langohr IM, Sturek M, Cheng JX, "Imaging and quantitative analysis of atherosclerotic lesions by CARS-based multimodal nonlinear optical microscopy," *Arterioscler Thromb Vasc Biol* 29, 1342-1348 (2009)

- [47] Sapozhnikova V, Willsey B, Asmis R, Wang T, Jenkins JT, Mancuso JJ, Ma L, Kuranov R, Milner TE, Johnston KP, Feldman MD, "Near infrared fluorescence produced by gold nanoclusters (nanoroses)," *J Biomed Opt* (IN PRESS).
- [48] Aikawa M, Rabkin E, Okada Y, Voglic SJ, Clinton SK, Brinckerhoff CE, Sukhova GK, Libby P, "Lipid lowering by diet reduces matrix metalloproteinase activity and increases collagen content of rabbit atheroma: a potential mechanism of lesion stabilization," *Circulation* 97, 2433-2444 (1998)
- [49] Frank PG, Pavlides S, Lisanti MP, "Caveolae and transcytosis in endothelial cells: role in atherosclerosis," *Cell Tissue Res* 335, 41-47 (2009)
- [50] Lu W, Tan YZ, Hu KL, Jiang XG, "Cationic albumin conjugated pegylated nanoparticle with its transcytosis ability and little toxicity against blood-brain barrier," *Int J Pharm* 295, 247-260 (2005)
- [51] Tabas I, "Macrophage apoptosis in atherosclerosis: consequences on plaque progression and the role of endoplasmic reticulum stress," *Antioxid Redox Signal* 11, 2333-2339 (2009)
- [52] Corot C, Petry KG, Trivedi R, Saleh A, Jonkmanns C, Le Bas JF, Blezer E, Rausch M, Brochet B, Foster-Gareau P, Balériaux D, Gaillard S, Dousset V, "Macrophage imaging in central nervous system and in carotid atherosclerotic plaque imaging using ultrasmall superparamagnetic iron oxide in magnetic resonance imaging," *Invest Radiol* 39, 619-625 (2004)
- [53] Dousset V, Delalande C, Ballarino L, Quesson B, Seilhan D, Coussemaq M, Thiaudière E, Brochet B, Canioni P, Caillé JM, "In vivo macrophage activity imaging in the central nervous system detected by magnetic resonance," *Magn Reson Med* 41, 329-333 (1999)



- [54] Rausch M, Hiestand P, Baumann D, Cannel C, Rudin M, "MRI-based monitoring of inflammation and tissue damage in acute and chronic relapsing EAE," *Magn Reson Med* 50, 309-314 (2003)
- [55] Corot C, Robert P, Idée JM, Port M, "Recent advances in iron oxide nanocrystal technology for medical imaging," *Adv Drug Deliv Rev* 58, 1471-1504 (2006)

## Chapter 8 Conclusions and Future Studies

### 8.1 CONCLUSIONS

The principal goal of my research is to develop hybrid optical imaging modalities: PTW imaging combined with OCT, TPLM combined with OCT, and assess the ability of such hybrid imaging modalities to reveal both cellular composition (e.g., macrophages (having taken up plasmonic gold nanoparticles as a contrast agent) and lipid deposits) and anatomical structure of atherosclerotic plaques. PTW imaging combined with OCT shows that superficial nanorose-loaded macrophages are distributed at shoulders on the upstream side of atherosclerotic plaques at edges of lipid deposits in a rabbit model of atherosclerosis. TPLM combined with OCT shows that nanorose-loaded macrophages are diffusively distributed and mostly detected superficially within 20  $\mu\text{m}$  from the luminal surface of the aorta in a rabbit model of aorta inflammation.

#### 8.1.1 Measurement of Optical Properties of Nanorose

In this doctoral dissertation, a gold-coated iron oxide nanoparticle cluster, nanorose, is used as a contrast agent to target macrophages in PTW imaging, confocal microscopy and TPLM. The absorption and scattering cross-sections of nanorose are determined from a direct optical properties measurement and a DDA simulation. Experiment indicates that absorption cross-section is  $\sigma_a = (3.1 \pm 0.5) \times 10^{-14} \text{ m}^2$ . DDA results indicate that nanorose absorption cross-section is an order of magnitude larger than the scattering cross-section (Chapter 3).

#### 8.1.2 Dual-wavelength Multi-frequency PTW Imaging Combined with OCT for Macrophage and Lipid Detection in Atherosclerotic Plaques Using Gold Nanoparticles

PTW imaging was first investigated to detect nanorose-loaded macrophages in atherosclerotic plaques. By utilizing PTW imaging in response to 800 and 1210 nm laser

irradiation we demonstrated detection of PTW signals from nanorose and lipid deposits in atherosclerotic plaques. Moreover, multi-frequency (0.1, 1 and 4 Hz) PTW imaging can be used to distinguish nanorose and lipid deposits distributed at different depths. Nanorose presence was also identified with TPL microscopy in histological sections. Co-localization of nanorose in TPL microscopy images with RAM-11 stained macrophages suggests that PTW signals at 800 nm laser irradiation is generated by superficial nanorose-loaded macrophages. Amplitude PTW images (800 and 1210 nm) at a modulation frequency of 4 Hz merged with a co-registered OCT image demonstrated the location and distribution of superficial nanorose-loaded macrophages and lipid deposits with respect to plaque surface structure and direction of blood flow. Our results suggest that nanorose-loaded macrophages are distributed at plaque shoulders on the upstream side, at edges of lipid deposits, and superficially located (within 20  $\mu\text{m}$  from plaque surface). This *ex vivo* animal study suggests that combined PTW-OCT imaging is a promising approach for multi-depth screening of nanorose-loaded macrophages and lipid deposits in atherosclerotic plaques (Chapters 4 and 6).

### **8.1.3 Combined TPLM and OCT for Macrophage Detection in the Hypercholesterolemic Rabbit Aorta Using Plasmonic Gold Nanorose**

TPLM has been employed to detect aorta components such as nanorose-loaded macrophages, elastin fibers and lipid droplets. By utilizing TPLM in combination with OCT we demonstrated detection of nanorose with respect to aorta surface structure in a double-balloon injured hypercholesterolemic rabbit model. Nanorose presence was also detected with PTW imaging. Co-localization of nanorose identified by TPLM with RAM-11 stained macrophages in the corresponding histological section suggests that TPL signal in the red channel (700/75 nm) is generated by superficial nanorose-loaded macrophages. Results suggest that nanorose-loaded macrophages are diffusively

distributed in the aorta and superficially located (within 20  $\mu\text{m}$  from the luminal surface). This study indicates that combined TPLM and OCT is promising for detection of aorta inflammation in the hypercholesterolemic rabbit using nanorose as a contrast agent. This combined imaging approach will need to be tested in further studies for macrophage detection in atherosclerotic plaques (Chapter 7).

## **8.2 FUTURE STUDIES**

### **8.2.1 3-D Reconstruction Algorithm for Swept-frequency PTW Imaging**

The 3-D reconstruction algorithm employed in swept-frequency PTW imaging (Chapter 4) is a direct reconstruction from a stack of PTW amplitude/phase image slices from high to low frequencies (i.e., 5-0.04 Hz). However, because each slice contains chromophore information from slices above (higher frequencies than the current slice), a “layer stripping” algorithm may need to be applied to eliminate the effect from overlying layers, which will be able to provide a more accurate depiction of 3-D distributions of chromophores.

### **8.2.2 Optimization of Imaging Contrast Agent**

Nanorose has been utilized as a contrast agent for TPLM to target macrophages. Nanorose specificity is achieved since endogenous fluorescence emission (at 800 nm excitation) of collagen, elastin fibers, oxidized-LDL, calcification and lipid are all below 650 nm while TPL emission of nanorose is broad and emission intensity increases beyond this wavelength. To optimize TPL emission in response to an 800 nm excitation wavelength, new nanoroses (more precisely, gold nanoparticle cluster) with different geometries (Figure 8.1) need to be tested to determine the cluster formulation with brightest average TPL signals.

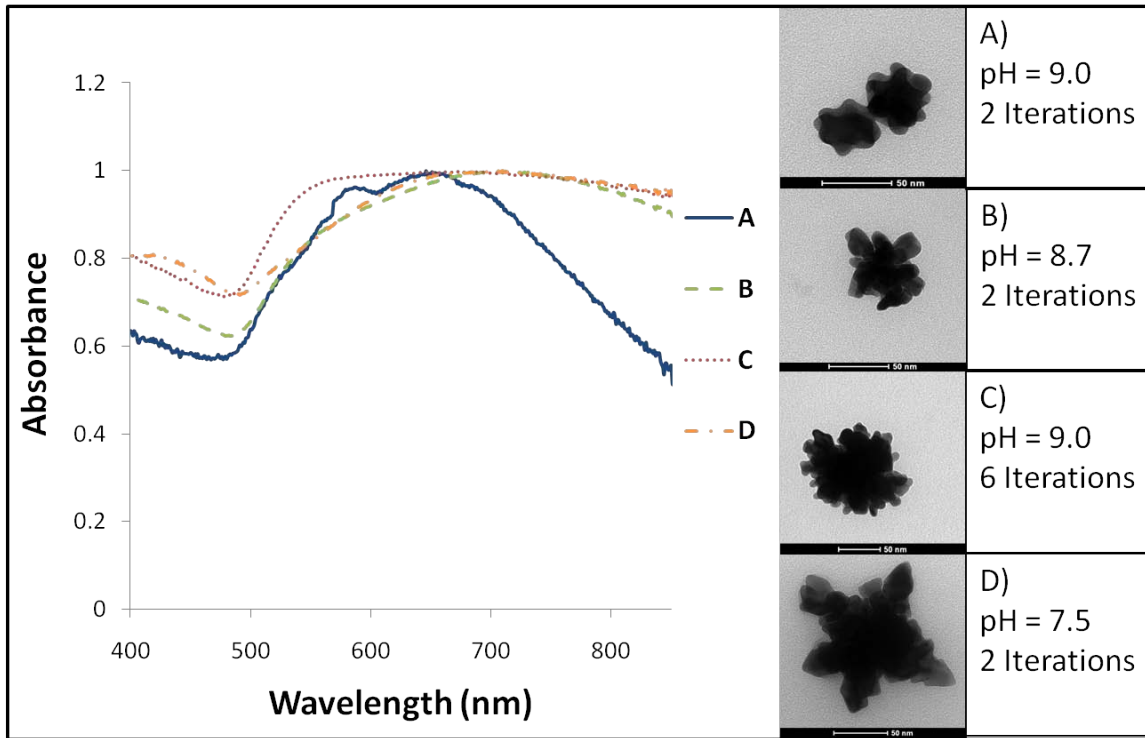


Figure 8.1. Nanorose geometries (imaged by TEM) for optimizing two-photon absorption and luminescence. Scale Bar: 50 nm.

### 8.2.3 Realization of Intravascular Imaging of Atherosclerotic Plaques

The vulnerable plaque, recently defined by Virmani as “thin-cap fibroatheroma”, results from inflammation and is characterized as having a thin fibrous cap typically less than 65  $\mu\text{m}$  thick, increased infiltration of macrophages with decreased smooth muscle cells, and an increased lipid core size compared to stable plaques.

Intravascular OCT (IVOCT) is a recently developed catheter-based method for high-resolution intravascular imaging. Currently, of all cardiovascular imaging modalities, IVOCT is the sole approach that provides sufficient spatial resolution to image thin-cap fibroatheromas. Thomas Milner, PhD and colleagues have constructed an IVOCT system with an OCT catheter for imaging human coronary arteries. Thin-cap fibroatheromas overlying large lipid cores can be identified (Figure 8.2).

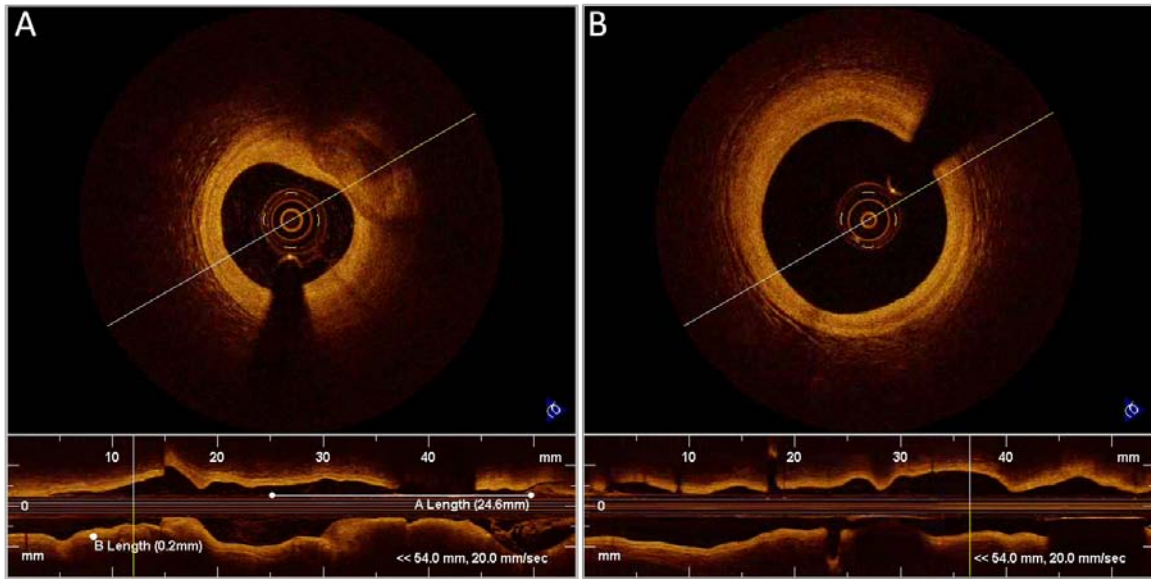


Figure 8.2. IVOCT images of a cross-section of a human coronary artery. (A) Thin-cap fibroatheroma overlying a large lipid core is observed at the 1:00-3:00 O'Clock position. (B) A healthy coronary artery. Reconstructed side view of the artery along the white line during a pullback is shown at the bottom of (A) and (B).

However, risk of plaque rupture cannot be easily assessed by only IVOCT because of the difficulties to distinguish macrophages from lipids and other plaque components such as crystals of cholesterol esters and microcalcifications due to poor scattering contrast between them. Therefore, further studies to combine IVOCT with TPL imaging and design a co-registered OCT-TPL imaging catheter to simultaneously image thin-cap fibroatheromas and macrophages (having taken up gold nanoparticles) with high spatial resolution will have decided advantages over IVOCT alone and will provide cardiologists important information about the vulnerability of thin-cap fibroatheromas.

## Bibliography

- [1] Yusuf S, Reddy S, Ounpuu S, Anand S, "Global burden of cardiovascular diseases: part I: general considerations, the epidemiologic transition, risk factors, and impact of urbanization," *Circulation* 104, 2746-2753 (2001)
- [2] Roger VL, Go AS, Lloyd-Jones DM, Adams RJ, Berry JD, Brown TM, Carnethon MR, Dai S, de Simone G, Ford ES, Fox CS, Fullerton HJ, Gillespie C, Greenlund KJ, Hailpern SM, Heit JA, Ho PM, Howard VJ, Kissela BM, Kittner SJ, Lackland DT, Lichtman JH, Lisabeth LD, Makuc DM, Marcus GM, Marelli A, Matchar DB, McDermott MM, Meigs JB, Moy CS, Mozaffarian D, Mussolino ME, Nichol G, Paynter NP, Rosamond WD, Sorlie PD, Stafford RS, Turan TN, Turner MB, Wong ND, Wylie-Rosett J, "Heart disease and stroke statistics - 2011 update : a report from the American Heart Association," *Circulation* 123, e18-e209 (2011)
- [3] Lloyd-Jones D, Adams RJ, Brown TM, Carnethon M, Dai S, De Simone G, Ferguson TB, Ford E, Furie K, Gillespie C, Go A, Greenlund K, Haase N, Hailpern S, Ho PM, Howard V, Kissela B, Kittner S, Lackland D, Lisabeth L, Marelli A, McDermott MM, Meigs J, Mozaffarian D, Mussolino M, Nichol G, Roger VL, Rosamond W, Sacco R, Sorlie P, Stafford R, Thom T, Wasserthiel-Smoller S, Wong ND, Wylie-Rosett J, "Heart disease and stroke statistics - 2010 update : a report from the American Heart Association," *Circulation* 121, e46-e215 (2010)
- [4] Stary HC, Chandler AB, Dinsmore RE, Fuster V, Glagov S, Insull W Jr, Rosenfeld ME, Schwartz CJ, Wagner WD, Wissler RW, "A definition of advanced types of atherosclerotic lesions and a histological classification of atherosclerosis. A report from the Committee on Vascular Lesions of the Council on Arteriosclerosis, American Heart Association," *Circulation*, 92(5), 1355-74 (1995)

- [5] Heart disease and stroke statistics - 2008 update, American Heart Association, Available at [http://www.americanheart.org/downloadable/heart/1200078608862HS\\_Stats%202008.final.pdf](http://www.americanheart.org/downloadable/heart/1200078608862HS_Stats%202008.final.pdf)
- [6] Zheng ZJ, Croft JB, Giles WH, Mensah GA, "Sudden cardiac death in the United States, 1989 to 1998," *Circulation* 104, 2158-2163 (2001)
- [7] Johnson JL, George SJ, Newby AC, Jackson CL, "Divergent effects of matrix metalloproteinases 3, 7, 9, and 12 on atherosclerotic plaque stability in mouse brachiocephalic arteries," *Proc Natl Acad Sci* 102, 15575-15580 (2005)
- [8] Henney AM, Wakeley PR, Davies MJ, Foster K, Hembry R, Murphy G, Humphries S, "Localization of stromelysin gene expression in atherosclerotic plaques by in situ hybridization," *Proc Natl Acad Sci* 88, 8154-8158 (1991)
- [9] Galis ZS, Sukhova GK, Lark MW, Libby P, "Increased expression of matrix metalloproteinases and matrix degrading activity in vulnerable regions of human atherosclerotic plaques," *J Clin Invest* 94, 2493-2503 (1994)
- [10] Nikkari ST, O'Brien KD, Ferguson M, Hatsukami T, Welgus HG, Alpers CE, Clowes AW, "Interstitial collagenase (MMP-1) expression in human carotid atherosclerosis," *Circulation* 92,1393-1398 (1995)
- [11] Libby P, Geng YJ, Aikawa M, Schoenbeck U, Mach F, Clinton SK, Sukhova GK, Lee, RT, "Macrophages and atherosclerotic plaque stability," *Curr Opin Lipidol* 7, 330-335 (1996)
- [12] Taubman MB, Fallon JT, Schechter AD, Giesen P, Mendlowitz M, Fyfe BS, Marmur JD, Nemerson Y, "Tissue factor in the pathogenesis of atherosclerosis," *Thromb Haemost* 78, 200-204 (1997)



- [13] Kolodgie FD, Virmani R, Burke AP, Farb A, Weber DK, Kutys R, Finn AV, Gold HK, "Pathologic assessment of the vulnerable human coronary plaque," *Heart* 90, 1385-1391 (2004)
- [14] Trivedi RA, Mallawarachi C, U-King-Im JM, Graves MJ, Horsley J, Goddard MJ, Brown A, Wang L, Kirkpatrick PJ, Brown J, Gillard JH, "Identifying inflamed carotid plaques using in vivo USPIO-enhanced MR imaging to label plaque macrophages," *Arterioscler Thromb Vasc Biol* 26, 1601-1606 (2006)
- [15] Hyafil F, Cornily J, Feig JE, Gordon R, Vucic E, Amirbekian V, Fisher EA, Fuster V, Feldman LJ, Fayad ZA, "Noninvasive detection of macrophages using a nanoparticulate contrast agent for computed tomography," *Nat Med* 13(5), 636-641 (2007)
- [16] Tawakol A, Migrino RQ, Bashian GG, Bedri S, Vermylen D, Cury RC, Yates D, LaMuraglia GM, Furie K, Houser S, Gewirtz H, Muller JE, Brady TJ, Fischman AJ, "In vivo <sup>18</sup>F-fluorodeoxyglucose positron emission tomography imaging provides a noninvasive measure of carotid plaque inflammation in patients," *J Am Coll Cardiol* 48, 1818-1824 (2006)
- [17] Jaffer FA, Kim DE, Quinti L, Tung CH, Aikawa E, Pande AN, Kohler RH, Shi GP, Libby P, Weissleder R, "Optical visualization of cathepsin K activity in atherosclerosis with a novel, protease-activatable fluorescence sensor," *Circulation* 115, 2292-2298 (2007)
- [18] Sethuraman S, Aglyamov SR, Amirian JH, Smalling RW, Emelianov SY, "Intravascular photoacoustic imaging using an IVUS imaging catheter," *IEEE Trans Ultrason Ferroelectr Freq Control* 54, 978-986 (2007)
- [19] Tearney GJ, Yabushita H, Houser SL, Aretz HT, Jang I, Schlendorf KH, Kauffman CR, Shishkov M, Halpern EF, Bouma BE, "Quantification of macrophage content

- in atherosclerotic plaques by optical coherence tomography," *Circulation* 107, 113-119 (2003)
- [20] Maton A, (1993), *Human Biology and Health*, Cliffs E (Ed.), New Jersey: Prentice Hall, ISBN 0-13-981176-1
- [21] Global Atlas on cardiovascular disease prevention and control, World Health Organization, Available at [http://whqlibdoc.who.int/publications/2011/9789241564373\\_eng.pdf](http://whqlibdoc.who.int/publications/2011/9789241564373_eng.pdf)
- [22] Statistical fact sheet - populations, American Heart Association, Available at <http://www.americanheart.org>
- [23] Atlas of heart disease and stroke, World Health Organization (2004)
- [24] Stary HC, Chandler AB, Glagov S, Guyton JR, Insull W Jr, Rosenfeld ME, Schaffer SA, Schwartz CJ, Wagner WD, Wissler RW, "A definition of initial, fatty streak, and intermediate lesions of atherosclerosis: a report from the Committee on Vascular Lesions of the Council on Arteriosclerosis," *Circulation* 89, 2462-2478 (1994)
- [25] Libby P, Aikawa M, "Stabilization of atherosclerotic plaques: new mechanisms and clinical targets," *Nat Med* 8, 1257-1262 (2002)
- [26] Libby P, Ridker PM, Maseri A, "Inflammation and atherosclerosis," *Circulation* 105,1135-1143 (2002)
- [27] Libby P, Theroux P, "Pathophysiology of coronary artery disease," *Circulation* 111, 3481-8 (2005)
- [28] Lucas AR, Korol R, Pepine CJ, "Inflammation in atherosclerosis: some thoughts about acute coronary syndromes," *Circulation* 113, e728-732 (2006)
- [29] Javier Sanz, Zahi A. Fayad, "Imaging of atherosclerotic cardiovascular disease," *Nature* 451, 953-957 (2008)

- [30] Davies MJ, Thomas A, "Thrombosis and acute coronary-artery lesions in sudden cardiac ischemic death," *N Engl J Med* 310, 1137-1140 (1984)
- [31] Virmani R, Burke AP, Kolodgie FD, Farb A, "Pathology of the thin-cap fibroatheroma: a type of vulnerable plaque," *J Interv Cardiol* 16(3), 267-272 (2003)
- [32] Davies MJ, Richardson PD, Woolf N, Katz DR, Mann J, "Risk of thrombosis in human atherosclerotic plaques: role of extracellular lipid, macrophage, and smooth muscle cell content," *Br Heart J* 69, 377-381 (1993)
- [33] Stary HC, Chandler AB, Dinsmore RE, "A definition of advanced types of atherosclerotic lesions and a histological classification of atherosclerosis: a report from the Committee on Vascular Lesions of the Council on Arteriosclerosis," *Circulation* 92, 1355-1374 (1995)
- [34] Jonasson L, Holm J, Skalli O, Bondjers G, Hansson GK, "Regional accumulations of T cells, macrophages, and smooth muscle cells in the human atherosclerotic plaque," *Arteriosclerosis* 6, 131-138 (1986)
- [35] Skalen K, Gustafsson M, Rydberg EK, Hultén LM, Wiklunda O, Innerarity TL, Borén J, "Subendothelial retention of atherogenic lipoproteins in early atherosclerosis," *Nature* 417, 750-754 (2002)
- [36] Leitinger N, "Oxidized phospholipids as modulators of inflammation in atherosclerosis," *Curr Opin Lipidol* 14, 421-430 (2003)
- [37] Eriksson EE, Xie X, Werr J, Thoren P, Lindbom L, "Importance of primary capture and L-selectin-dependent secondary capture in leukocyte accumulation in inflammation and atherosclerosis in vivo," *J Exp Med* 194, 205-218 (2001)
- [38] Kinlay S, Libby P, Ganz P, "Endothelial function and coronary artery disease," *Curr Opin Lipidol* 12, 383-389 (2001)

- [39] Cybulsky MI, Iiyama K, Li H, Zhu S, Chen M, Liyama M, Davis V, Gutierrez-Ramos JC, Connelly PW, Milstone DS, "A major role for VCAM-1, but not ICAM-1, in early atherosclerosis," *J Clin Invest* 107, 1255-1262 (2001)
- [40] Smith JD, Trogan E, Ginsberg M, Grigaux C, Tian J, Miyata M, "Decreased atherosclerosis in mice deficient in both macrophage colony-stimulating factor (op) and apolipoprotein E," *Proc Natl Acad Sci* 92, 8264-8268 (1995)
- [41] Boring L, Gosling J, Cleary M, Charo IF, "Decreased lesion formation in CCR2<sup>-/-</sup> mice reveals a role for chemokines in the initiation of atherosclerosis," *Nature* 394, 894-897 (1998)
- [42] Gu L, Okada Y, Clinton SK, Gerard C, Sukhova GK, Libby P, Rollins BJ, "Absence of monocyte chemoattractant protein-1 reduces atherosclerosis in low density lipoprotein receptor-deficient mice," *Mol Cell* 2, 275-281 (1998)
- [43] Fukumoto Y, Libby P, Rabkin E, Hill CC, Enomoto M, Hirouchi Y, Shiomi M, Aikawa M, "Statins alter smooth muscle cell accumulation and collagen content in established atheroma of watanabe heritable hyperlipidemic rabbits," *Circulation* 103, 993-999 (2001)
- [44] van der Wal AC, Becker AE, van der Loos CM, Das PK, "Site of intimal rupture or erosion of thrombosed coronary atherosclerotic plaques is characterized by an inflammatory process irrespective of the dominant plaque morphology," *Circulation* 89, 36-44 (1994)
- [45] Viles-Gonzalez JF, Poon M, Sanz J, Rius T, Nikolaou K, Fayad ZA, Fuster V, Badimon JJ, "In vivo 16-slice, multidetector-row computed tomography for the assessment of experimental atherosclerosis: comparison with magnetic resonance imaging and histopathology," *Circulation* 110, 1467-1472 (2004)

- [46] Khera A, de Lemos JA, Peshock RM, Lo HS, Stanek HG, Murphy SA, Wians FH Jr, Grundy SM, McGuire DK, "Relationship between C-reactive protein and subclinical atherosclerosis: the Dallas Heart Study," *Circulation* 113, 38-43 (2006)
- [47] Nahrendorf M, Jaffer FA, Kelly KA, Sosnovik DE, Aikawa E, Libby P, Weissleder R, "Noninvasive vascular cell adhesion molecule-1 imaging identifies inflammatory activation of cells in atherosclerosis," *Circulation* 114, 1504-1511 (2006)
- [48] Amirbekian V, Lipinski MJ, Briley-Saebo KC, Amirbekian S, Aguinaldo JGS, Weinreb DB, Vucic E, Frias JC, Hyafil F, Mani V, Fisher EA, Fayad ZA, "Detecting and assessing macrophages in vivo to evaluate atherosclerosis noninvasively using molecular MRI," *Proc Natl Acad Sci* 104, 961-966 (2007)
- [49] Okane K, Ibaraki M, Toyoshima H, Sugawara S, Takahashi K, Miura S, Shimosegawa E, Satomi J, Kitamura K, Satoh T, "<sup>18</sup>F-FDG accumulation in atherosclerosis: use of CT and MR co-registration of thoracic and carotid arteries," *Eur J Nucl Med Mol Imaging* 33, 589-594 (2006)
- [50] Nahrendorf M, Zhang H, Hembrador S, Panizzi P, Sosnovik DE, Aikawa E, Libby P, Swirski FK, Weissleder R, "Nanoparticle PET-CT imaging of macrophages in inflammatory atherosclerosis," *Circulation* 117, 379-387 (2008)
- [51] Kircher MF, Grimm J, Swirski FK, Libby P, Gerszten RE, Allport JR, Weissleder R, "Noninvasive in vivo imaging of monocyte trafficking to atherosclerotic lesions," *Circulation* 117, 388-395 (2008)
- [52] Nair A, Kuban BD, Obuchowski N, Vince DG, "Assessing spectral algorithms to predict atherosclerotic plaque composition with normalized and raw intravascular ultrasound data," *Ultrasound Med Biol* 27, 1319-1331 (2001)
- [53] Kenya N, Etsuo T, Osamu K, Vince DG, Renu V, Jean-Francois S, Akira M, Yoshihiro T, Tatsuya I, Mariko E, Tetsuo M, Mitsuyasu T, Takahiko S, "Accuracy

of in vivo coronary plaque morphology assessment: a validation study of in vivo virtual histology compared with in vitro histopathology," *J Am Coll Cardiol* 47, 2405-2412 (2006)

- [54] Wang B, Yantsen E, Larson T, Karpouk AB, Sethuraman S, Su JL, Sokolov K, Emelianov SY, "Plasmonic intravascular photoacoustic imaging for detection of macrophages in atherosclerotic plaques," *Nano Lett* 9(6), 2212-7 (2009)
- [55] Phipps JE, Hatami N, Galis ZS, Baker JD, Fishbein MC, Marcu L, "A fluorescence lifetime spectroscopy study of matrix metalloproteinases-2 and -9 in human atherosclerotic plaque," *J Biophotonics* 4, 650-658 (2011)
- [56] Brezinski ME, Tearney GJ, Bouma BE, Boppart SA, Hee MR, Swanson EA, Southern JF, Fujimoto JG, "Imaging of coronary artery microstructure (in vitro) with optical coherence tomography," *Am J Cardiol* 77, 92-93 (1996)
- [57] Raffel OC, Tearney GJ, Gauthier DD, Halpern EF, Bouma BE, Jang IK, "Relationship between a systemic inflammatory markers, plaque inflammation, and plaque characteristics determined by intravascular optical coherence tomography," *Arterioscler Thromb Vasc Biol* 27, 1820-1827 (2007)
- [58] Tanaka A, Imanishi T, Kitabata H, Kubo T, Takarada S, Tanimoto T, Kuroi A, Tsujioka H, Ikejima H, Ueno S, Kataiwa H, Okouchi K, Kashiwagi M, Matsumoto H, Takemoto K, Nakamura N, Hirata K, Mizukoshi M, Akasaka T, "Morphology of exertion-triggered plaque rupture in patients with acute coronary syndrome: an optical coherence tomography study," *Circulation* 118, 2368-2373 (2008)
- [59] Vancraeynest D, Pasquet A, Roelants V, Gerber BL, Vanoverschelde JJ, "Imaging the vulnerable plaque," *J Am Coll Cardiol* 57, 1961-1979 (2011)

- [60] van Zandvoort M, Engels W, Douma K, Beckers L, oude Egbrink M, Daemen M, Slaaf DW, "Two-photon microscopy for imaging of the (atherosclerotic) vascular wall: a proof of concept study," *J Vasc Res* 41, 54-63 (2004)
- [61] Zoumi A, Lu XA, Kassab GS, Tromberg BJ, "Imaging coronary artery microstructure using secondharmonic and two-photon fluorescence microscopy," *Biophys J* 87, 2778-2786 (2004)
- [62] Boulesteix T, Pena AM, Pages N, Godeau G, Sauviat MP, Beaurepaire E, Schanne-Klein MC, "Micrometer scale ex vivo multiphoton imaging of unstained arterial wall structure," *Cytometry Part A* 69A, 20-26 (2006)
- [63] Le TT, Langohr IM, Locker MJ, Sturek M, Cheng JX, "Label-free molecular imaging of atherosclerotic lesions using multimodal nonlinear optical microscopy," *J Biomed Opt* 12(5), 0540071-05400710 (2007)
- [64] Lilledahl MB, Haugen OA, de Lange Davies C, Svaasand LO, "Characterization of vulnerable plaques by multiphoton microscopy," *J Biomed Opt* 12(4), 0440051-04400512 (2007)
- [65] Badea C, Hedlund LW, Johnson GA, "Micro-CT with respiratory and cardiac gating," *Med Phys* 31(12), 3324-3329 (2004)
- [66] Wasserman BA, Astor BC, Sharrett AR, Swingen C, Catellier D, "MRI measurements of carotid plaque in the atherosclerosis risk in communities (ARIC) study: Methods, reliability and descriptive statistics," *J Magn Reson Imaging* 31, 406-415 (2010)
- [67] Baird AE, Donnan GA, Austin MC, Fitt GJ, Davis SM, McKay WJ, "Reperfusion after thrombolytic therapy in ischemic stroke measured by single-photon emission computed tomography," *Stroke* 25, 79-85 (1994)

- [68] Karpouk AB, Wang B, Emelianov SY, "Development of a catheter for combined intravascular ultrasound and photoacoustic imaging," *Rev Sci Instrum* 81(1), 014901-014907 (2010)
- [69] Park J, Jo JA, Shrestha S, Pande P, Wan Q, Applegate BE, "A dual-modality optical coherence tomography and fluorescence lifetime imaging microscopy system for simultaneous morphological and biochemical tissue characterization," *Biomed Opt Express* 2 (1), 186-200 (2010)
- [70] Wang T , Mancuso JJ, Sapozhnikova V, Dwelle J, Ma LL, Willsey B, Kazmi SM, Qiu J, Li X, Asmis R, Johnston KP, Feldman MD, Milner TE, "Dual-wavelength multi-frequency PTW imaging combined with OCT for macrophage and lipid detection in atherosclerotic plaques", *J Biomed Opt* (IN PRESS)
- [71] Wang HW, Langohr IM, Sturek M, Cheng JX, "Imaging and quantitative analysis of atherosclerotic lesions by CARS-based multimodal nonlinear optical microscopy," *Arterioscler Thromb Vasc Biol* 29, 1342-1348 (2009)
- [72] The Trials of Hypertension Prevention Collaborative Research Group, "Effects of weight loss and sodium reduction intervention on blood pressure and hypertension incidence in overweight people with high-normal blood pressure, The Trials of Hypertension Prevention, phase II," *Arch Intern Med* 157, 657-67 (1997)
- [73] He J, Whelton PK, Appel LJ, Charleston J, Klag MJ, "Long-term effects of weight loss and dietary sodium reduction on incidence of hypertension," *Hypertension* 35, 544-549 (2000)
- [74] Sacks FM, Svetkey LP, Vollmer WM, Appel LJ, Bray GA, Harsha D, Obarzanek E, Conlin PR, Miller ER III, Simons-Morton DG, Karanja N, Lin PH, DASH-Sodium Collaborative Research Group, "Effects on blood pressure of reduced dietary



- sodium and the Dietary Approaches to Stop Hypertension (DASH) diet," *N Engl J Med* 344, 3-10 (2001)
- [75] Vollmer WM, Sacks FM, Ard J, Appel LJ, Bray GA, Simons-Morton DG, Conlin PR, Svetkey LP, Erlinger TP, Moore TJ, Karanja N, "Effects of diet and sodium intake on blood pressure: subgroup analysis of the DASH-sodium trial," *Ann Intern Med* 135, 1019-1028 (2001)
- [76] Chobanian AV, Hill M, National Heart, Lung, and Blood Institute, "Workshop on sodium and blood pressure: a critical review of current scientific evidence," *Hypertension* 35, 858-863 (2000)
- [77] Kelley GA, Kelley KS, "Progressive resistance exercise and resting blood pressure: a meta-analysis of randomized controlled trials," *Hypertension* 35, 838-843 (2000)
- [78] Whelton SP, Chin A, Xin X, He J, "Effect of aerobic exercise on blood pressure: a meta-analysis of randomized, controlled trials," *Ann Intern Med* 136, 493-503 (2002)
- [79] Xin X, He J, Frontini MG, Ogden LG, Motsamai OI, Whelton PK, "Effects of alcohol reduction on blood pressure: a meta-analysis of randomized controlled trials," *Hypertension* 38, 1112-1117 (2001)
- [80] Executive summary of the Third Report of the National Cholesterol Education Program (NCEP) Expert Panel on Detection, Evaluation, and Treatment of High Blood Cholesterol in Adults (Adult Treatment Panel III), National Heart, Lung, and Blood Institute, Available at <http://www.nhlbi.nih.gov/guidelines/cholesterol/atp3xsum.pdf> (Accessed Jan 10, 2011)
- [81] 4S Group, "Randomised trial of cholesterol lowering in 4444 patients with coronary heart disease: the Scandinavian Simvastatin Survival Study (4S)," *Lancet* 344, 1383-1389 (1994)

- [82] Shepherd J, Cobbe SM, Ford I, Isles CG, Lorimer AR, MacFarlane PW, McKillop JH, Packard CJ, "Prevention of coronary heart disease with pravastatin in men with hypercholesterolemia. West of Scotland Coronary Prevention Study Group," *N Engl J Med* 333, 1301-1307 (1995)
- [83] Sacks FM, Pfeffer MA, Moye LA, Rouleau JL, Rutherford JD, Cole TG, Brown L, Warnica JW, Arnold JM, Wun CC, Davis BR, Braunwald E, "The effect of pravastatin on coronary events after myocardial infarction in patients with average cholesterol levels. Cholesterol and Recurrent Events Trial Investigators," *N Engl J Med* 335, 1001-1009 (1996)
- [84] Downs JR, Clearfield M, Weis S, Whitney E, Shapiro DR, Beere PA, Langendorfer A, Stein EA, Kruyer W, Gotto AM Jr, "Primary prevention of acute coronary events with lovastatin in men and women with average cholesterol levels: results of AFCAPS/TexCAPS: Air Force/Texas Coronary Atherosclerosis Prevention Study," *JAMA* 279, 1615-1622 (1998)
- [85] Atherosclerosis, National Heart, Lung, and Blood Institute, Available at [http://www.nhlbi.nih.gov/health/dci/Diseases/Atherosclerosis/Atherosclerosis\\_All.html](http://www.nhlbi.nih.gov/health/dci/Diseases/Atherosclerosis/Atherosclerosis_All.html) (Accessed Jan 10, 2011)
- [86] Ellis SG, Omoigui N, Bittl JA, Lincoff M, Wolfe MW, Howell G, Topol EJ, "Analysis and comparison of operator-specific outcomes in interventional cardiology: from a multicenter database of 4860 quality-controlled procedures," *Circulation* 93, 431-439 (1996)
- [87] Wolfe MW, Roubin GS, Schweiger M, Isner JM, Ferguson JJ, Cannon AD, Cleman M, Cabin H, Leya F, Bonan R, "Length of hospital stay and complications after percutaneous transluminal coronary angioplasty: clinical and procedural predictors," *Circulation* 92, 311-319 (1995)

- [88] Topol EJ, Leya F, Pinkerton CA, Whitlow PL, Hofling B, Simonton CA, Masden RR, Serruys PW, Leon MB, Williams DO, "A comparison of directional atherectomy with coronary angioplasty in patients with coronary artery disease," *N Engl J Med* 329, 221-227 (1993)
- [89] Adelman AG, Cohen EA, Kimball BP, Bonan R, Ricci DR, Webb JG, Laramee L, Barbeau G, Traboulsi M, Corbett BN, "A comparison of directional atherectomy with balloon angioplasty for lesions of the left anterior descending coronary artery," *N Engl J Med* 329, 228-233 (1993)
- [90] Nobuyoshi M, Kimura T, Nosaka H, Mioka S, Ueno K, Yokoi H, Hamasaki N, Horiuchi H, Ohishi H, "Restenosis after successful percutaneous transluminal coronary angioplasty: serial angiographic follow-up of 229 patients," *J Am Coll Cardiol* 12, 616-623 (1988)
- [91] Serruys PW, de Jaegere P, Kiemeneij F, Macaya C, Rutsch W, Heyndrickx G, Emanuelsson H, Marco J, Legrand V, Materne P, "A comparison of balloon-expandable-stent implantation with balloon angioplasty in patients with coronary artery disease," *N Engl J Med* 331, 489-495 (1994)
- [92] Fischman DL, Leon MB, Baim DS, Schatz RA, Savage MP, Penn I, Detre K, Veltri L, Ricci D, Nobuyoshi M, "A randomized comparison of coronary-stent placement and balloon angioplasty in the treatment of coronary artery disease," *N Engl J Med* 331, 496-501 (1994)
- [93] Nissen SE, "The vulnerable plaque "hypothesis"- promise, but little progress," *JACC: Cardiovascular Imaging* 2(4), 483-485 (2009)
- [94] Briley-Saebo KC, Mulder WJ, Mani V, Hyafil F, Amirbekian V, Aguinaldo JG, Fisher EA, Fayad ZA, "Magnetic resonance imaging of vulnerable atherosclerotic

- plaques: current imaging strategies and molecular imaging probes," *J Magn Reson Imaging* 26, 460–479 (2007)
- [95] Wu JC, Bengel FM, Gambhir SS, "Cardiovascular molecular imaging," *Radiology* 244, 337-355 (2007)
- [96] Jaffer FA, Libby P, Weissleder R, "Molecular imaging of cardiovascular disease," *Circulation* 116, 1052-1061 (2007)
- [97] Sosnovik DE, Nahrendorf M, Weissleder R, "Molecular magnetic resonance imaging in cardiovascular medicine," *Circulation* 115, 2076-2086 (2007)
- [98] Cai W, Chen X, "Nanoplatfoms for targeted molecular imaging in living subjects," *Small* 3, 1840-1854 (2007)
- [99] Caruthers SD, Wickline SA, Lanza GM, "Nanotechnological applications in medicine," *Curr Opin Biotechnol* 18(1), 26-30 (2007)
- [100] Annovazzi A, Bonanno E, Arca M, D'Alessandria C, Marcoccia A, Spagnoli LG, Violi F, Scopinaro F, De Toma G, Signore A, "<sup>99m</sup>Tc-interleukin-2 scintigraphy for the in vivo imaging of vulnerable atherosclerotic plaques," *Eur J Nucl Med Mol Imaging* 33(2), 117-126 (2006)
- [101] Jaffer FA, Vinegoni C, John MC, Aikawa E, Gold HK, Finn AV, Ntziachristos V, Libby P, Weissleder R, "Real-time catheter molecular sensing of inflammation in proteolytically active atherosclerosis," *Circulation* 118(18), 1802-1809 (2008)
- [102] Smith BR, Heverhagen J, Knopp M, Schmalbrock P, Shapiro J, Shiomi M, Moldovan NI, Ferrari M, Lee SC, "Localization to atherosclerotic plaque and biodistribution of biochemically derivatized superparamagnetic iron oxide nanoparticles (SPIONs) contrast particles for magnetic resonance imaging (MRI)," *Biomed Microdevices* 9(5), 719-727 (2007)

- [103] Kolodgie FD, Petrov A, Virmani R, Narula N, Verjans JW, Weber DK, Hartung D, Steinmetz N, Vanderheyden JL, Vannan MA, Gold HK, Reutelingsperger CP, Hofstra L, Narula J, "Targeting of apoptotic macrophages and experimental atheroma with radiolabeled annexin V: a technique with potential for noninvasive imaging of vulnerable plaque," *Circulation* 108(25), 3134-3139 (2003)
- [104] McAteer MA, Sibson NR, von Zur Muhlen C, Schneider JE, Lowe AS, Warrick N, Channon KM, Anthony DC, Choudhury RP, "In vivo magnetic resonance imaging of acute brain inflammation using microparticles of iron oxide," *Nat Med* 13(10), 1253-1258 (2007)
- [105] Broisat A, Riou LM, Ardisson V, Boturyn D, Dumy P, Fagret D, Ghezzi C, "Molecular imaging of vascular cell adhesion molecule-1 expression in experimental atherosclerotic plaques with radiolabelled B2702-p," *Eur J Nucl Med Mol Imaging* 34(6), 830-840 (2007)
- [106] Villanueva FS, Lu E, Bowry S, Kilic S, Tom E, Wang J, Gretton J, Pacella JJ, Wagner WR, "Myocardial ischemic memory imaging with molecular echocardiography," *Circulation* 115, 345-352 (2007)
- [107] Meding J, Urich M, Licha K, Reinhardt M, Misselwitz B, Fayad ZA, Weinmann HJ, "Magnetic resonance imaging of atherosclerosis by targeting extracellular matrix deposition with Gadofluorine M," *Contrast Media Mol Imaging* 2(3), 120-129 (2007)
- [108] Megens RT, Oude Egbrink MG, Cleutjens JP, Kuijpers MJ, Schiffers PH, Merkx M, Slaaf DW, van Zandvoort MA, "Imaging collagen in intact viable healthy and atherosclerotic arteries using fluorescently labeled CNA35 and two-photon laser scanning microscopy," *Mol Imaging* 6(4), 247-260 (2007)

- [109]Frias JC, Williams KJ, Fisher EA, Fayad ZA, "Recombinant HDL-like nanoparticles: a specific contrast agent for MRI of atherosclerotic plaques," *J Am Chem Soc* 126(50), 16316-16317 (2004)
- [110]Riou LM, Broisat A, Dimastromatteo J, Pons G, Fagret D, Ghezzi, "Pre-clinical and clinical evaluation of nuclear tracers for the molecular imaging of vulnerable atherosclerosis: an overview," *Curr Med Chem* 16(12), 1499-1511 (2009)
- [111]Winter PM, Neubauer AM, Caruthers SD, Harris TD, Robertson JD, Williams TA, Schmieder AH, Hu G, Allen JS, Lacy EK, Zhang H, Wickline SA, Lanza GM, "Endothelial  $\alpha v \beta 3$  integrin-targeted fumagillin nanoparticles inhibit angiogenesis in atherosclerosis," *Arterioscler Thromb Vasc Biol* 26, 2103-2109 (2006)
- [112]Backer MV, Levashova Z, Patel V, Jehning BT, Claffey K, Blankenberg FG, Backer JM, "Molecular imaging of VEGF receptors in angiogenic vasculature with single-chain VEGF-based probes," *Nat Med* 13(4), 504-509 (2007)
- [113]Botnar RM, Perez AS, Witte S, Wiethoff AJ, Laredo J, Hamilton J, Quist W, Parsons EC Jr, Vaidya A, Kolodziej A, Barrett JA, Graham PB, Weisskoff RM, Manning WJ, Johnstone MT, "In vivo molecular imaging of acute and subacute thrombosis using a fibrin-binding magnetic resonance imaging contrast agent," *Circulation* 109(16), 2023-2029 (2004)
- [114]Taillefer R, Edell S, Innes G, Lister-James J, "Acute thromboscintigraphy with (99m)Tc-apcitide: results of the phase 3 multicenter clinical trial comparing <sup>99m</sup>Tc-apcitide scintigraphy with contrast venography for imaging acute DVT. Multicenter Trial Investigators," *J Nucl Med* 41, 1214-1223 (2000)
- [115]Flaumenhaft R, Tanaka E, Graham GJ, De Grand AM, Laurence RG, Hoshino K, Hajjar RJ, Frangioni JV, "Localization and quantification of platelet-rich thrombi in

- large blood vessels with near-infrared fluorescence imaging," *Circulation* 115, 84-93 (2007)
- [116]Alonso A, Della Martina A, Stroick M, Fatar M, Griebe M, Pochon S, Schneider M, Hennerici M, Allémann E, Meairs S, "Molecular imaging of human thrombus with novel abciximab immunobubbles and ultrasound," *Stroke* 38(5), 1508-1514 (2007)
- [117]Ma LL, Feldman MD, Tam JM, Paranjape AS, Cheruku KK, Larson TA, Tam JO, Ingram DR, Paramita V, Villard JW, Jenkins JT, Wang T, Clarke GD, Asmis R, Sokolov K, Chandrasekar B, Milner TE, Johnston KP, "Small multifunctional nanoclusters (nanoroses) for targeted cellular imaging and therapy," *ACS Nano* 3(9), 2686-2696 (2009)
- [118]Wang T, Qiu J, Ma LL, Li X, Sun J, Ryoo S, Johnston KP, Feldman MD, Milner TE, "Nanorose and lipid detection in atherosclerotic plaque using dual-wavelength PTW imaging," *Proc. SPIE*, Vol. 7562, 75620S (2010)
- [119]Patterson MS, Wilson BC, Wyman DR, "The propagation of optical radiation in tissue. II: optical properties of tissues and resulting fluence distributions," *Lasers Med Sci* 6(4), 379-390(1991)
- [120]Draine BT, Flatau PJ, "User guide for the discrete dipole approximation code DDSCAT 7.0 (2008)," Available at <http://arxiv.org/abs/0809.0337>
- [121]Jain PK, Eustis S, El-Sayed MA, "Plasmon coupling in nanorod assemblies: optical absorption, discrete dipole approximation simulation, and exciton-coupling model," *J Phys Chem B* 110, 18243-18253 (2006)
- [122]Mornet S, Vasseur S, Grasset F, Duguet E, "Magnetic nanoparticle design for medical diagnosis and therapy," *J Mat Chem* 14, 2161-2175 (2004)
- [123]Jacques S, Optical properties spectra, Available at: <http://omlc.ogi.edu/spectra>

- [124] Anderson RR, Farinelli W, Laubach H, Manstein D, Yaroslavsky AN, Gubeli III J, Jordan K, Neil GR, Shinn M, Chandler W, Williams GP, Benson SV, Douglas DR, Dylla HF, "Selective photothermolysis of lipid-rich tissues: A free electron laser study," *Lasers Surg Med* 38(10), 913-919 (2006)
- [125] Mulaveesala R, Tuli S, "Theory of frequency modulated thermal wave imaging for nondestructive subsurface defect detection," *Appl Phys Lett* 89, 191-193 (2006)
- [126] Mandelis A, "Green's functions in thermal-wave physics: Cartesian coordinate representations," *J Appl Phys* 78(2), 647-655 (1995)
- [127] Roeder J, Birngruber R, (1995), "Solution of the heat conduction equation," Welch AJ, van Gemert MJC (Eds), 386-390, New York: Plenum Press
- [128] Cotran RS, Kumar V, Collins T, Robbins SL, "Robbins pathologic basis of disease," Saunders, The University of Michigan, 523-524 (1999)
- [129] Yoshimura K, Esato K, Fujioka K, "Effects of nilvadipine, a calcium antagonist, on intimal thickness of vascular grafting in cholesterol-fed rabbits," *Int J Angiology* 5(1), 8-14 (1996)
- [130] ten Have AG, Gijzen FJH, Wentzel JJ, Slager CJ, van der Steen AFW, "Temperature distribution in atherosclerotic coronary arteries: influence of plaque geometry and flow (a numerical study)," *Phys Med Biol* 49, 4447-4462 (2004)
- [131] Kzhyshkowska J, Krusell L, "Cross-talk between endocytic clearance and secretion in macrophages," *Immunobiology* 214(7), 576-593 (2009)
- [132] Telenkov SA, Vargas G, Nelson JS, Milner TE, "Coherent thermal wave imaging of subsurface chromophores in biological materials," *Phys Med Biol* 47, 657-671 (2002)
- [133] Somersalo E, Cheney M, Isaacson D, Isaacson E, "Layer stripping: a direct numerical method for impedance imaging," *Inverse Prob* 7(6), 899-926 (1991)



- [134] American Heart Association, Available at <http://www.americanheart.org/presenter.jhtml?identifier=3038611>
- [135] American Heart Association, Available at <http://www.americanheart.org/presenter.jhtml?identifier=4478>
- [136] Pasterkamp G, Falk E, Woutman H, Borst C, "Techniques characterizing the coronary atherosclerotic plaque: influence on clinical decision making?," *J Am Coll Cardiol* 36, 13-21 (2000)
- [137] Virmani R, Kolodgie FD, Burke AP, Farb A, Schwartz M, "Lessons from sudden coronary death. A comprehensive morphological classification scheme for atherosclerotic lesions," *Arterioscler Thromb Vasc Biol* 20, 1262-1275 (2000)
- [138] Galis ZS, Sukhova GK, Kranzhofer R, Clark S, Libby P, "Macrophage foam cells from experimental atheroma constitutively produce matrix-degrading proteinases," *Proc Natl Acad Sci* 92(2), 402-406 (1995)
- [139] Falk E, Shah PK, Fuster V, "Coronary plaque disruption," *Circulation* 92(3), 657-671 (1995)
- [140] Rajadhyaksha M, Grossman M, Esterowitz D, Webb RH, Anderson RR, "In vivo confocal scanning laser microscopy of human skin: melanin provides strong contrast," *J Invest Dermatol* 104, 946-952 (1995)
- [141] Rajadhyaksha M, González S, Zavislan JM, Anderson RR, Webb RH, "In vivo confocal scanning laser microscopy of human skin II: advances in instrumentation and comparison with histology," *J Invest Dermatol* 113(3), 293-301 (1999)
- [142] Available at <http://www.biology.wustl.edu/imaging-facility/specs-leica.php>
- [143] Wang T, Qiu J, Ma LL, Li X, Sun J, Ryoo S, Johnston KP, Feldman MD, Milner TE, "Nanorose and lipid detection in atherosclerotic plaque using dual-wavelength photothermal wave imaging," *Proc SPIE* 7562, 75620S-75620S-7 (2010)

- [144] Schonbeck U, Mach F, Sukhova GK, Atkinson E, Levesque E, Herman M, Graber P, Basset P, Libby P, "Expression of stromelysin-3 in atherosclerotic lesions: regulation via CD40- CD40 ligand signaling in vitro and in vivo," *J Exp Med* 189, 843-853 (1999)
- [145] Falk E, "Pathogenesis of atherosclerosis," *J Am Coll Cardiol* 47(8 Suppl), C7-C12 (2006)
- [146] Liu L, Gardecki JA, Nadkarni SK, Toussaint JD, Yagi Y, Bouma BE, Tearney GJ, "Imaging the subcellular structure of human coronary atherosclerosis using micro-optical coherence tomography," *Nat Med* 17(8), 1010-1014 (2011)
- [147] Rosencwaig A, "Thermal-wave imaging," *Science* 218(4569), 223-228 (1982)
- [148] Thomas RL, Favro LD, Kuo PK, "Thermal-wave imaging for nondestructive evaluation," *Can J Phys* 64, 1234-1237 (1986)
- [149] Mandelis A, Williams A, Siu EKM, "Photothermal wave imaging of metal-oxide-semiconductor field-effect transistor structures," *J Appl Phys* 63(1), 92-98 (1988)
- [150] Busse G, Dewhurst RJ, Nikoonahad M, Scruby CB, "Imaging with optically generated thermal waves," *Phil Trans R Soc Lond A* 320, 181-186 (1986)
- [151] Tsai CL, Chen JC, Wang WJ, "Near-infrared absorption property of biological soft tissue constituents," *J Med Biol Eng* 21, 7-14 (2001)
- [152] Walsh Jr JT, (1995), "Pulsed laser angioplasty: a paradigm for tissue ablation in optical-thermal response of laser-irradiated tissue," Welch AJ, van Gemert MJC (Eds), 869-874, New York: Plenum Press
- [153] Kolodgie FD, Katocs AS Jr, Largis EE, Wrenn SM, Cornhill JF, Herderick EE, Lee SJ, Virmani R, "Hypercholesterolemia in the rabbit induced by feeding graded amounts of low-level cholesterol: Methodological considerations regarding

- individual variability in response to dietary cholesterol and development of lesion type," *Arterioscler Thromb Vasc Biol* 16(12), 1454-1464 (1996)
- [154]Paranjape AS, Kuranov R, Baranov S, Ma LL, Villard JW, Wang T, Sokolov KV, Feldman MD, Johnston KP, Milner TE, "Depth resolved photothermal OCT detection of macrophages in tissue using nanorose," *Biomed Opt Exp* 1(1), 2-16 (2010)
- [155]Shaw III CF, "Gold-based therapeutic agents," *Chem Rev* 99, 2589-2600 (1999)
- [156]Park J, Estrada A, Sharp K, Sang K, Schwartz JA, Smith DK, Coleman C, Payne JD, Korgel BA, Dunn AK, Tunnell JW, "Two-photon-induced photoluminescence imaging of tumors using near-infrared excited gold nanoshells," *Opt Exp* 16(3), 1590-1599 (2008)
- [157]Yu W, Braz JC, Dutton AM, Prusakov P, Rekhter M, "In vivo imaging of atherosclerotic plaques in apolipoprotein E deficient mice using nonlinear microscopy," *J Biomed Opt* 12(5), 0540081-05400810 (2007)
- [158]Leibovich SJ, Polverini PJ, Shepard HM, Wiseman DM, Shively V, Nuseir N, "Macrophage-induced angiogenesis is mediated by tumor necrosis factor-alpha," *Nature* 329, 630-632 (1987)
- [159]Lim RS, Kratzer A, Barry NP, Miyazaki-Anzai S, Miyazaki M, Mantulin WW, Levi M, Potma EO, Tromberg BJ, "Multimodal CARS microscopy determination of the impact of diet on macrophage infiltration and lipid accumulation on plaque formation in ApoE-deficient mice," *J Lipid Res* 51, 1729-1737 (2010)
- [160]Chithrani BD, Ghazani AA, Chan WC, "Determining the size and shape dependence of gold nanoparticle uptake into mammalian cells," *Nano Lett* 6, 662-668 (2006)

- [161]Jiang W, Kim BY, Rutka JT, Chan WC, "Nanoparticle-mediated cellular response is size-dependent," *Nat Nanotech* 3, 145-150 (2008)
- [162]Owens DE III, Peppas NA, "Opsonization, biodistribution, and pharmacokinetics of polymeric nanoparticles," *Int J Pharmaceu* 307, 93-102 (2006)
- [163]Wenger Y, Schneider RJ 2nd, Reddy GR, Kopelman R, Jolliet O, Philbert MA, "Tissue distribution and pharmacokinetics of stable polyacrylamide nanoparticles following intravenous injection in the rat," *Toxicol Appl Pharmacol* 251, 181-190 (2011)
- [164]Trivedi RA, U-King-Im JM, Graves MJ, Cross JJ, Horsley J, Goddard MJ, Skepper JN, Quartey G, Warburton E, Joubert I, Wang L, Kirkpatrick PJ, Brown J, Gillard JH, "In vivo detection of macrophages in human carotid atheroma: temporal dependence of ultrasmall superparamagnetic particles of iron oxide-enhanced MRI," *Stroke* 35, 1631-1635 (2004)
- [165]Dirksen MT, van der Wal AC, van den Berg FM, van der Loos CM, Becker AE, "Distribution of inflammatory cells in atherosclerotic plaques relates to the direction of flow," *Circulation* 98(19), 2000-2003 (1998)
- [166]Slager CJ, Wentzel JJ, Gijsen FJ, Thury A, van der Wal AC, Schaar JA, Serruys PW, "The role of shear stress in the destabilization of vulnerable plaques and related therapeutic implications," *Nat Rev Cardiol* 2, 456-464 (2005)
- [167]Halpert I, Sires UI, Roby JD, Potter-Perigo S, Wight TN, Shapiro SD, Welgus HG, Wickline SA, Parks WC, "Matrilysin is expressed by lipid-laden macrophages at sites of potential rupture in atherosclerotic lesions and localizes to areas of versican deposition, a proteoglycan substrate for the enzyme," *Proc Natl Acad Sci* 93, 9748-9753 (1996)

- [168] Uzui H, Harpf A, Liu M, Doherty TM, Shukla A, Chai NN, Tripathi PV, Jovinge S, Wilkin DJ, Asotra K, Shah PK, Rajavashisth TB, "Increased expression of membrane type 3-matrix metalloproteinase in human atherosclerotic plaque: role of activated macrophages and inflammatory cytokines," *Circulation* 106, 3024-3030 (2002)
- [169] Rajagopalan S, Meng XP, Ramasamy S, Harrison DG, Galis ZS, "Reactive oxygen species produced by macrophage-derived foam cells regulate the activity of vascular matrix metalloproteinases in vitro. Implications for atherosclerotic plaque stability," *J Clin Invest* 98(11), 2572-2579 (1996)
- [170] Kovanen PT, Kaartinen M, Paavonen T, "Infiltrates of activated mast cells at the site of coronary atheromatous erosion or rupture in myocardial infarction," *Circulation* 92, 1084-1088 (1995)
- [171] Schieffer B, Schieffer E, Hilfiker-Kleiner D, Hilfiker A, Kovanen PT, Kaartinen M, Nussberger J, Harringer W, Drexler H, "Expression of angiotensin ii and interleukin 6 in human coronary atherosclerotic plaques: potential implications for inflammation and plaque instability," *Circulation* 101, 1372-1378 (2000)
- [172] Tabas I, "Macrophage apoptosis in atherosclerosis: consequences on plaque progression and the role of endoplasmic reticulum stress," *Antioxid Redox Signal* 11(9), 2333-2339 (2009)
- [173] Corot C, Petry KG, Trivedi R, Saleh A, Jonkmanns C, Le Bas JF, Blezer E, Rausch M, Brochet B, Foster-Gareau P, Balériaux D, Gaillard S, Dousset V, "Macrophage imaging in central nervous system and in carotid atherosclerotic plaque imaging using ultrasmall superparamagnetic iron oxide in magnetic resonance imaging," *Invest Radiol* 39, 619-625 (2004)

- [174] Dousset V, Delalande C, Ballarino L, Quesson B, Seilhan D, Coussemacq M, Thiaudière E, Brochet B, Canioni P, Caillé JM, "In vivo macrophage activity imaging in the central nervous system detected by magnetic resonance," *Magn Reson Med* 41, 329-333 (1999)
- [175] Rausch M, Hiestand P, Baumann D, Cannet C, Rudin M, "MRI-based monitoring of inflammation and tissue damage in acute and chronic relapsing EAE," *Magn Reson Med* 50, 309-314 (2003)
- [176] Corot C, Robert P, Idée JM, Port M, "Recent advances in iron oxide nanocrystal technology for medical imaging," *Adv Drug Deliv Rev* 58, 1471-1504 (2006)
- [177] Beard PC, Pérennès F, Draguioti E, Mills TN, "Optical fiber photoacoustic-photothermal probe," *Opt Lett* 23(15), 1235-1237 (1998)
- [178] Adler DC, Huang SW, Huber R, Fujimoto JG, "Photothermal detection of gold nanoparticles using phase-sensitive optical coherence tomography," *Opt Exp* 16(7), 4376-4393 (2008)
- [179] Skala MC, Crow MJ, Wax A, Izatt JA, "Photothermal optical coherence tomography of epidermal growth factor receptor in live cells using immunotargeted gold nanospheres," *Nano Lett* 8(10), 3461-3467 (2008)
- [180] Zhou C, Tsai TH, Adler DC, Lee HC, Cohen DW, Mondelblatt A, Wang Y, Connolly JL, Fujimoto JG, "Photothermal optical coherence tomography in ex vivo human breast tissues using gold nanoshells," *Opt Lett* 35(5), 700-702 (2010)
- [181] Bouma BE, Tearney GJ, Yabushita H, Shishkov M, Kauffman CR, DeJoseph Gauthier D, MacNeill BD, Houser SL, Aretz HT, Halpern EF, Jang IK, "Evaluation of intracoronary stenting by intravascular optical coherence tomography," *Heart* 89, 317-320 (2003)

- [182]Yabushita H, Bouma BE, Houser SL, Aretz HT, Jang IK, Schlendorf KH, Kauffman CR, Shishkov M, Kang DH, Halpern EF, Tearney GJ, "Characterization of human atherosclerosis by optical coherence tomography," *Circulation* 106, 1640-1645 (2002)
- [183]Ambrose JA, Winters SL, Stern A, Eng A, Teichholz LE, Gorlin R, Fuster V, "Angiographic morphology and the pathogenesis of unstable angina pectoris," *J Am Coll Cardiol* 5, 609-616 (1985)
- [184]Ambrose JA, Tannenbaum MA, Alexopoulos D, Hjemdahl-Monsen CE, Leavy J, Weiss M, Borrico S, Gorlin R, Fuster V, "Angiographic progression of coronary artery disease and the development of myocardial infarction," *J Am Coll Cardiol* 12, 56-62 (1988)
- [185]Hackett D, Davies G, Maseri A, "Pre-existing coronary stenosis in patients with first myocardial infarction are not necessarily severe," *Eur Heart J* 9, 1317-1323 (1988)
- [186]Little WC, Downes TR, Applegate RJ, "The underlying coronary lesion in myocardial infarction: implications for coronary angiography," *Clin Cardiol* 14, 868-874 (1991)
- [187]Nobuyoshi M, Tanaka M, Nosaka H, Kimura T, Yokoi H, Hamasaki N, Kim K, Shindo T, Kimura K, "Progression of coronary atherosclerosis: is coronary spasm related to progression?," *J Am Coll Cardiol* 18, 904-910 (1991)
- [188]Giroud D, Li JM, Urban P, Meier B, Rutishauer W, "Relation of the site of acute myocardial infarction to the most severe coronary arterial stenosis at prior angiography," *Am J Cardiol* 69, 729-732 (1992)
- [189]Gershlick AH, de Belder M, Chambers J, Hackett D, Keal R, Kelion A, Neubauer S, Pennell DJ, Rothman M, Signy M, Wilde P, "Role of non-invasive imaging in

the management of coronary artery disease: an assessment of likely change over the next 10 years. A report from the British Cardiovascular Society Working Group," *Heart* 93, 423-431 (2007)

[190]Shen T, Weissleder R, Papisov M, Bogdanov A, Jr, Brady TJ, "Monocrystalline iron oxide nanocompounds (Mion): physicochemical properties," *Magn Reson Med* 29, 599-604 (1993)

[191]Sapozhnikova V, Willsey B, Asmis R, Wang T, Jenkins JT, Mancuso JJ, Ma L, Kuranov R, Milner TE, Johnston KP, Feldman MD, "Near infrared fluorescence produced by gold nanoclusters (nanoroses)," *J Biomed Opt* (IN PRESS).

[192]Aikawa M, Rabkin E, Okada Y, Voglic SJ, Clinton SK, Brinckerhoff CE, Sukhova GK, Libby P, "Lipid lowering by diet reduces matrix metalloproteinase activity and increases collagen content of rabbit atheroma: a potential mechanism of lesion stabilization," *Circulation* 97, 2433-2444 (1998)

[193]Frank PG, Pavlides S, Lisanti MP, "Caveolae and transcytosis in endothelial cells: role in atherosclerosis," *Cell Tissue Res* 335, 41-47 (2009)

[194]Lu W, Tan YZ, Hu KL, Jiang XG, "Cationic albumin conjugated pegylated nanoparticle with its transcytosis ability and little toxicity against blood-brain barrier," *Int J Pharm* 295, 247-260 (2005)



## Vita

Tianyi Wang was born in Huangshi, Hubei Province, China on November 1st, 1982. He received his B.E. and M.E. degrees in electronic information engineering and optical engineering from Wuhan University, China in 2005 and 2007, respectively. As a graduate student, Tianyi worked under supervision of Professors Libo Zeng and Song Li to quantitatively analyze DNA of cast-off cervical cells using auto-spread liquid-base cytology and a DNA imaging cytometer, and to study the microcirculation using orthogonal polarization spectral imaging in the Engineering Research Center of Spectrum and Imaging Instruments at the Wuhan University.

In September 2007, Tianyi entered the PhD program in the Department of Biomedical Engineering at the University of Texas at Austin, Texas. He expects to complete his Doctor of Philosophy in Biomedical Engineering in May 2012. He has been working under Professor Thomas E. Milner for over four years and his research interests include medical imaging system design, modeling and image processing, specifically in thermal imaging, optical coherence tomography, nonlinear optical imaging, modeling of light and heat transfer in tissue and medical image processing.

Permanent address: No. 1 Hospital,  
Huangshi, Hubei, China  
435001

This dissertation was typed by the author.